BIOPHYSICALLY DETAILED NEURAL NETWORK MODELS OF BUSHY CELLS

THE EFFECTS OF GAP JUNCTIONS AND INHIBITION ON SYNCHRONIZATION OF BIOPHYSICALLY DETAILED NEURAL NETWORK MODELS OF BUSHY CELLS OF VENTRAL COCHLEAR NUCLEUS

BY
MELIH YAYLI,

A THESIS
SUBMITTED TO THE DEPARTMENT OF ELECTRICAL & COMPUTER ENGINEERING
AND THE SCHOOL OF GRADUATE STUDIES
OF MCMASTER UNIVERSITY
IN PARTIAL FULFILMENT OF THE REQUIREMENTS
FOR THE DEGREE OF
DOCTOR OF PHILOSOPHY

Doctor of Philosophy (2025) McMaster University
(Electrical & Computer Engineering) Hamilton, Ontario, Canada

TITLE:	The Effects of Gap Junctions and Inhibition on Synchronization of Biophysically Detailed Neural Network Models of Bushy Cells of Ventral Cochlear Nucleus
AUTHOR:	Melih YAYLI M.A.Sc. (McMaster University), B.Sc. (Ankara University)
SUPERVISOR:	Ian C. Bruce, PhD
NUMBER OF PAGES:	xv, 124

To all my fellow international graduate students who are dealing with depression and anxiety... Keep pushing!

Lay Abstract

The cochlear nucleus (CN) is an integral part of sound processing in the brainstem. One of the main cell types of the CN, bushy cells, extracts crucial sound localization cues. Apart from the excitation and inhibition bushy cells receive through chemical synapses, they are also connected via electrical synapses called gap junctions. Although previous studies investigate the effect of gap junctions on cell behaviors in other parts of the brain, their impacts on bushy cells are yet to be explored. Our studies use biophysically detailed neural network models to determine how bushy cells process incoming sound stimuli. Our simulations show that the gap junction connections have a substantial effect on the excitability of bushy cells and the spread of excitation between bushy cells. Gap junctions also contribute to the synchronized firing behavior in bushy cells, while the inhibition's effect on the synchronization is found to be non-monotonic.

Abstract

The cochlear nucleus is the first stage in the central auditory nervous system (CANS) that receives information from auditory nerve fibers (ANFs). Sound identification and localization cues are extracted here and propagated to the upper levels of the CANS. One of the main cell types of the ventral cochlear nucleus is the bushy cells which can be divided into two subtypes as globular and spherical bushy cells (GBCs and SBCs). Bushy cells receive excitation from ANFs and inhibition from D-stellate and tuberculoventral cells via chemical synapses. Additionally, bushy cells are connected via electrical synapses known as gap junctions and form clusters. One of the main features of bushy cells is enhancing the synchronization behavior seen in ANFs. Although coincidence detection can be the underlying mechanism for the GBCs to show this behavior, SBCs' synchrony enhancement mechanism is still unclear. In this thesis, biophysically detailed neural network models of SBCs and GBCs are built to investigate the effect of gap junctions on the excitability and the synchronization behavior of GBCs and SBCs. Current injection simulations show that gap junctions substantially affect the excitability of the bushy cell models and allow the spread of excitation within and between the cell clusters. Simulations made with more realistic synaptic inputs indicate that inhibition and gap junctions strongly affect the synchronization of the model SBCs and GBCs. Although the effects of the inhibition on synchronization is non-monotonic, the effects of gap junctions on the synchronization found to be clearer. A grid search is done to investigate the effects of the inhibition, gap junctions, and strength of excitation on the synchronization of bushy cell models and a set of parameters is hand-picked to fit the model results to the recorded physiological data.

Acknowledgments

I would like to express my sincere gratitude to my supervisor, Dr. Ian C. Bruce, for his unwavering guidance and patience. His invaluable support has been instrumental in the completion of this work. I also want to thank Dr. Laurel H Carney and Dr. Aleksandar Jeremic for being a part of my thesis committee and their tremendous help.

Despite spending the past decade away from my family, I have always felt their unwavering support. This experience has reinforced my belief that physical distance does not weaken our bond; rather, we remain as connected as ever. I would like to specifically thank my father, Dr. Yusuf Yaylı, for his support, both as a father and a mentor.

I am also deeply appreciative of my close friends, whose steadfast support has been a source of strength throughout this journey. Their presence during both challenging times and moments of celebration has meant a great deal to me.

Furthermore, I extend my gratitude to the Turkish Ministry of Education for its financial support throughout my master's studies.

Declaration of Academic Achievement

This thesis consists of main content chapters that have already been submitted or are planned to be submitted as journal articles, while Chapters 1 and 5 provide a general Introduction and Discussion, respectively. Because Chapters 2 and 3 are based on journal articles, some of the information in Chapter 1 and these later chapters could overlap. For consistency, these chapters are kept as is in terms of content and reformatted to be more consistent with the rest of the thesis, and a common bibliography is provided at the end of the thesis.

All of the chapters are a collaboration between my thesis supervisor, Dr. Ian C. Bruce, and me. Under the guidance of Ian C. Bruce, I developed the research questions, coded the main framework, did the literature review, analyzed the simulation results, and wrote the initial manuscript drafts. Chapter 2 is under preparation as a journal article to be submitted to PLoS Computational Biology. Chapter 3 has been submitted to Journal of the Association for Research in Otolaryngology (JARO), titled as "Effects of Gap Junctions and Inhibition on the Synchronization Behavior of a Biophysically-Detailed Neural Network Model of Bushy Cells." It has been reviewed once, and the version included in this thesis is based on the first resubmission of the manuscript to JARO. Chapter 4 presents the preliminary results of the spherical and globular bushy cell neurogram responses to speech and is not in a journal manuscript format.

Notation and Abbreviations

AN Auditory Nerve
ANF Auditory Nerve Fiber
AP Action Potential
AVCN Anteroventral Cochlear Nucleus
BS Bushy Cell
CANS Central Auditory Nervous System
CC Coupling Coefficient
CF Characteristic Frequency
ChS Sustained Chopper
ChT Transient Choppper
CN Cochlear Nucleus
Cx Connexin
DCN Dorsal Cochlear Nucleus
DS D-Stellate
EPSC Excitatory Post-Synaptic Current
EPSP Excitatory Post-Synaptic Potential
GABA Gamma-Aminobutyric Acid
GBC Globular Bushy Cells
HH Hodgkin-Huxley
IC Inferior Colliculus
ICB Ian C. Bruce
IHC Inner Hair Cell
IPSC Inhibitory Post-Synaptic Current
IPSP Inhibitory Post-Synaptic Potential
ITD Interaural Time Difference
KLT Low-threshold Potassium Channel
KHT High-threshold Potassium Channel
LSO Lateral Superior Olive
MNTB Medial Nucleus of Trapezoidal Body
MOC Medial Olivocochlear
MSO Medial Superior Olive

MY Melih Yayli
NMDA N-Methyl-D-aspartic Acid
NSIM Neurogram Similarity Index Measure
OHC Outer Hair Cell
OnC Onset Chopper
OnL Onset with Latent Response
PL Primary-like
PLn Primary-like with Notch
PSTH Peri-stimulus Time Histogram
RM Rothmann and Manis
SBC Spherical Bushy Cell
SI Synchronization Index
SNR Signal to Noise Ratio
SPL Sound Pressure Level
SR Spontaneous Rate
std standart deviation
STMI Spectro-Temporal Modulation Index
TB Trapezoid Body
TGN Trigger Group Neuron
TS T-Stellate
TV Tuberculoventral
VCN Ventral Cochlear Nucleus
XM Xie and Manis

Contents

List of Figures

Chapter 1

Introduction and Literature Review

1.1 Introduction

The central auditory nervous system of mammals is a complex structure consisting of various stages that process the sound in different ways to extract useful features that are projected to the upper levels of the system. The cochlear nucleus is the first stage in the central auditory nervous system to receive inputs from auditory nerve fibers (ANFs). The cochlear nucleus (CN) itself is also divided into compartments with distinctive cell types inhabiting each section. Sound identification and localization cues are extracted here and propagated to the upper levels via parallel pathways.

In this thesis, a biophysically detailed neural network model of bushy cells of the ventral cochlear nucleus (VCN) is introduced, with an emphasis on the implementation of gap junction structures. Contributions of gap junctions and inhibition to the synchronization behavior of bushy cells is explored by using these detailed neural network models.

In the first chapter of this thesis, a brief literature review of the auditory periphery and cochlear nucleus is done. Different cell types located in the CN, their morphologies and the physiological responses of these different cell types to incoming stimuli are investigated. Lastly, gap junction structures seen in the bushy cells of VCN are delved into.

In the second chapter, the effect of gap junctions on the excitability of the bushy cell network model is investigated. The network's response to current injections and simple synaptic inputs is checked. The contribution of gap junctions to the spread of excitation in different network connection settings, and the effect of a range of gap junctions and leakage current conductance levels on the excitability of the cells are examined.

In Chapter 3, the effect of gap junctions and inhibition on the synchronization behavior of the bushy cell network model is analyzed. Details of the methods used to create the biophysically detailed neural networks of bushy cells of VCN are provided. A review of various bushy cell network models is also given in this chapter. The implementation of gap junctions and the synaptic model used in this network are explained. The results presented in this chapter are obtained by providing Bruce *et al.* (2018) ANF model responses to sound stimuli as realistic synaptic inputs to the bushy cell models. The effects of gap junctions and inhibition on the synchronization index scores and firing rate of bushy cells over a range of characteristic frequencies (CFs) are shown. How an optimal parameter set of gap junctions, inhibition and excitation strength are hand-picked is explained.

In Chapter 4, initial results of neurograms, which represent the response of population of bushy cells to an incoming sound stimulus, obtained from spike train outputs of the base model, without gap junctions and inhibition, and bushy cell models constructed with the best parameter set are shown.

Chapter 5 presents the conclusions made from all of the results obtained through various simulations, what can be done to improve the model, and what kind of explorations can be performed as future work.

Appendix A provides detailed mathematical expressions of the ion channels of the models.

In Appendix B, supplementary figures for Chapter 3 are provided. This Appendix offers in-depth information on how the internal model parameters such as membrane constant, excitatory post-synaptic current (EPSC) decay time constant and EPSC size affect the synchronization of a population of bushy cell models covering a range of CFs. The effect of inhibition on the cut-off frequency behavior of low pass filtering behavior of the spherical and globular bushy cell models is provided. Synchronization index scores over a range of sound pressure levels (SPLs) for each cell in a fully connected cluster are also presented. Visualizations of the spike identification process and the low threshold potassium channel's effect on the spiking dynamics is provided. Post stimulus time histograms of SBC and GBC models with and without gap junctions and inhibition are also given in this chapter.

The model codes used in this research can be found in here.

1.2 Auditory Periphery

The auditory periphery for humans consists of the outer ear, middle ear and inner ear, as illustrated in Fig. 1.1.

The outer ear consists of pinna, concha and external auditory meatus (a.k.a ear canal) and increases the amount of energy transferred to the middle ear. After the

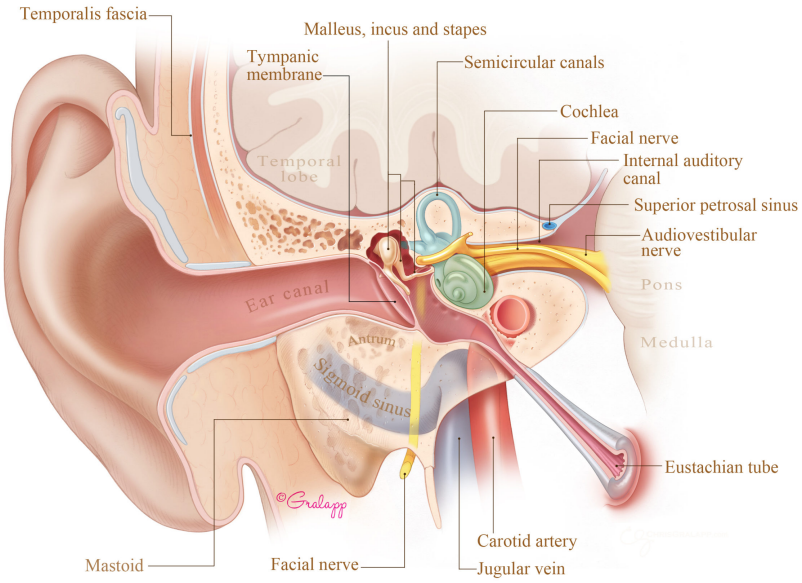

Figure 1.1: An illustration of the auditory periphery of humans from a coronal perspective. ©2020 Chris Gralapp, used with permission.

sound travels through the ear canal, it hits the tympanic membrane (a.k.a ear drum) and causes it to vibrate. These vibrations are passed through the middle ear ossicles and are called the incus, malleus, and stapes. These bones act as an impedance-matching mechanism since a direct transition between the air and the fluids inside the cochlea would result in the loss of most of the energy of the sound signal as it would be reflected. The sound signals enter the cochlea from the oval window. The cochlea comprises three compartments: scala vestibuli, scala media and scala tympani. The cochlear fluid dynamics and the structure's stiffness allow different parts of the cochlea to be more responsive to specific frequencies. This kind of behavior is essential in terms of creating a frequency tuning across the cochlea and allows it to act as a structure that can apply a time-frequency analysis to the incoming stimuli. The base of the cochlea is more sensitive to high frequency vibrations while the apex of the cochlea is more sensitive to low frequency vibrations. One of the most essential structures in the cochlea is the organ of Corti, which is located on top of the basilar membrane and hosts the inner and outer hair cells that auditory nerve fibers innervate. A cross-section of the cochlea and a detailed illustration of the organ of Corti can be seen in Fig. 1.2.

Inner and outer hair cells have rigid structures on top of them called stereocilia,

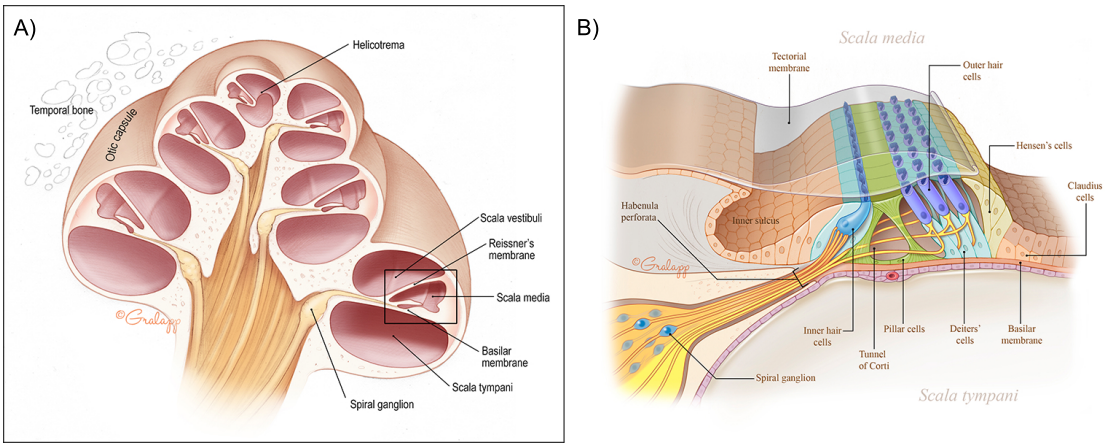

Figure 1.2: Illustration of (A) the cross-section of the cochlea and (B) the organ of Corti. ©2020 Chris Gralapp, used with permission.

which have ionic channels. As the vibrations cause displacement in the basilar membrane, the organ of Corti also moves with it. The movement of the basilar membrane causes the stereocilia to be pushed against the tectorial membrane and the ion channels residing on the stereocilia to open up. This allows ionic exchange between the endolymph and hair cells. This mechanism enables the mechanical displacement to turn into electrical current, so the organ of Corti can be seen as a transducer.

1.3 Auditory Nerve Fibers

Auditory nerve fibers innervate the inner and outer hair cells of the organ of Corti and transfer the auditory information to the central auditory nervous system. The majority of the ANFs innervate the inner hair cells and are called Type I fibers. Type I fibers respond to incoming sound stimuli and can have high spontaneous firing rates, which means the spiking activity can occur without a stimulus present. Most of the recordings taken from ANFs are from Type I fibers. Type II fibers connect to the outer hair cells, and their role in sound processing is unclear since it is harder to record from them.

Post-stimulus time histograms (PSTHs) are a useful indicator of ANFs' responses to incoming stimuli. Fig. 1.3 shows a typical response of an ANF to a pure tone stimulus. The fiber responds to the incoming stimuli with a sharp spike on the onset. Then, the fiber adapts, and the spike rate rapidly decreases to a steady rate. After the stimulus ends, the fiber's response is suppressed briefly before returning to its spontaneous rate. ANFs can be divided into three groups according to their spontaneous rates: high, medium and low spontaneous rate fibers. High spontaneous

rate ANFs have low thresholds while low spontaneous rate ANFs have high thresholds. About 20 percent of the fibers have low spontaneous rates below 1 spike/sec, 4 percent of the fibers have SRs between 14 - 40 spikes/sec, and the rest of the fibers have SRs between 40 - 120 spikes/sec (Liberman, 1978).

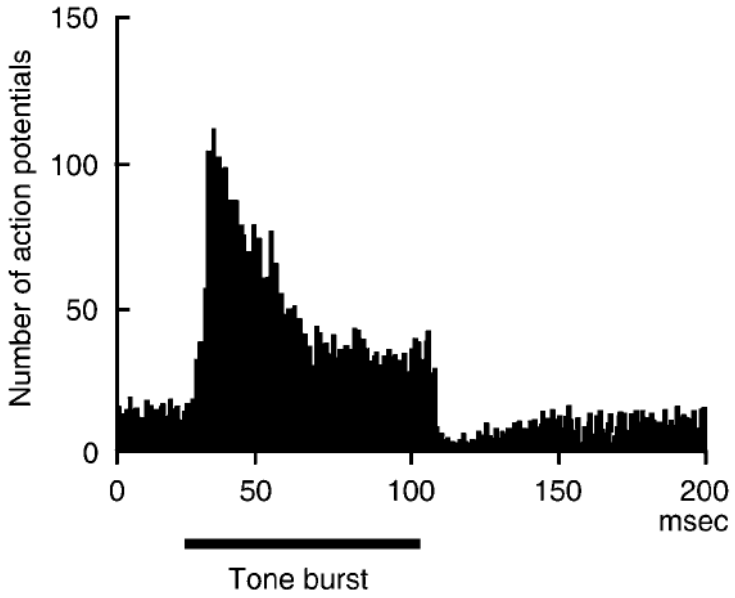

Figure 1.3: PSTH of an auditory nerve fiber. Reprinted with permission of the Brill Publishers, Figure 4.2 from Pickles (2013) ©2013.

The basilar membrane frequency tuning behavior is passed along to hair cells, which means the hair cells that reside at the base of the cochlea are tuned to process high frequency information, while the hair cells residing at the apex of the cochlea processes lower frequency information. As a result, the ANFs that innervate these hair cells at specific spots have similar tuning to the hair cell.

The tuning curves of ANFs with different characteristic frequencies can be seen in Fig. 1.4. The tuning curves show the necessary stimulus intensity needed for the fiber to fire more than its spontaneous rate. From the shape of their frequency responses, it can be seen that the fibers act like a bandpass filter. Low frequency fibers have symmetrical frequency response shapes, while the high frequency fibers have asymmetrical shapes. The tuning curves indicate that the fibers tuned to the specific frequencies need less intense stimulation to activate at that particular frequency than the other frequencies.

For low stimulus frequencies, ANFs tend to fire at a specific phase of an incoming stimulus. This kind of phase locking behavior can be clearly seen in period histograms (Fig. 1.5) and raster plots (Fig. 1.16). For high frequencies, the probability of the

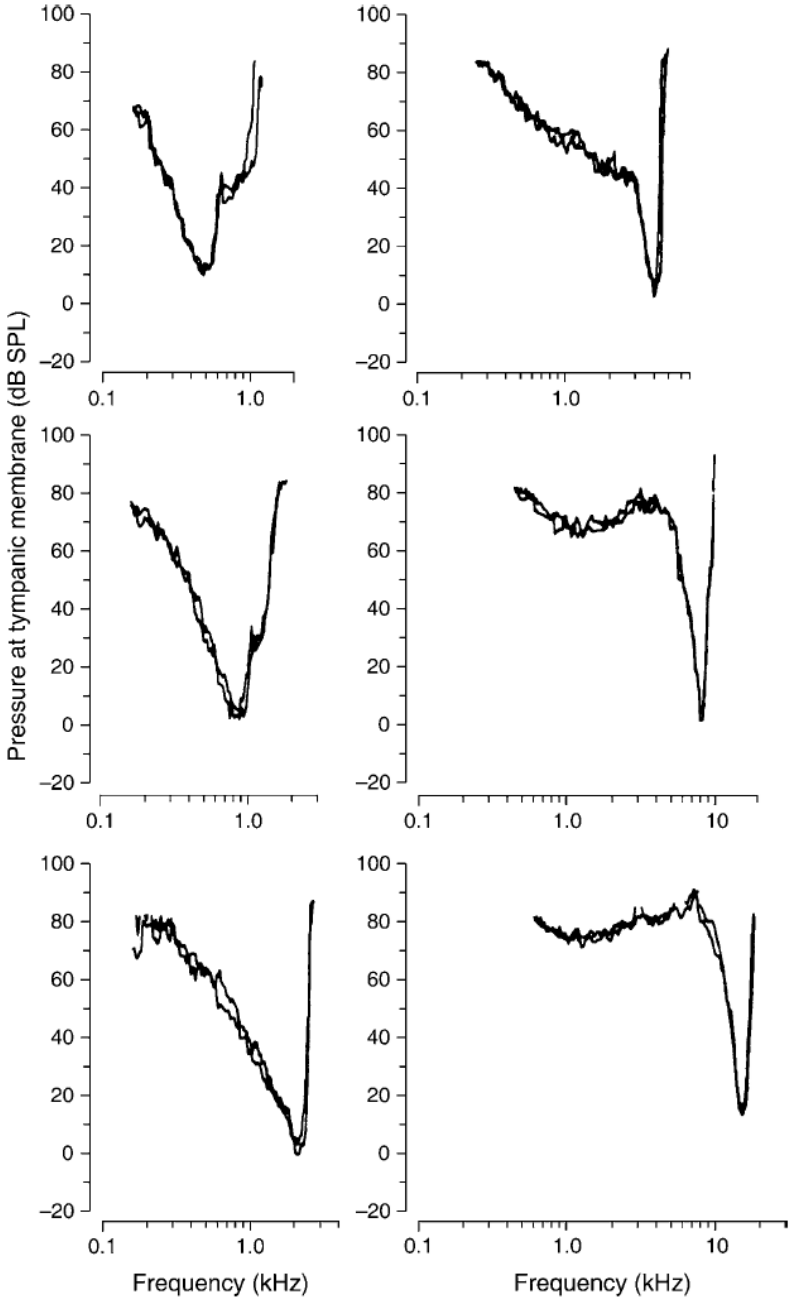

Figure 1.4: Tuning curves of ANFs with different characteristic frequencies. Two similar characteristic fibers tuning curves are overlayed on the same plots to show that the similar CF fibers have similar tuning responses. Reprinted with permission of the Acoustical Society of America, Figure 4.3 from Liberman (1978) ©1978.

ANF spiking is approximately equal for every phase of the cycle, which means ANFs are not able to show synchronized firing behavior to high frequency periodic stimuli. Maximum synchronization index scores of a population of ANFs can be seen in Fig. 1.6. The population of ANFs shown in the figure are receiving sinusoidal inputs with a frequency the same as their CF. The maximum achievable synchronization scores shown in Fig. 1.6 tell us that the ANFs transition from high SI scores at low frequency to low SI scores at high frequency, indicating that ANFs act like a low pass filter in regards to their temporal response properties. The frequency at which the max SI scores start dropping rapidly as a function of frequency is referred to as the synchronization cutoff frequency.

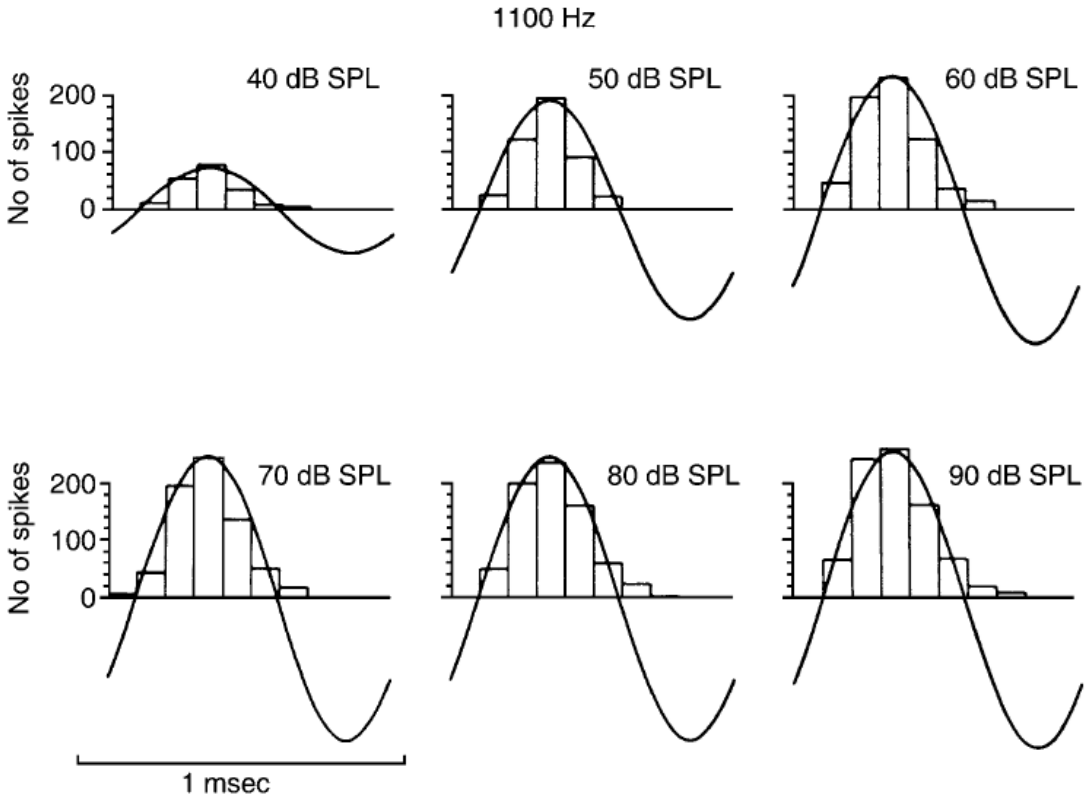

Figure 1.5: Period histograms of an ANF with CF of 1000 Hz. The fiber fires only at the positive cycle and fires the most at the peak of the stimulus. After 70 dB SPL, the fiber saturates, but the general shape of the period histogram stays similar. Reprinted with permission of The American Physiological Society, Figure 4.8 from Rose *et al.* (1971) ©1971.

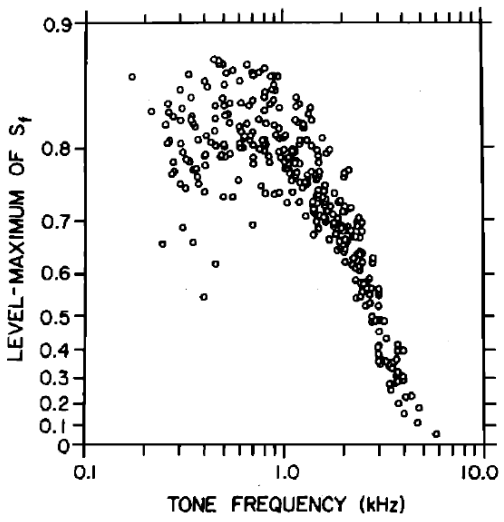

Figure 1.6: Maximum synchronization scores of a population of ANFs. Reprinted with permission of the Acoustical Society of America, Figure 5 from Johnson (1980) ©1980.

1.4 Cochlear Nucleus

The cochlear nucleus (CN) is the first stage in the central auditory nervous system to receive auditory input from the ANFs. Sound identification and localization cues get extracted here and propagated to the upper levels of the central auditory nervous system via three main parallel pathways (Cant and Benson, 2003). The cochlear nucleus is a complex structure consisting of various cell types that have different morphological and physiological properties. Various cell types and their locations in the CN can be seen in Fig. 1.7. Properties such as firing rates, spike discharge patterns, action potential properties and where in the upper levels of the auditory nervous system the cells are projecting the information are useful in terms of identifying different cell types residing in the CN (Typlt *et al.*, 2012; Manis *et al.*, 2019). PSTHs are good indicators of a cell's behavior toward incoming stimuli. The type of PSTHs of the main VCN cell types are presented in Fig. 1.8. This kind of variability allows different types of cues to get extracted in the cochlear nucleus. While tonically firing cells such as T-stellate cells can encode information in their firing rate, phasically firing cells such as bushy cells are able to encode the fine timing information efficiently (Oertel, 1983). These two main types of cells convey this useful information to the upper levels via parallel pathways. Fig. 1.9 shows the main projection patterns of parts of the VCN to the upper levels of the central auditory system.

The VCN receives the innervation from the ANFs that connect with the hair cells

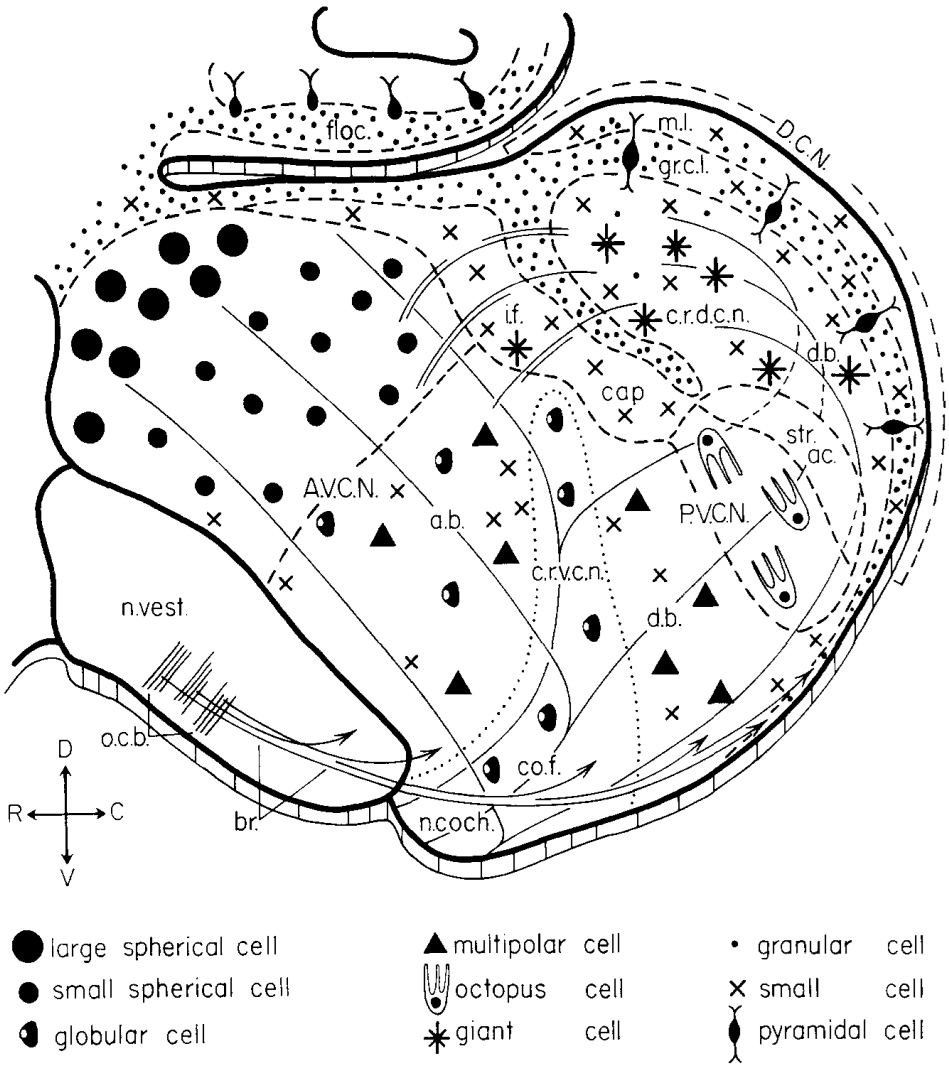

Figure 1.7: Locations of main cell types of CN. AVCN, anteroventral cochlear nucleus; cap, peripheral cap of small cells; c.r.d.c.n., central region of the DCN; c.r.v.c.n., central region of the ventral nucleus; DCN, dorsal cochlear nucleus; floc, flocculus (cerebellum); gr.c.l., granular cell layer; if, intrinsic fibres; m.l., molecular layer; PVCN, posteroventral cochlear nucleus; strac, dorsal and intermediate acoustic striae. Reprinted with permission of Elsevier, from Osen and Roth (1969) ©1969.

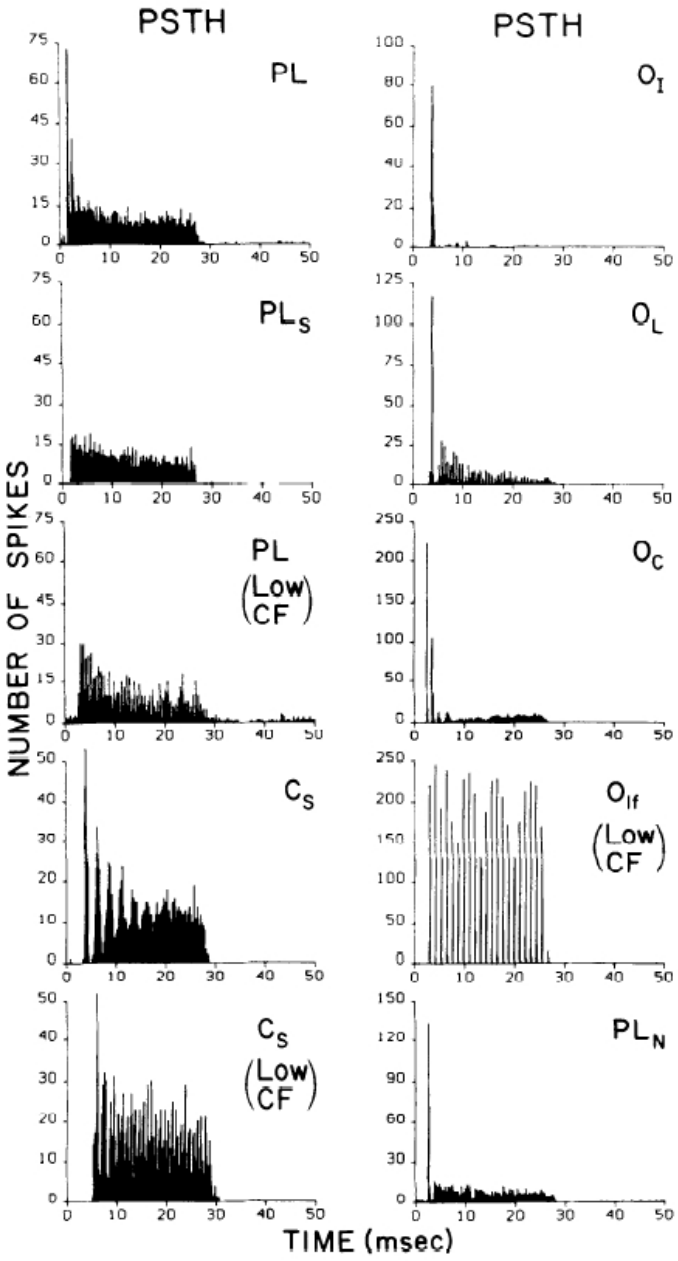

Figure 1.8: Sample of common PSTH responses seen in the ventral cochlear nucleus. PL: primary like, PL_S: primary like with low spontaneous firing, C_S: sustained chopper, O_I: onset with little late activity, O_L: onset unit with sustained phase locked activity, O_C: onset with initial chopper response, PL_N: primary like with notch after initial response. Reprinted with permission of American Physiological Society, from Rhode and Smith (1986) ©1986.

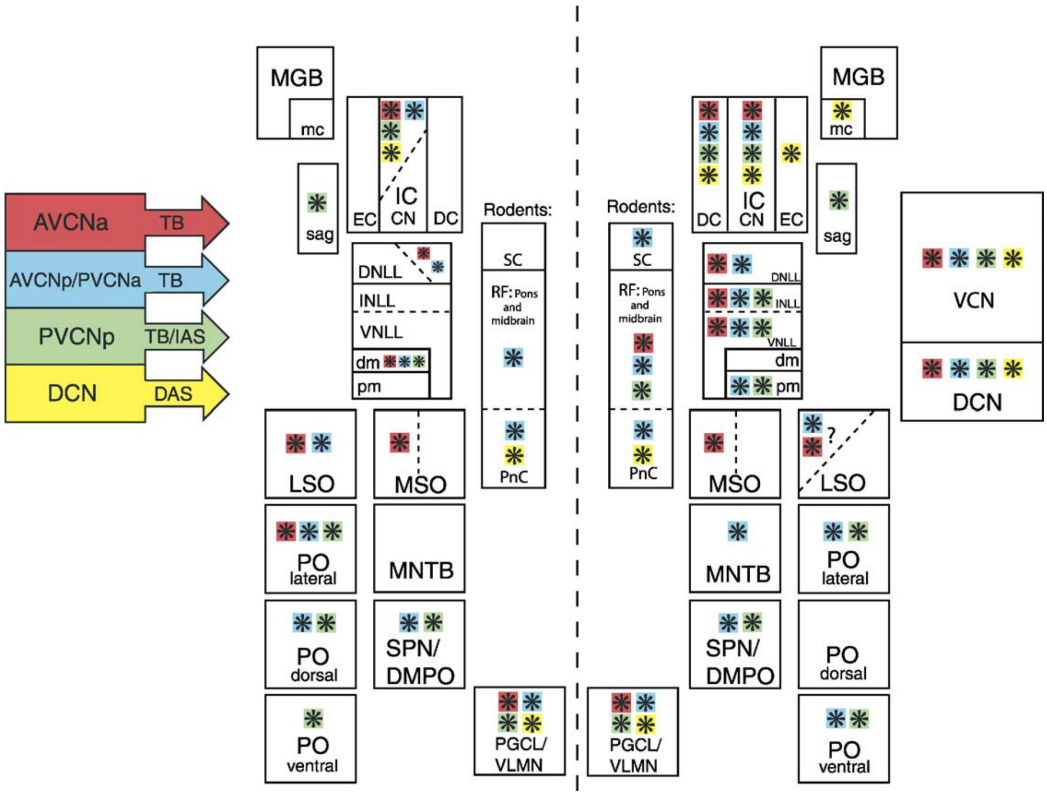

Figure 1.9: Projections of main areas of CN to the upper levels of the central auditory nervous system. AVCNa: anterior part of anteroventral cochlear nucleus; AVCNp: posterior part of the anteroventral cochlear nucleus; CN: central nucleus of the inferior colliculus; DAS: dorsal acoustic stria; DC: dorsal cortex of the inferior colliculus; DCN: dorsal cochlear nucleus; DMPO: dorsomedial periolivary nucleus; DNLL: dorsal nucleus of the lateral lemniscus; EC: external cortex of the inferior colliculus; IAS: internal acoustic stria; IC: inferior colliculus; INLL: intermediate nucleus of the lateral lemniscus; LSO: lateral superior olivary nucleus; mc: magnocellular division of the medial geniculate body; MGB: medial geniculate body; MNTB: medial nucleus of the trapezoid body; MSO: medial superior olivary nucleus; PGCL: lateral paragigantocellular nucleus; PnC: caudal pontine reticular nucleus; PnO: oral pontine reticular nucleus; PO: periolivary nuclei; pm: posteromedial part of the ventral nucleus of the lateral lemniscus; PVCNa: anterior part of the posteroventral cochlear nucleus; PVCNp: posterior part of the posteroventral cochlear nucleus; sag: sagulum; SC: superior colliculus; SPN: superior paraolivary nucleus; TB: trapezoid body; VCN: ventral cochlear nucleus; VLMN: ventrolateral medullary nucleus; VLTg: ventrolateral tegmental area; vm: ventromedial part of the ventral nucleus of the lateral lemniscus; VNLL: ventral nucleus of the lateral lemniscus. Reprinted with permission of Elsevier, from Cant and Benson (2003) ©2003.

in the more apical region of the cochlea, while the dorsal cochlear nucleus (DCN) receives innervation from more basal regions (Ryugo and Parks, 2003). This indicates the DCN focuses on processing higher frequency information than VCN. The tonotopic mapping behavior projecting from the cochlea to the cochlear nucleus can be seen in Fig. 1.10.

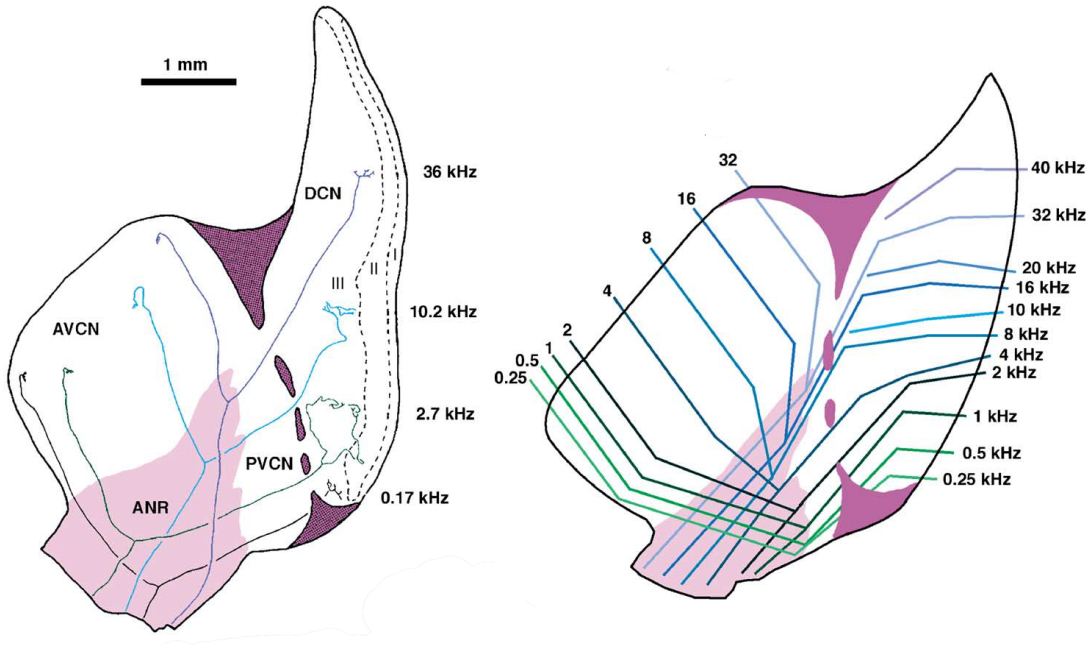

Figure 1.10: The structure of Type I ANF innervation of cochlear nucleus and the resulting tonotopic structure. DCN receives higher frequency information than VCN. ANR: auditory nerve root; AVCN, anteroventral cochlear nucleus; DCN: dorsal cochlear nucleus; PVCN: posteroventral cochlear nucleus. Reprinted with permission of Elsevier, from Ryugo and Parks (2003) ©2003.

1.4.1 D-Stellate Cells

D-stellate (a.k.a radiate multipolar) cells are the inhibitory cells in the VCN that show onset chopper response to the inputs with frequencies close to their CFs. Their dentrites project dorsally within the CN, and because of their orientation, they receive a wide range of excitatory inputs coming from ANFs. D-stellates provide inhibitiory inputs to the primary cells of the ventral and dorsal cochlear nucleus. Networks in the dorsal part of the cochlear nucleus are responsible for extracting sound localization

cues, and wideband inhibition coming from D-stellate cells is proposed to be crucial for this function (Arnott *et al.*, 2004).

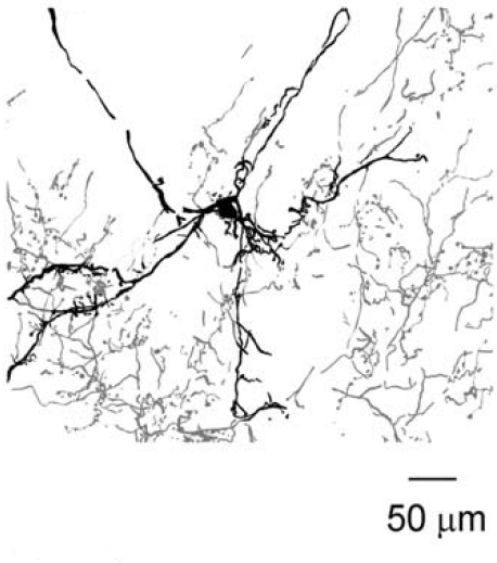

Figure 1.11: Morphology of a d-stellate cell. Reprinted with permission of Elsevier, from Needham and Paolini (2006) ©2006.

1.4.2 Tuberculoventral Cells

Tuberculoventral cells (a.k.a vertical cells) are a type of interneuron cells residing in the deep layers of the dorsal cochlear nucleus. The cell body and axon orientation of TV cells are parallel to the ANF projection path, and TV cells receive narrowband inputs, meaning they are sharply tuned to the narrow frequency range from which they receive their ANF inputs. The morphological structure of a TV cell can be seen in Fig. 1.12. TV cells project to the VCN and provide narrowband glycinergic inhibition to bushy and T-stellate cells (Zhang and Oertel, 1993; Oertel and Wickesberg, 1993). They receive frequency specific excitation from ANFs and T-stellate cells and weak inhibition from the interneurons of cochlear nucleus such as D-stellate cells and other TV cells (Kuo *et al.*, 2012). They are tonically firing cells, respond weakly to broadband noises and have chopper or onset type responses (Fig. 1.8). Their delayed frequency specific inhibition to the primary cells of the VCN are hypothesized to provide monaural echo suppression (Wickesberg and Oertel, 1990).

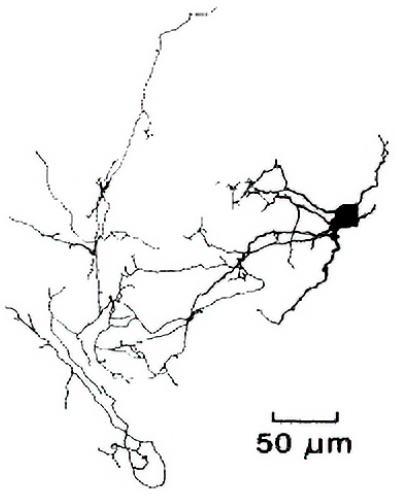

Figure 1.12: Morphology of a tuberculoventral cell. Reprinted with permission of American Physiological Society, from Zhang and Oertel (1993) ©1993.

1.4.3 Bushy Cells

Bushy cells are one of the main cell types of the AVCN that sends information to the upper stages of the central auditory nervous system through parallel pathways. The cells have a round soma and one or two main dendrites that spread thin dendritic trees. Bushy cells respond to incoming stimuli with one or a few action potentials at the beginning of the stimuli, also known as phasic firing. This kind of firing behavior is known to preserve fine timing information of the stimuli. Depending on the shape of the soma, the type of excitation they receive and their response patterns, bushy cells can be classified as spherical or globular bushy cells (SBCs or GBCs). SBCs reside in the anterior division of the AVCN, while GBCs reside in the posterior division of the AVCN (Smith and Rhode, 1987). While spherical bushy cells receive few suprathreshold inputs through large endbulbs of Held, globular bushy cells receive subthreshold inputs from a large number of ANFs through modified endbulbs of Held (Spirou *et al.*, 2005; Rhode, 2008). SBCs have a primary-like type of response which means they can follow the ANF response patterns accurately. GBCs show a primary-like with a notch response pattern, which includes a notch right after the initial peak in their PSTH pattern. Besides the excitation they receive from ANFs, bushy cells receive broadband inhibition from D-Stellate (DS) cells and narrowband inhibition from tuberculoventral (TV) cells. Bushy cells reside in the VCN as clusters, and they have soma-somatic connections. One type of these connections are gap junctions

(a.k.a electrical synapses) (Gómez-Nieto and Rubio, 2009, 2011). A 3D reconstruction of a bushy cell cluster can be seen in Fig. 1.14.

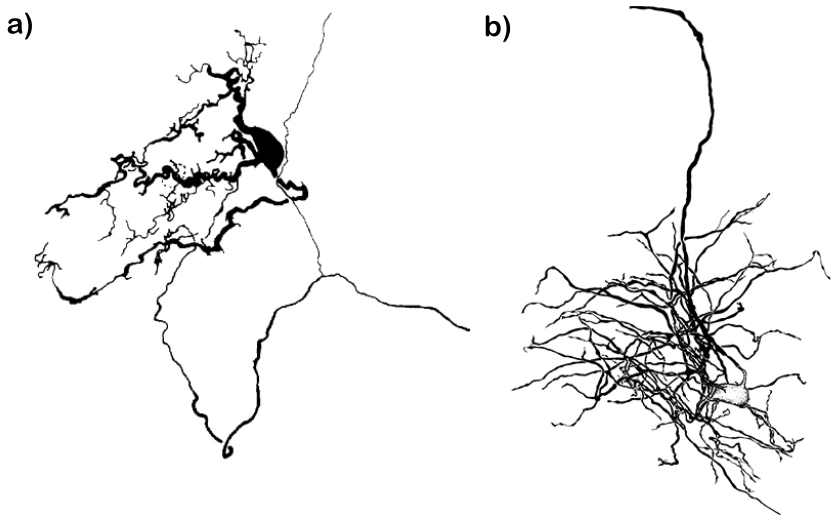

Figure 1.13: Camera lucida drawings of a) spherical and b) globular bushy cells show the distinctive cell shape of bushy cells. Reprinted with permission of John Wiley and Sons, a) from Rhode *et al.* (1983) ©2004 and b) from Smith and Rhode (1987) ©2004.

The projection targets of the main VCN cell types can be seen in Fig. 1.15 which indicates the differences between the projection paths of SBCs and GBCs. Bushy cells project the fine timing information to the medial superior olivary nucleus (MSO) of the contralateral and ipsilateral part of the brain, where this information is compared with each other for sound localization (Smith *et al.*, 1993; Cao and Oertel, 2010). While SBCs provide excitatory input to the MSO, GBCs provide excitatory input to the medial nucleus of the trapezoid body (MNTB), which provides inhibitory inputs to MSO. The lateral superior olive (LSO) receives excitatory inputs from ipsilateral SBCs and inhibitory inputs from contralateral GBCs via MNTB. The comparison between these two inputs helps LSO to propagate sound localization cues to the upper levels of CANS.

ANFs respond to periodic stimuli in a synchronized manner, which means their firing patterns specifically focus on certain phase of the periodic stimuli they receive. This behavior can be seen as a peak in their period histograms. The synchronization index (a.k.a vector strength), which is calculated using these period histograms, quantifies the degree of firing synchrony. A synchronization index (SI) score of 0 means the spike distributes evenly across the time bins of the period histograms while 1 means spikes are confined in a single time bin. This kind of firing behavior is even more prominent in bushy cells which can be seen in Fig. 1.16 and Fig. 1.17. For

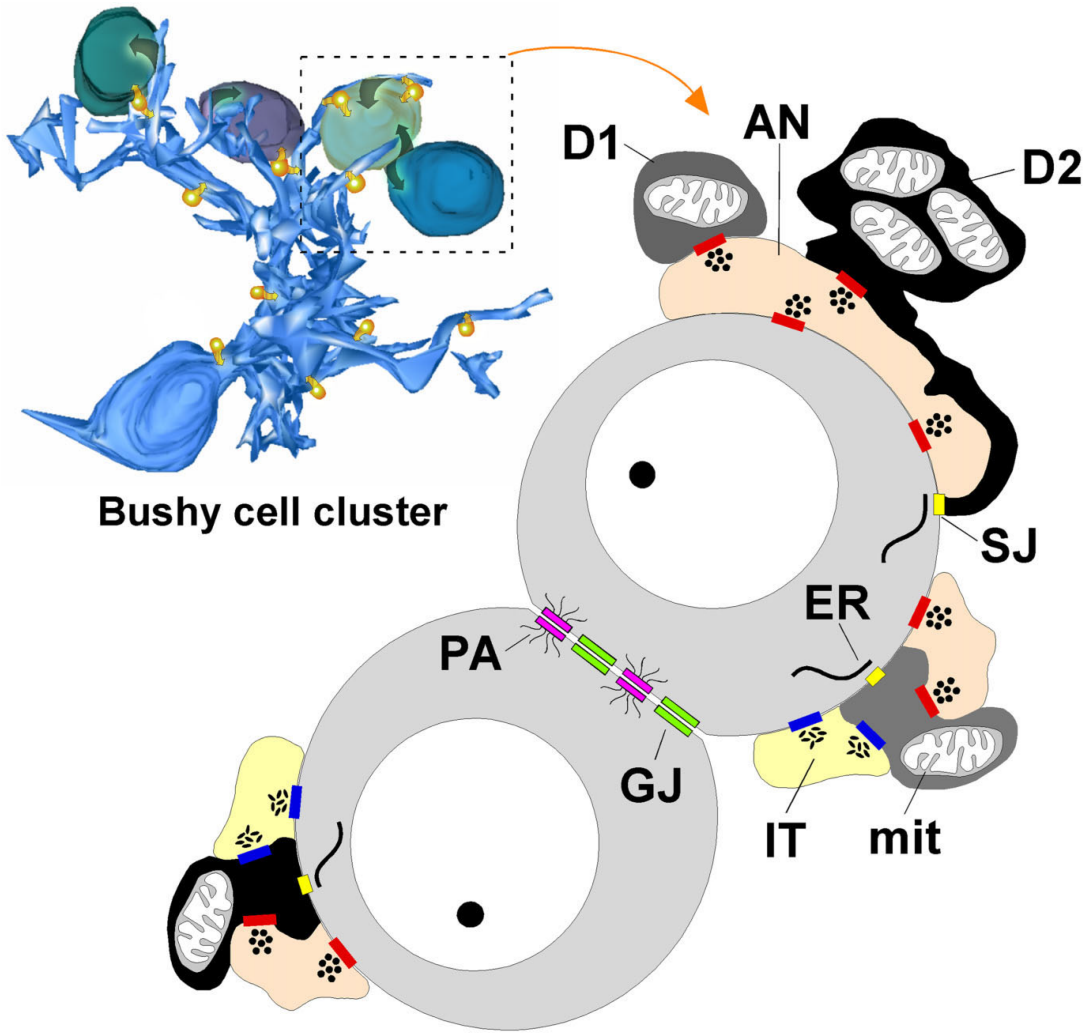

Figure 1.14: A 3D reconstruction of a bushy cell cluster in VCN. Apart from taking excitatory and inhibitory through AN and IT terminals, the cells in the cluster receive excitatory inputs through gap junctions (GJ). Another somasomatic connections between the cells are puncta adherentia (PA). AN: auditory nerve; CB: cell body; D1: dendrite 1; D2: dendrite 2; ER: endoplasmic reticulum; IT: inhibitory terminal; mit: mitochondria; SJ: sarcoplasmic junction (dentro-somatic). Reprinted with permission of Wiley-Blackwell Electronic Journals, from Gómez-Nieto and Rubio (2009) ©2009.

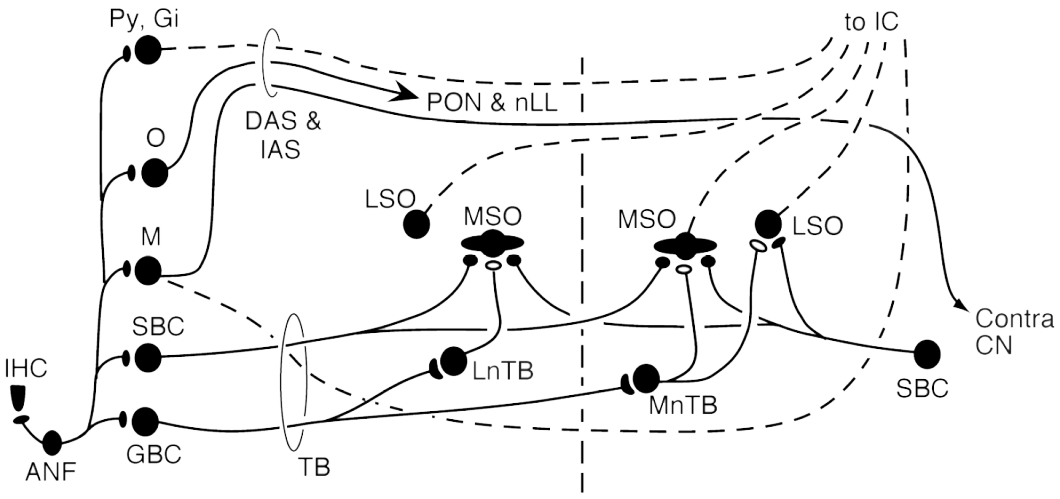

Figure 1.15: Projections of main cell types of CN to the upper levels of central auditory nervous system. Abbreviations are the same with Fig. 1.9 with additions of, gi: giant cells; M: D-Stellate and T-stellate cells; O: Octopus cells; py: pyramidal cells. Reprinted with permission of Oxford Publishing Limited, from Young and Oertel (2004) ©2004.

GBCs the mechanism behind the synchrony enhancement can be identified as a coincidence detection since it receives many ANF inputs Smith and Rhode (1987); Joris *et al.* (1994); Louage *et al.* (2005); Joris and Smith (2008); Rhode (2008). But for SBCs, which receive few suprathreshold inputs, the mechanism behind the synchrony enhancement is not clear.

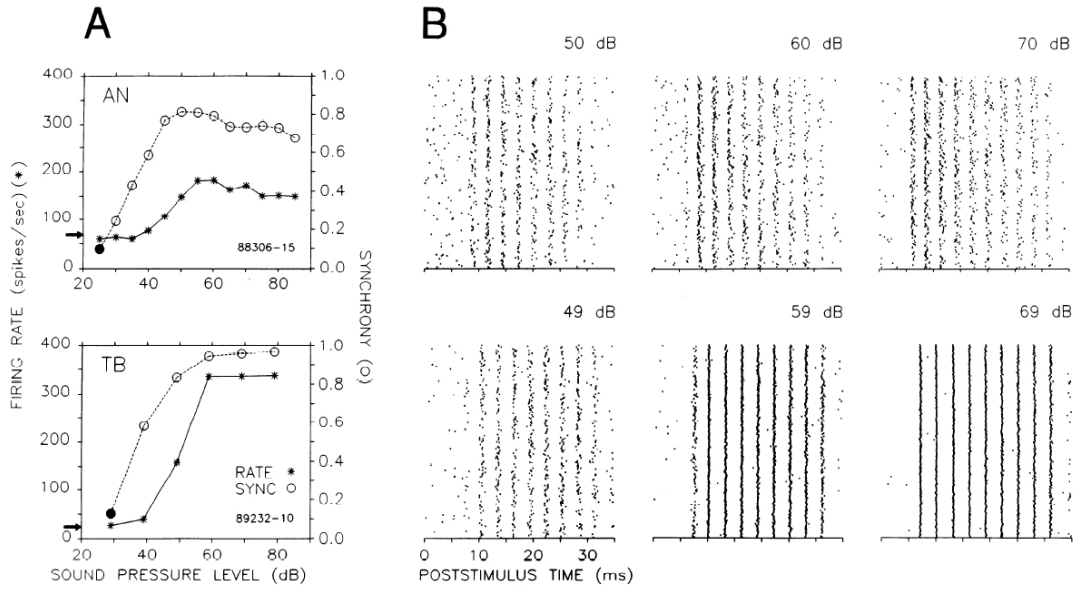

Figure 1.16: A) Firing rate and synchronization versus level plots of an ANF with a characteristic frequency (CF) of 350 Hz (top row) and a fiber with a CF of 340 Hz recording taken from the ascending pathways of trapezoid body (TB) which is believed to be originated from bushy cells of ventral CN (bottom row). B) Raster plots showing the synchronization behavior in the firing patterns of an ANF (top row) and a TB fiber (bottom row). The synchronization enhancement in the measurements taken from TB fiber compared to ANF firing patterns can be seen as the cell firing in a more confined matter at each period of the stimuli. Figure from Joris *et al.* (1994), reprinted with permission from The American Physiological Society.

1.5 Gap Junctions in Bushy Cells

Immunolabeling studies (Gómez-Nieto and Rubio, 2009, 2011; Rubio and Nagy, 2015) indicate that the bushy cells of the ventral CN have soma-somatic connections. One type of these connections being gap junctions suggests that these cells are electrically coupled. These connections allow the excitation to spread across the cells in the

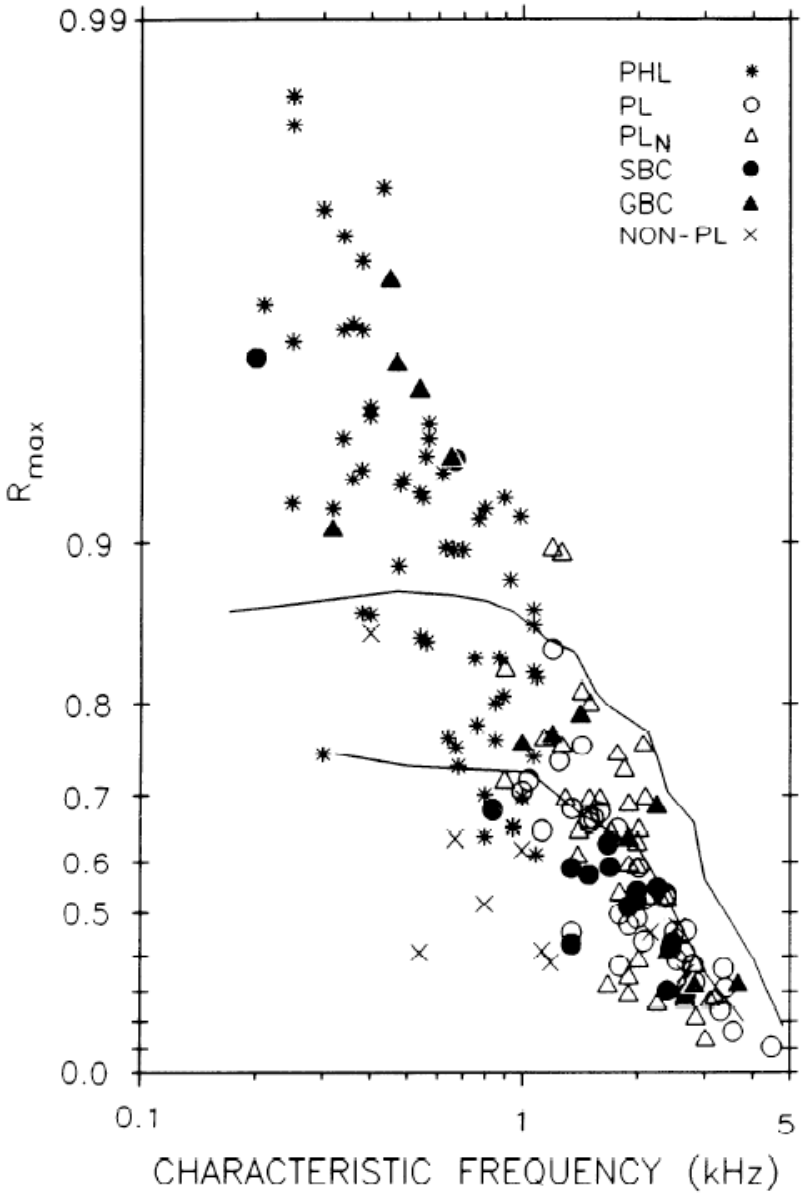

Figure 1.17: Maximum synchronization index values of a population of cells that projects through TB as a function of the cell's CF. The solid lines represents the upper and lower boundaries of synchronization index values of ANFs reported in Johnson (1980). Different types of cell responses are separated according to their PSTHs and morphology and labeled as PHL: phase-locked (cells with CFs under 1.2 kHz that have no anatomical data), PL: primary-like, PL_N : primary-like with notch, SBC: spherical bushy cells, GBC: globular bushy cells, NON-PL: nonprimary-like. Figure from Joris *et al.* (1994), reprinted with permission from The American Physiological Society.

cluster and have been found in both spherical and globular bushy cells.

Gap junctions allow fast continuous transmission between the cells unlike the chemical synapses that work on the principal of releasing and binding of neurotransmitters, which is not instantenous. The transmission via chemical synapses is stochastic in nature and dependent on the arrival of a presynaptic action potential. On the other hand the transmission via electrical synapses happens instantaneously and conductance of the electrical synapse channel is not dependent on the membrane potential.

Weakly coupled oscillator theory states that if oscillators with a similar oscillation frequencies are connected to each other, their oscillations are going to synchronize Hoppensteadt and Izhikevich (2012). In the biophysical domain, this can be translated as, if oscillating cells that have similar characteristic frequencies are connected to each other via fast transmission, they will synchronize eventually. The fast transmission between the cells can be interpreted as gap junctions.

Since changing the gap junction strength between the cells in an intact tissue would be hard to achieve experimentally, Sharp *et al.* (1992); Perez Velazquez (2003) connected two cells via patch clamps to simulate the gap junction connection. The firing patterns of the cells are synchronized by increasing the gap junction strength (Fig. 1.18). Gap junctions are hypothesized to enable synchronization between connected cells (Fukuda and Kosaka, 2000; Migliore *et al.*, 2005). In Fukuda and Kosaka (2000) a population of GABAergic neurons located in hippocampus that are connected through both chemical and dentrodentritic gap junctions are inspected while Migliore *et al.* (2005) investigates the distal gap junction's effect on synchronization of mitral cells using biophysically detailed cell models. Although Devor and Yarom (2002); Mercer *et al.* (2006); Curti *et al.* (2012); Yaeger and Trussell (2016) inspect the effect of gap junction on the firing of cells connected via gap junctions that are located in different parts of the brain, such as inferior olivary nucleus, hippocampus, mesencephalic trigeminal (MesV) nucleus and in DCN, their effect on the biophysically detailed network models of bushy cells is yet to be explored. This research question is the focus of the next three chapters of this thesis.

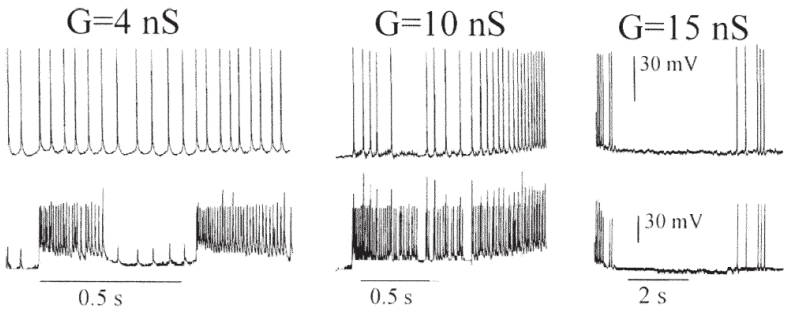

Figure 1.18: The figure shows how the increasing gap junctions results in a synchronization of the cells firing. The cells are coupled artificially and G represents the strength of the gap junction conductivity in nS. As the gap junction strength increases, the firing behavior of both cells (top row and bottom row) are synchronized. Reprinted with permission of Taylor & Francis, from Perez Velazquez (2003) ©2003.

Chapter 2

Modeling the Effects of Gap Junctions on The Excitability of a Network of Phasic Firing Bushy Cells

2.1 Abstract

Information propagation from cell to cell in the nervous system is performed via chemical or electrical synapses. While electrical synapses (a.k.a. gap junctions) are less common in the mammalian brain than chemical synapses, they have been found to play crucial roles in a numerous brain mechanisms, particularly in enhancing synchronization in networks of cells. The effects of gap junctions on neural excitability, information propagation, and synchronization enhancement have been well investigated in various brain areas through biophysical and computational studies, but the majority of these have focussed on neurons that exhibit tonic or oscillatory firing behaviors.

In this study, the effects of gap junctions on the excitability of a type of phasic firing cells are inspected using biophysically detailed neural-network models of bushy cells in the auditory brainstem. Models of fully connected cell clusters of different sizes were created to investigate the effect of gap junctions on the excitability of the cells by applying suprathreshold and subthreshold current injections and single synaptic inputs. Action potential (AP) generation inside clusters was examined across a range of gap-junction connection strengths. The effects of gap junctions and the leakage current on the excitability are compared. Gap junctions with small to medium conductivities help cells in clusters fire an AP even when they receive subthreshold inputs, either from direct current injection or synaptic input. Simulations show that

the time window over which one cell receiving suprathreshold input can help a connected cell receiving subthreshold input to fire an AP tends to increase as the gap junction strength is increased. However, as the gap-junction conductivity between the cells and the number of connected cells increases, the threshold for AP creation also increases. For very high gap-junction conductivities, the cells become very difficult to excite, although current-injection simulations indicate that model excitability is more sensitive to changes in the leakage current than the gap-junction strength. Overall, the results of this modeling study show a strong effect of gap junctions on the excitability of phasic firing bushy-cell networks.

2.2 Introduction

The electrical information propagation between cells in the nervous system can happen two ways; indirect communication through chemical synapses, which relies on releasing and binding of neurotransmitters, or direct electrical communication through channels on the cell membrane, such as electrical synapses. Unlike chemical synaptic transmission, the electrical connection between the cells is instantaneous and continuous (Alcamí and Pereda, 2019). One category of these connections is called gap junctions. Connexins (Cx) are the main type of cell-membrane proteins that form gap junctions in mammals, and Cx36 allows bidirectional communication between electrically coupled cells. Cx36 expression in the mammalian brain is well documented (Dermietzel and Spray, 1993; Condorelli *et al.*, 2000; Belluardo *et al.*, 2000; Bennett and Zukin, 2004).

The investigation of the effects of gap junctions on cell activity has a long history. Watanabe (1958) took recordings of the large cells of the heart of Japanese lobsters and found evidence of the spread of excitation. When a large cell was subjected to a depolarized current injection, another cell that makes a protoplasmic connection to it also showed a lower amplitude, delayed depolarization. Slow oscillations seen in the first cell were apparent at the neighboring cell with decreased amplitude and a phase shift. Considering these recordings, Watanabe (1958) concluded that cells are electrically connected, and this connection allows small oscillatory potentials to appear in the neighboring cell. Getting (1974) and Getting and Willows (1974) investigated the role of electrical synapses on burst firing of the trigger group neurons (TGN) of marine mollusk. Intracellular recordings from these neurons showed the spread of excitation to neighboring TGN cells. A current-clamp mechanism was used to equalize the membrane potential of two cells, which effectively acted as an electrical coupling. A model for the electrotonic interactions within the TGN populations was developed, and the simulation results showed that the reduction in input resistance and time constant depended on the number of coupled cells and the coupling strength. The

functional significance of gap-junction connections in microcircuits of the inferior olivary nucleus is studied in De Zeeuw *et al.* (1998) and found to have prominent effects on the contributions of the inferior olivary nucleus to timing and learning hypotheses. Li and Hatton (1996) investigated the effect of gap junctions on the burst firing of rat supraoptic neurons. Although these neurons fire phasically in some circumstances, they also exhibit oscillatory burst firing, and Li and Hatton (1996) found that gap junctions allowing the fast transmission of Ca^{+2} is an important mechanism for this burst-firing activity.

The effects of gap junctions on the cell and network behavior in various regions of the brain has also been explored with computational studies. In Traub *et al.* (1999, 2002) the effect of axon-axon gap junctions on the burst firing was explored by a network model that only had gap junction connections and no chemical synapses. First, the evidence of axonal gap junctions was presented in CA1 pyramidal neurons, and a network model was created to investigate the effects of different gap junctional properties on the excitability of single cells and the propagation of excitation in a cell cluster. Manor *et al.* (1997) built a Hodgkin–Huxley-type cell model with a low-threshold calcium channel and a leakage channel, and checked the oscillatory behavior of the cell in response to a range of leakage and calcium-channel conductances. Manor *et al.* (1997) found that coupling two non-oscillating cells via gap junctions can result in oscillatory behavior. Loewenstein *et al.* (2001) built a similar model to Manor *et al.* (1997); the model consisted of a calcium channel, a leakage channel, and a calcium-dependent potassium channel. The cells were connected via gap junctions, and the study concluded that besides helping synchronization and allowing an immediate communication between the cells, gap junctions can be a mechanism for generating subthreshold oscillations. Traub *et al.* (2011) investigated the role of the gap junctions in burst firing of CA3 pyramidal neurons, and concluded that the chemical synapses are not the only mechanism that helps to produce burst firing in these cells. Perez-Velazquez *et al.* (1994) experimented on the effect of gap junctions on CA1 pyramidal cell firing behavior, and found that blocking the gap junctional connections significantly decreases the spontaneous firing of the cells, which indicates the suppression of seizure-like activity. In summary, gap junctions can influence cell network behavior in a variety of ways that are dependent on the cell types and their connectivity.

The effectiveness of the transmission between the electrically coupled cells can be shown via coupling coefficients (CCs). CC is calculated as the ratio between the peaks of the subthreshold steady-state membrane potentials of cells when a subthreshold DC current is injected into one cell while the other cell does not receive any current injection and only receives excitation through electrical synapses. The effect of gap junction strength on CC can be seen in Fig. 2.1. Although electrical coupling provides excitation from neighboring cells, it also affects the excitability of the cells, and

the loading effect should be taken into consideration. The loading effect is described as electrically coupled cells having reduced input resistance because of the current leakage caused by gap junctions, which effectively act as current sinks. As the electrical coupling strength between the cells increases, the input resistance of the cells decreases; hence, the cells become less excitable (Getting, 1974; Getting and Willows, 1974). On the other hand, reduced input resistance lowers the cell membrane time constant, which allows the cells to respond faster.

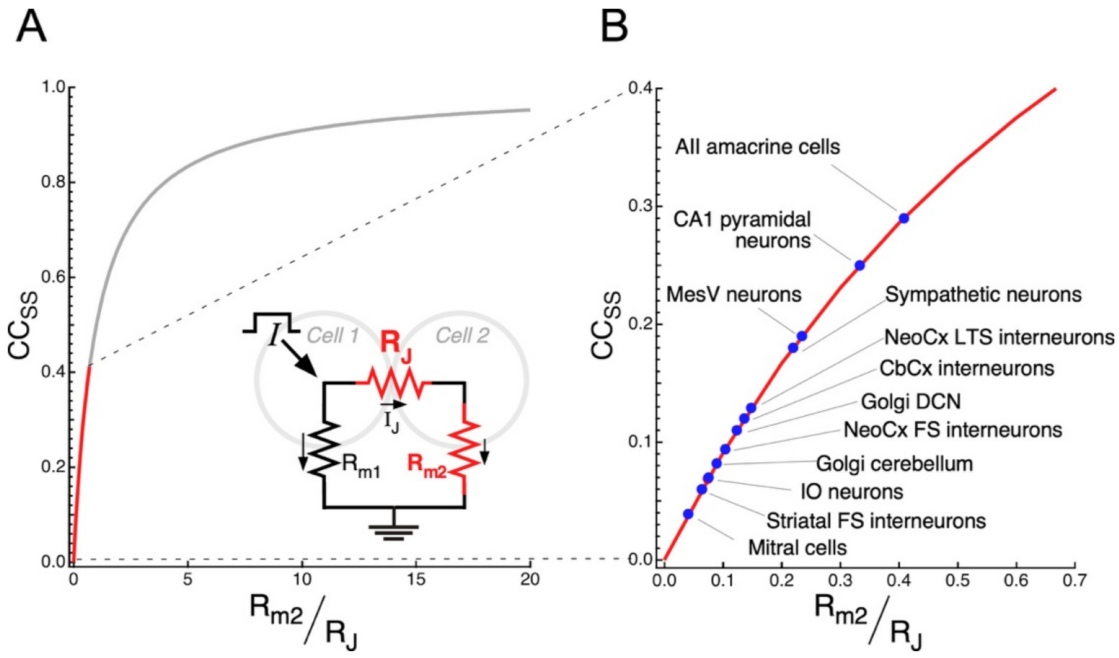

Figure 2.1: (A) Demonstration of the setup used for calculation of coupling coefficients (inner panel) and physiologically recorded coupling coefficient values of a variety of cells. CC_{SS} stands for the steady state coupling coefficient, calculated from the ratio of the membrane potentials of cells that receive DC current injections. R_J indicates junctional resistance while R_{m1} and R_{m2} are membrane resistances of the electrically coupled cells. (B) A zoomed in portion of the figure presented in (A). Some example CC_{SS} values for a variety of cells are provided. Reprinted with permission of MDPI Open Access Journals, from Curti *et al.* (2022) ©2022.

The effects of gap junction connections on the network functionality depend on the type of cells that are connected electrically and the type of gap junction connections. An functionality of the brain is to perform sound localization. Fine-timing information is crucial for computing interaural time differences (ITD) and phasic firing cells, which are able to fire an action potential fast at the onset of the signal, are

presumed to play a major role on this behavior since they are able to preserve fine-timing information effectively (Joris *et al.*, 1998; Grothe *et al.*, 2010). In this study, the effects of gap junctions on phasic firing cells were explored using biophysically detailed neural-network models. The cell models were based on the bushy cells of ventral cochlear nucleus (VCN), since the transient and persistent K^+ channels prevent bushy cells from firing repetitively, making them phasic firing neurons (Manis and Marx, 1991; Schwarz and Puil, 1997; Rothman and Manis, 2003; Zhang *et al.*, 2024). Bushy cells are one of the main cell types in the ventral cochlear nucleus, and they make soma-somatic and dendro-somatic gap junctions (Gómez-Nieto and Rubio, 2009, 2011). Bushy cells have low membrane resistances, hence they have fast membrane time constants (Cao *et al.*, 2007). Bushy cells send precisely timed information to the higher levels of the central auditory nervous system, which is used as a cue for sound localization. The strength of gap-junction conductance or coupling coefficients for bushy cells are yet to be recorded physiologically. Therefore, the strength of gap-junction connections in this study is a free parameter, so that the effects of gap junctions on the behavior of phasic firing cells were inspected over a range of gap-junction connection strengths. Although the roles of gap junctions in stellate and fusiform cells of the dorsal cochlear nucleus (DCN) are well documented and studied (Wouterlood *et al.*, 1984; Apostolides and Trussell, 2013), the functional significance of gap junctions in the VCN, especially on bushy cells, are yet to be discovered. This study aims to explore the effect of gap junctions on the excitability and firing activity of phasic-firing cell models, which has implications for the functionality of bushy cells of the VCN. Since a gap-junction channel acts as a current sink, its effect on excitability is compared with the effect of leakage current. Current injections and single synaptic inputs were provided to clusters with different size and configurations to examine the effect of gap junctions on phasic-firing cells in a mechanistic manner. A more complete bushy-cell network model is presented in Chapter 3, which includes acoustically-driven excitatory auditory-nerve fiber (ANF) inputs and inhibitory synaptic inputs from brainstem interneurons. The effect of gap junctions on the synchronization of spherical and globular bushy cell models in response to pure-tone acoustic stimuli are inspected in that chapter.

2.3 Methods

The phasic-firing bushy-cell models used in this study were connected via gap junctions as shown in Fig. 2.2. Each cell model consisted of a high-threshold K^+ current, I_{HT}, a low-threshold K^+ current, I_{LT}, a fast Na^+ current, I_{Na}, a fast inactivating potassium current, I_{A}, a hyperpolarization-activated cation current, I_{h}, and a leakage current, I_{leak}. The membrane potential was calculated as shown in Eq. 2.1.

Let k be the number of cells in a fully connected structure and $\mathbb{K}$ be the set of numbers $\mathbb{K} = \{1, 2, 3, 4, \ldots, k \mid k \in \mathbb{Z}^+\}$. The membrane voltage equations of cell n within the set $\mathbb{K}$ can be written in general form:

$$C_m \frac{dV_{\mathrm{n}}}{dt} = -(I_{\mathrm{HT_n}} + I_{\mathrm{LT_n}} + I_{\mathrm{Na_n}} + I_{\mathrm{A_n}} + I_{\mathrm{h_n}} + I_{\mathrm{lk_n}} + I_{\mathrm{syn_n}} + I_{\mathrm{gap_n}} - I_{\mathrm{ext_n}}) \quad (2.1)$$

The cell models were connected via a fixed resistor, which acted as a gap-junction connection that electrically coupled the membrane voltages. This connection was implemented into the equation as $I_{\mathrm{gap_n}}$. For every $n \in \mathbb{K}$, if we define $\mathbb{M} = \mathbb{K} - \{n\}$, the $I_{\mathrm{gap_n}}$ was defined as:

$$I_{\mathrm{gap_n}} = g_{\mathrm{gap}} \sum_{m \in \mathbb{M}} (V_{\mathrm{n}} - V_{\mathrm{m}}) \quad (2.2)$$

where V_{m} is the membrane potential of the m^{th} cell. The model received excitatory and inhibitory synaptic inputs via the synaptic channel:

$$I_{\mathrm{syn_n}} = g_{\mathrm{syn_n}}(V_n - V_{\mathrm{syn}}) \quad (2.3)$$

where V_{syn} is the reversal potential. For inhibitory inputs $V_{\mathrm{syn}} = -75$ mV and for excitatory inputs $V_{\mathrm{syn}} = 0$. $g_{\mathrm{syn_n}}$ is the change in the conductivity of the synaptic channel caused by the spikes coming from the presynaptic cells. In this chapter, only excitatory synaptic currents are investigated–the role of inhibition will be explored in Chapter 3. The change in the conductivity is modeled as a double exponential function with a rise time of $\tau_{\mathrm{rise}} = 0.05$ msec and a fall time $\tau_{\mathrm{fall}} = 0.4$ msec with a peak of $\bar{g}_{\mathrm{exct}}$. The decay time constant for bushy cells used in this study was based on Xie and Manis (2017b). The model could also receive direct current injections via $I_{\mathrm{ext_n}}$.

The phasic firing cell model used in this study was based on the Hodgkin–Huxley-type Xie and Manis (2013b) bushy cell models, which are modified versions of Rothman and Manis (2003) type models. Equations for the model's ion channels are provided in Appendix A. MATLAB's built-in ODE solver `ode45` was used with a time step of 10 µs.

Two types of connection scenarios were explored in this study. First, a fully connected cluster model was created consisting of an arbitrary number of cells that were connected via gap junctions. Second, a "connected clusters" structure explored the idea of two fully connected clusters, with one cell shared between the two clusters, which allowed for the spread of excitation through one cluster to another. A visual representation of the connection types is provided in Fig. 2.3.

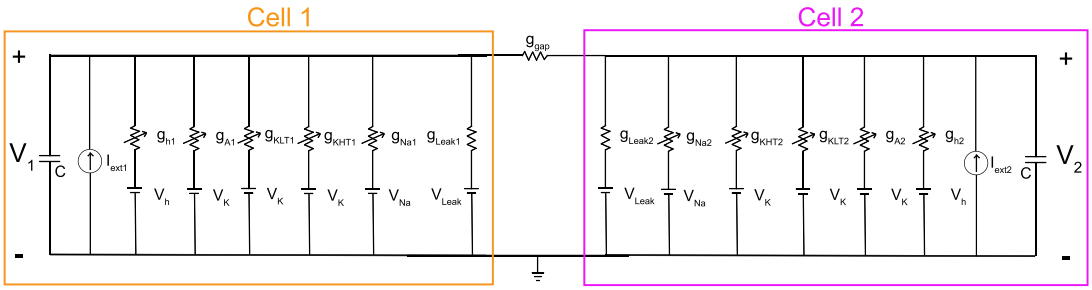

Figure 2.2: A circuit diagram showing two Hodgkin–Huxley-type cell models connected via gap junctions. The ion channels are modelled as parallel branches in the circuit. Each voltage-gated ion channel is represented as a variable conductance and a reversal potential, while the passive channels, such as the leakage current, are shown as a fixed conductance and a reversal potential. The membrane capacitance is modelled as a parallel branch consisting of a single capacitance component in the circuit. The current injection is represented as a current source on a parallel branch.

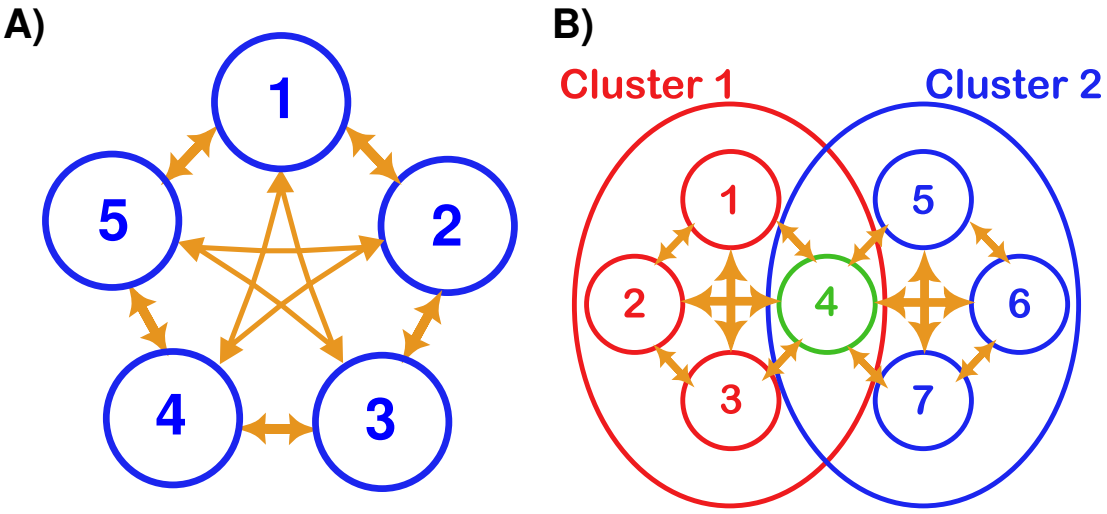

Figure 2.3: Visual representations of A) five fully connected phasic firing cells and B) two fully connected clusters of phasic firing cell models which share a single cell. Orange arrows indicate bidirectional gap junction connections between the cells. No inhibitory inputs are implemented in these models. The number of cells in the clusters can be set to any arbitrary number.

2.4 Results

The effects of gap junctions on the coupling coefficients in a pair of electrically coupled cells is demonstrated first. The minimum amount of current injection and synaptic input needed to initiate an AP on different sized clusters, where one cell received suprathreshold input while all the other cells in the cluster received subthreshold inputs, is also presented. Then, how gap junctions allow the spread of excitation inside and between fully connected clusters is demonstrated. Lastly, the effects of leakage current and gap junctions on the excitability of phasic firing cells in clusters are compared.

2.4.1 Gap Junctions Help the Spread of Excitation Within and Between Fully Connected Clusters of Phasic-Firing Cell Models

Fig. 2.4 shows the effect of gap junctions on steady state coupling coefficients of two electrically coupled phasic-firing bushy-cell models. Different levels of DC current injections were applied to check the effect of current-injection levels on the coupling-coefficient values over a range of g_{gap} values. The relationship between the coupling coefficient and g_{gap} was sigmoidal, with the coupling coefficient approaching 1 for very high g_{gap} values, which indicated lossless transmission between the cells, but never reached it. Different subthreshold current-injection levels resulted in almost identical curves.

When cell models were connected via gap junctions, they affected the membrane potentials of each other, because the gap junction connection is bidirectional. How gap junctions allow the spread of excitation was inspected by connecting two or more phasic-firing cell models via gap junctions to form clusters that received current injections and single synaptic inputs as excitation. In Fig. 2.5, simulation results of two connected bushy cells receiving suprathreshold and subthreshold current injections are presented. When $\text{g}_{\text{gap}} = 0$ nS, which means the cells were not electrically coupled, the AP produced by the first cell, which received a suprathreshold input (1000 pA), did not cause any perturbations in the membrane potential of the second cell, which did not receive any current injections (Fig. 2.5A). When g_{gap} was increased to 12.5 nS, Cell #1 caused a change in the membrane potential of Cell #2, as a delayed spikelet can be seen in the membrane potential (Fig. 2.5B). When the gap junction strength was kept the same and the second cell received a subthreshold input (500 pA), it produced an AP with the help of the excitation spread through the gap junction (Fig. 2.5C). Panels D-F of Fig. 2.5 show the effect of gap junction connections on the excitability of the cells when two connected bushy cells received suprathreshold current injections at t = 10 msec (Cell #1) and t = 15 msec (Cell

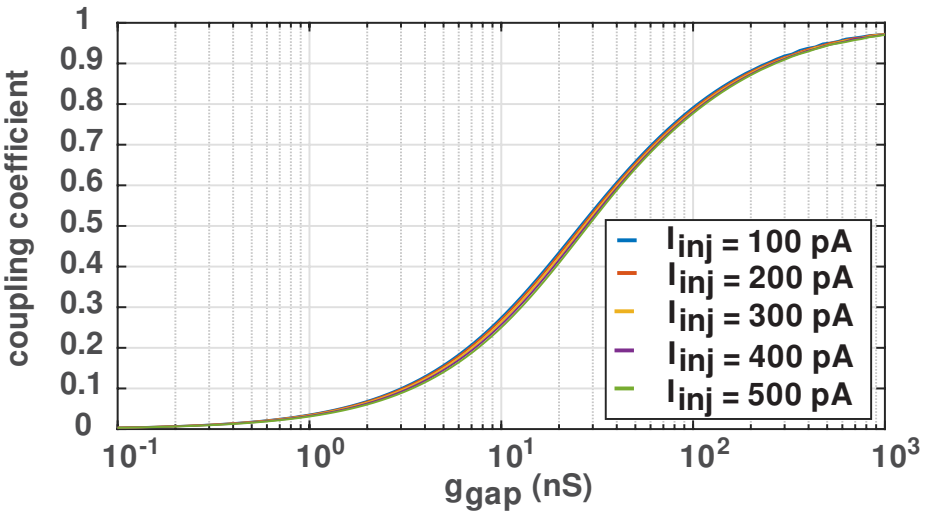

Figure 2.4: The effect of gap junctions on the steady state coupling coefficient. A pair of phasic firing cell models are connected via gap junctions to obtain results presented in this figure. The curves show the progression of coupling coefficients with respect to a range of gap junction connection strengths. Different curves indicate the coupling coefficients calculated by presenting subthreshold current injections to the same model.

#2). At $g_{\text{gap}} = 12.5$ nS, these APs caused a perturbation at the membrane potential of the other cell. When g_{gap} was increased to 50 nS, both cells fire an AP twice. The second AP is able to be produced by cells because the strong gap junction connection was enough for the AP produced by one cell to help the other cell to produce an AP. The APs produced by both cells, caused by suprathreshold current injections, had reduced amplitudes relative to the case with $g_{\text{gap}} = 0$ because the increased gap-junction strength decreased the cell excitability and the level of injected current was kept the same. As the strength of gap junction connection was increased even further, both cells stop firing an AP, even though they received enough excitation through current injections to produce an AP in cases when there were no gap junctions, because the excitability of the cells was decreased by the strong gap-junction connection.

Figure 2.6 shows the effects of gap junctions on excitability when two cells received single synaptic inputs. Similar to the current-injection simulation results, when the cells were not connected via gap junctions, the Cell #2 that received a suprathreshold input ($\overline{g}_{\text{exct}} = 45$ nS) had no effect on the Cell #1. When a gap junction connection was included, Cell #2 helped Cell #1 to fire an AP even though Cell #1 received a subthreshold synaptic input ($\overline{g}_{\text{exct}} = 20$ nS). Fig. 2.6 also shows the effect of the gap junctions on the firing behavior of the cells when both cells received suprathreshold synaptic inputs. When the gap junction strength was low, although APs produced by

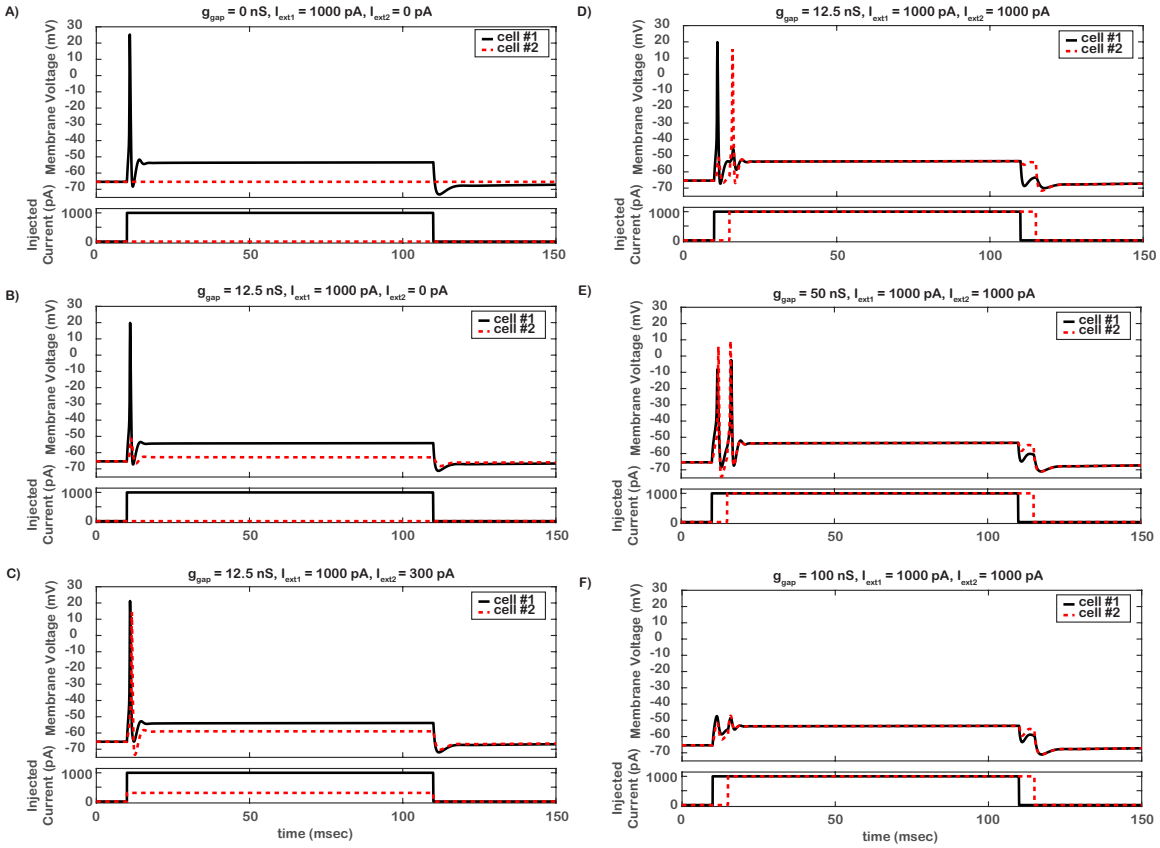

Figure 2.5: Simulations of a **pair** of connected cells that receive suprathreshold and subthreshold current injection inputs. (A) Cells are not connected with a gap junction. When Cell #1 is injected with a suprathreshold input (1000 pA), it creates an action potential, but Cell #2 remains inactive. (B) When a moderate strength of gap junction connection is introduced, even though Cell #2 is not stimulated with an injected current, the membrane potential is perturbed. (C) When Cell #2 is injected with a subthreshold input (500 pA), which would not cause the cell to spike by itself without gap junction connections, an action potential is produced with the help of the gap junction connection. (D), (E) and (F) show how different strengths of gap junctions affect the firing behavior of the cells when both cells receive suprathreshold inputs at different times. When both of the cells are injected with suprathreshold inputs at different times, both are able to fire an AP when a moderate strength of gap junction connection is present (12.5 nS). When g_{gap} is increased to 50 nS, both cells fire two action potentials, i.e., the action potentials spread from cell to cell. At 100 nS, even though both cells are injected with levels of injected currents that would cause them to fire an AP for lower g_{gap} values, both cells fail to produce action potentials.

a cell affected the membrane potential of the other cell, it was not enough to initiate an AP. When the gap junction strength was increased, both cells fired twice because the excitation spread through gap junction was enough to elicit another AP. Because the gap junctions decreased the excitability of the cells, the spike amplitudes were decreased. As the gap junction strength increased even more, because the excitability of the cells decreased, both cells stopped firing even though the level of excitation they received through synaptic inputs was enough to initiate an AP when gap junctions were not included.

We investigated the time duration over which the gap junctions could help a cell that received a subthreshold current injection to produce an AP in a pair of electrically coupled cells, the results of which are shown in Fig. 2.7. In these simulations, Cell #1 received a suprathreshold synaptic pulse ($\overline{g}_{\text{exct}} = 45$ nS) while Cell #2 received a subthreshold synaptic pulse ($\overline{g}_{\text{exct}} = 24$ nS, close to firing threshold so that small g_{gap} strength helped the Cell #2 to fire an AP). The length of the effective time window was calculated as the maximum time difference between the onsets of the subthreshold and supratheshold current injections that could still generate an AP in Cell #2. The time window to increased monotonically, but nonlinearly, with increasing gap-junction strength (Fig. 2.7E). Another effect of the gap-junction strength on the excitability of Cell #2 was that as the gap-junction strength increased, the AP was produced earlier, indicating that the cell-membrane potential reached the threshold faster. In these simulation settings, when g_{gap} exceeded 18 nS, Cell #1 caused Cell #2 to fire an AP at the onset of the suprathreshold synaptic input (see Fig. 2.7D), hence the time-window length was undefined for values of $g_{\text{gap}} \geq 18$ nS and is not included in the Fig. 2.7E.

The results presented in this section until this point were for a pair of connected cells. Figure 2.8 shows the membrane voltage traces of eight fully connected cells. Even though Cell #2 was the only cell that received suprathreshold input (1000 pA) in the cluster, with the help of gap junction connections, it was able to help all the other cells fire an AP, even though they all received subthreshold inputs (500 pA). Since the gap junction strengths were the same between all the cells and the size of subthreshold current injections provided to the cells were the same, all the cells in the clusters, apart from Cell #2, had the same membrane-voltage traces.

In Figure 2.9, how gap junctions allowed the spread of excitation both within and between two fully connected clusters that shared a single cell (as in Fig. 2.3B) is introduced. In this setting, only Cell #2 received suprathreshold current injection (1000 pA) while all the other cells in both clusters received subthreshold current injection (500 pA). All the gap junction connections between the cells were at the same level. The $g_{\text{gap}} = 3.3$ nS was enough for the cells in Cluster #1 that received a subthreshold input to fire an AP because the excitation spread through Cell #2 provided enough excitation. Cell #4 was not able to fire an AP since it was connected

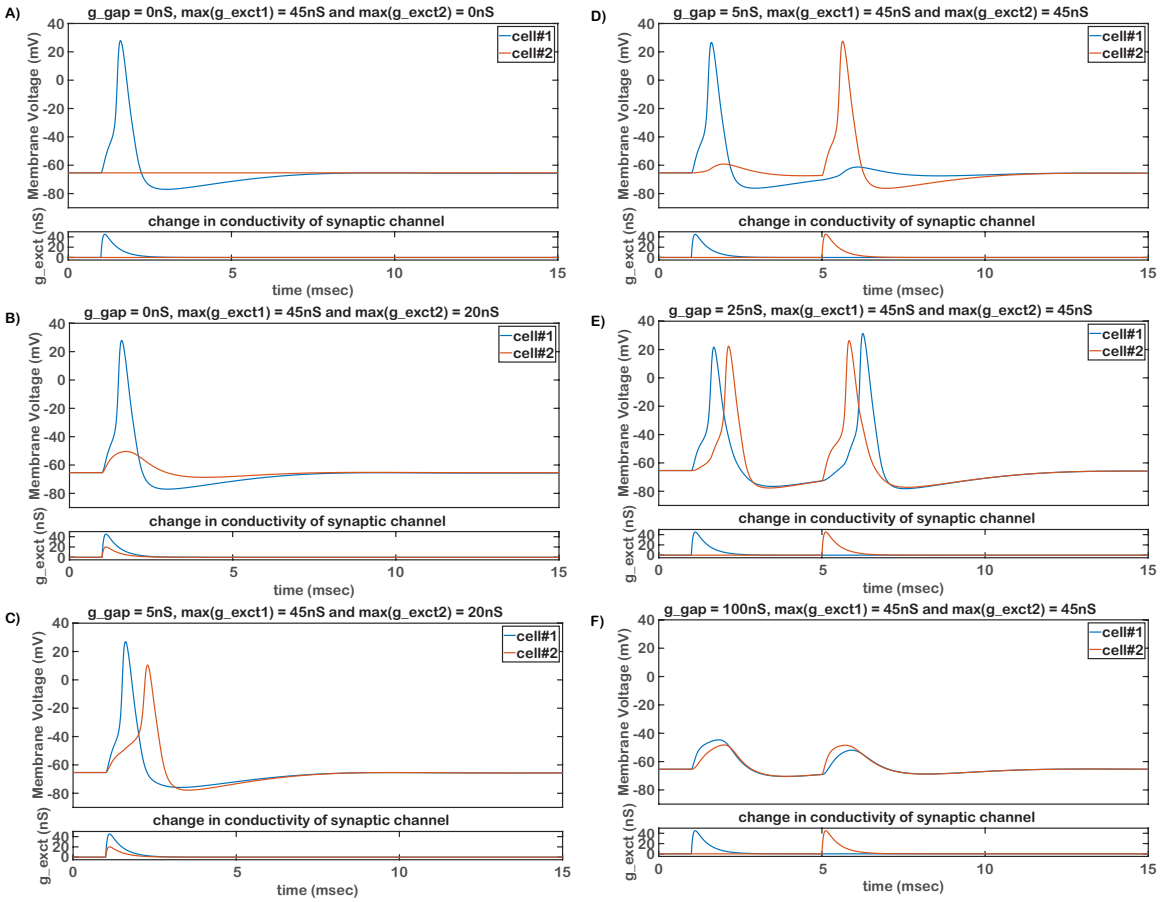

Figure 2.6: Simulations of a **pair** of connected cells that receive simultaneous suprathreshold and subthreshold synaptic inputs. (A) Cells are not connected with a gap junction. When the first cell receives a suprathreshold synaptic input ($\overline{g}_{\text{exct}} = 45$ nS), it fires an action potential, but the second cell remains inactive. (B) When second cell receives a subthreshold synaptic excitatory input ($\overline{g}_{\text{exct}} = 20$ nS), the membrane is perturbed but not enough to create an AP. (C) When gap junction introduced and cells are connected, even though the second cell receives a subthreshold input (which would not cause the cell to spike by itself) an action potential is created with the help of the gap junction connection. (D), (E) and (F) show how different strengths of gap junction connections affect the firing behaviour of the cells. When both of the cells are introduced to a suprathreshold input, both are able to fire with a moderate gap junction strength. When g_{gap} is increased to 25 nS, both cells fire two action potentials, i.e., the action potentials spread from cell to cell. At 100nS, even though both cells are injected with suprathreshold inputs, both cells fail to create an action potential.

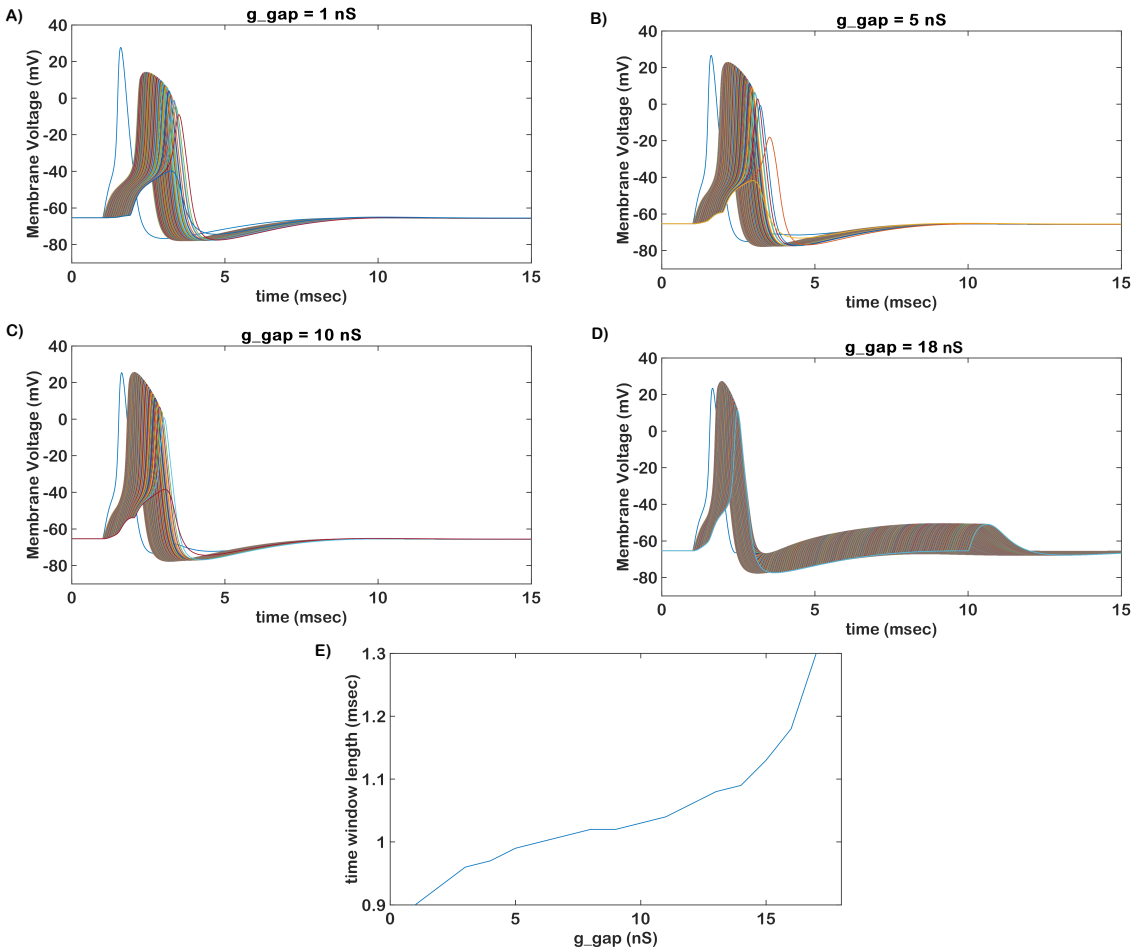

Figure 2.7: (A), (B), (C) and (D) visualizes the width of the time window where a cell in a **pair** of electrically coupled cells that receives suprathreshold synaptic input ($\overline{g}_{\text{exct}} = 45$ nS) input helps the cell in the cluster that receives subthreshold ($\overline{g}_{\text{exct}} = 24$ nS) input at different times to fire an AP. A range of g_{gap} strengths are inspected to understand for how long the suprathreshold input that Cell #1 receives effects the Cell #2 that receives suprathreshold input. Each instance of spiking behavior Cell #2 is superimposed on the same plot to visualize the progression in time. (E) shows the width of the time window in milliseconds for a range of g_{gap} values. As gap junction strength increases, the effect of suprathreshold input on the cell that receives subthreshold input also increases in a nonlinear manner.

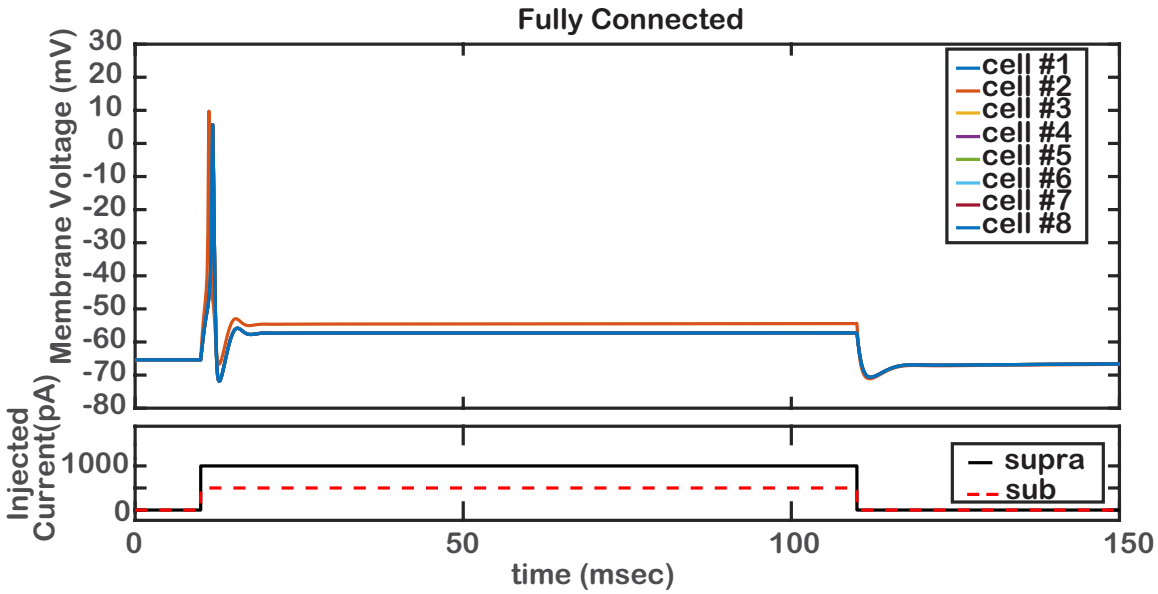

Figure 2.8: The membrane voltage traces of **eight cells** in a **fully connected** structure. The Cell #2 receives a suprathreshold input (1000 pA) while the other cells in the structure receive subthreshold input (500 pA). In this setting, the gap junction conductance is enough to initiate action potentials in the other cells. Since the connection's strength between each cell is the same, the cells which receive subthreshold inputs show the exact same behaviour (hence the membrane voltage traces are on the top of each other).

to 6 cells and the number of cells in a fully connected cluster was another deciding factor in cell excitability, apart from the g_{gap} strength. In this setting, none of the cells in the Cluster #2 produced an AP because the excitation spread through the first cluster via Cell #4 and the gap junction strength was not enough to exceed firing threshold. When gap junction strength was increased to 12.5 nS, all the cells in the Cluster #1 fired an AP, including Cell #4, and this gap junction strength was also enough for the excitation to spread between clusters and help all the cells in Cluster #2 fire an AP. The amplitude of the AP in Cell #2 was largest because it received the direct suprathreshold input while the cells other than Cell #4 in Cluster #1 had APs with amplitudes close to the AP produced by Cell #2. The amplitude of the APs produced by the cells in Cluster #2 were lower than the AP produced by Cell #4.

2.4.2 Gap Junctions Substantially Affect the Excitability of the Phasic-Firing Bushy-Cell Models

In Fig. 2.10, the minimum current-injection needed to produce an AP by the cells in a fully connected setting is shown. In these simulations, only one cell of the fully connected cluster received a suprathreshold current injection of 1000 pA while other cells in the cluster received subthreshold inputs. The effects of gap junctions and the number of cells on the minimum current-injection needed to produce an AP in fully connected clusters was explored. The suprathreshold current value was chosen to be substantially above the threshold for the bushy-cell model without gap junctions. Although different suprathreshold levels resulted in different surface shapes, the effects of gap junctions and the number of cells in the fully connected cluster on the excitability of the cells were qualitatively similar. Fig. 2.10 indicates that when the cluster size was kept the same, as the g_{gap} increased, the minimum amount of current injection level needed by the cells that received subthreshold input to produce an AP decreased. At high g_{gap} strength, in small size clusters, the cells in the cluster did not need to receive any current injection to produce an AP because the strong gap junction connection allowed them to received enough excitation from the cell that receives a suprathreshold input. As the size of the cluster increased, the excitability of the cells decreased and the amount of input needed to produce an AP for the cells that receive subthreshold input increased. For cluster sizes smaller than 4, the effect of gap junctions on the excitability was monotonic. For larger clusters, the increase in gap junctions decreased subthreshold current injection needed to produce an AP in cells that received subthreshold inputs, until moderate gap junction strength levels were reached. As gap junction strength increased even further, the decrease in the cell excitability reduced the AP amplitude on the cell that received suprathreshold input, hence providing less excitation to the cells in the cluster that received subthreshold

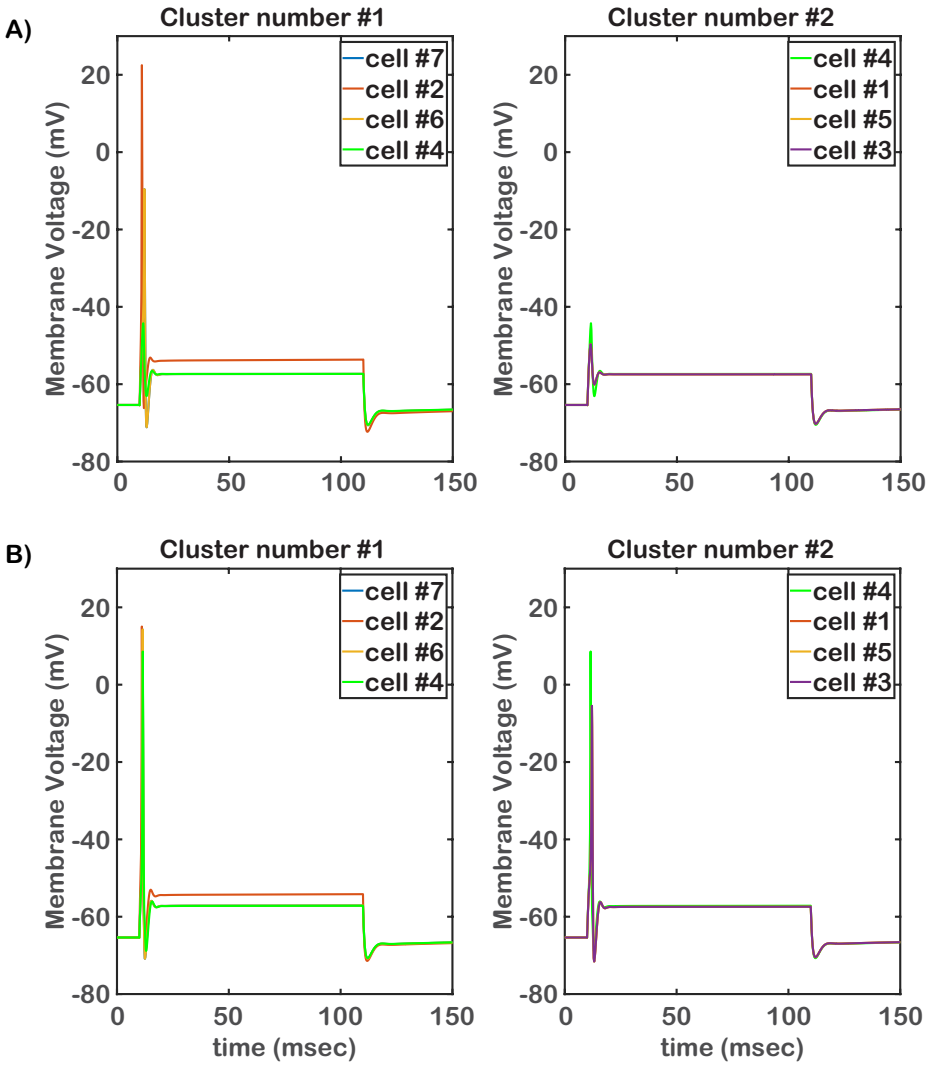

Figure 2.9: In a **cluster** connection setting where two clusters with four interconnected cells sharing a common cell, when Cell #2 in the Cluster #1 is introduced with a suprathreshold input (1000 pA), while every other cells in both clusters are introduced with subthreshold ones (500 pA), a gap junction connection with a strength of $g_{\text{gap}} = 3.3nS$ is enough to initiate a spike in the cells inside the cluster. Since Cell #4 is a member of both of the clusters, the excitability of the cell is less than the other cells which receive subthreshold inputs. Therefore, this cell is not able to create an action potential and fails to carry the action potential produced in the Cluster #1 to Cluster #2. B) In the same **cluster** setting, when the g_{gap} increased to a value of 12.5 nS, the spike in Cell #2 is enough to initiate a spike in Cell #4. And this gap junction strength is enough to carry the action potential created in the Cluster #1 to Cluster #2 via Cell #4.

input. Therefore, combined with the effect of decreased excitability, a slightly higher subthreshold current injection was needed by the cells that received subthreshold inputs to produce an AP.

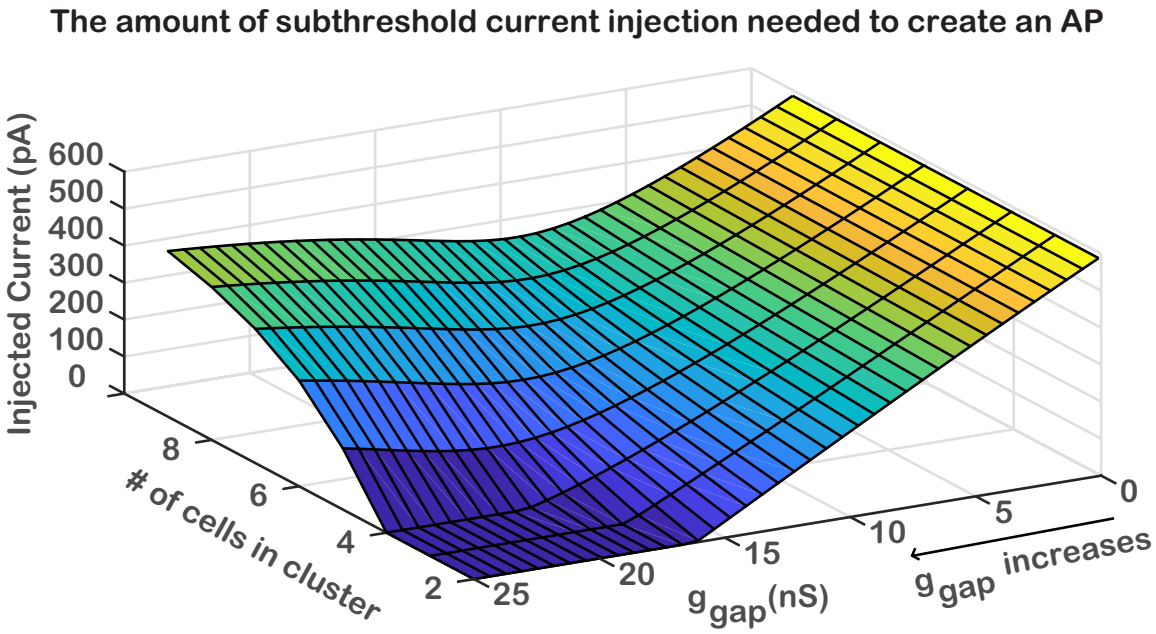

Figure 2.10: The minimum amount of current injection input needed to initiate a spike in a **fully connected cluster** setting where one cell receive suprathreshold current injection input of 1000 pA while all other cells in the cluster receive simultaneous subthreshold current injection inputs. The change in the amount of necessary current injection level is inspected across different number of fully connected cells and the strength of gap junction connections.

The amount of synaptic input needed to produce an AP by cells in a fully connected cluster that received subthreshold input is shown in Fig. 2.11. In these simulations, only one cell in the fully connected cluster received a suprathreshold synaptic input while the other cells in the cluster received subthreshold synaptic input. The values shown on the z-axis are the peak synaptic conductance ($\overline{g}_{\text{exct}}$). The effects of g_{gap} and the number of cells in the cluster on the excitability of the cells had similar trends to the current-injection simulations (Fig. 2.10). When the number of cells in the cluster was kept the same, as the g_{gap} increased, the amount of minimum synaptic input needed for cells in the cluster that received subthreshold input decreased. And at high g_{gap} values, these cells did not need to receive any synaptic input to produce an AP, the spread of excitation coming through gap junctions was enough. When the g_{gap} strength was kept the same, as the number of cells in the cluster increased,

the excitability of the cells decreased, as they needed stronger subthreshold synaptic inputs to produce an AP. The non-monotonic effect of gap junctions on the cell excitability can also be seen in Fig. 2.11. For smaller cluster sizes, as gap junction strength increased, the amount of subthreshold synaptic input to produce an AP by the cells in the cluster that receive subthreshold input decreased. As the gap junction strength increased even further, the subthreshold synaptic input needed to initiate an AP started to increase again for the reasons explained in the previous paragraph.

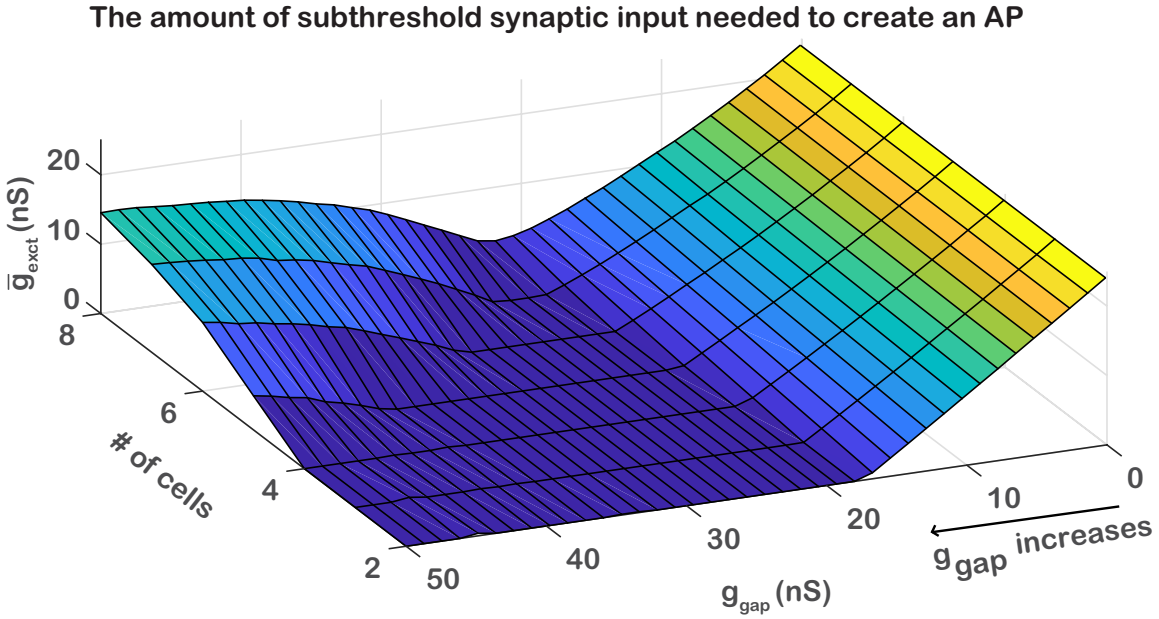

Figure 2.11: The minimum amount of subthreshold synaptic input needed to initiate a spike in a **fully connected cluster** setting, where one cell receive suprathreshold input while all the other cells receive simultaneous subthreshold inputs. The change in the amount of necessary subthreshold input is inspected across different number of fully connected cells, and the strength of gap junction connections.

2.4.3 Comparison of the Effect of Gap Junctions and Leakage Current on the Excitability of the Phasic-Firing Cell Models

In previous sections, the impact of gap junctions on the excitability of the phasic firing cell models and how they allow the spread of excitability was explored. The leakage current implemented in the models are also known to effect the model's excitability. In this section, the effects of leakage current and gap junctions on excitability were

compared by inspecting the maximum membrane voltage over a range of g_{gap} and g_{leak} strengths. These simulations were performed with the "connected cluster" structure presented in Fig. 2.3B, and the maximum membrane voltages of each cell in the clusters were inspected. Cell #2 received a suprathreshold input of 1000pA while all the other cells in both clusters received a subthreshold input of 500pA. When both g_{gap} and g_{leak} were lower, the cells in the Cluster #1 produced APs. While the strength of g_{gap} was enough for the AP in Cell #2 to help the other cells within its cluster to fire, it was not enough for the AP's effect to be carried over to the cells in Cluster #2 (Fig. 2.12A). When the g_{gap} value increased enough, the effect of an AP produced in Cluster #1 carried over to Cluster #2 via their joint Cell #4, causing the cells in Cluster #2 to also produce APs. Another noticeable effect of higher g_{gap} values was that the amplitude of APs produced in Cells #6 and #7 was higher than in Cell #2, which received the suprathreshold input (Fig. 2.12B). When g_{gap} increased even further, the excitability of the cells decreased to a level where all the cells failed to produce an AP, despite the low g_{leak} value ((Fig. 2.12C). A high g_{leak} value also decreased the cell excitability to an extent that none of the cells in the clusters could produce an AP (Fig. 2.12D).

2.5 Discussion & Conclusion

In this study, the effect of gap junction connections on the excitability of phasic-firing cells was inspected using biophysically detailed neural models of bushy cells of the VCN. Inspecting the effect of gap junctions provided insight into how electrical coupling can affect the function of individual cells and networks as a whole. Phasic-firing cells have a distinguishable firing pattern, in that they tend to fire APs only at the onset of the stimulus and do not fire in a sustained manner for an ongoing stimulus. Therefore they are able to preserve the fine-timing information of stimulus onsets, of cycle-by-cycle periods of low-frequency stimuli, and of cycle-by-cycle periods of amplitude modulations in an ongoing stimulus, all of which can provide ITD cues for sound localization. Bushy cells of the VCN are phasic-firing cells that provide input to the superior olivary complex, where ITD cues are first processed. Bushy cells are known to make soma-somatic gap junction connections. Hence, exploring the effects of gap junctions on phasic-firing cell models is crucial to understand the role of bushy cells in sound localization.

Fully connected cell clusters of different sizes were created in order to examine how gap junctions spread the excitation inside and between connected cell clusters. Current injection and single synaptic inputs were provided to cells inside clusters. Simulation results indicated that gap junctions allowed the cells in the cluster to affect the membrane potentials of surrounding cells directly. The strength of gap junction

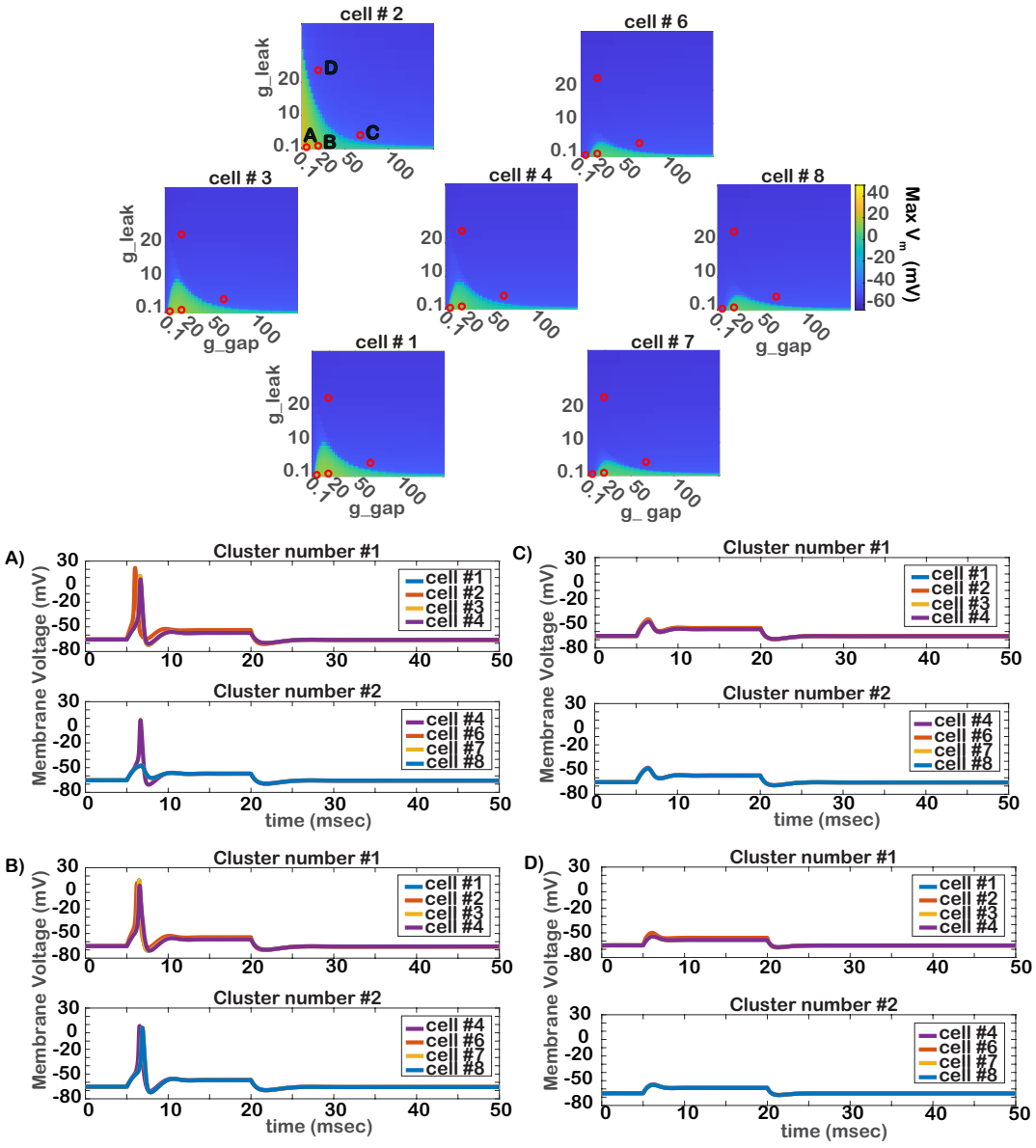
cell # 2
cell # 6
cell # 3
cell # 4
cell # 8
cell # 1
cell # 7
g_leak
g_gap
Max V_m (mV)
A)
B)
C)
D)
Cluster number #1
Cluster number #2
Membrane Voltage (mV)
time (msec)
cell #1
cell #2
cell #3
cell #4
cell #6
cell #7
cell #8

Figure 2.12: The top set of panels shows the maximum of the membrane voltages of the individual cells in the cluster structure presented in Fig. 2.3B for a range of g_{gap} and g_{leak} values. Cell #2 of Cluster #1 receives a suprathreshold input of 1000 pA while all other cells in both clusters receive subthreshold inputs of 500 pA. Comparison of the effect of gap junctions and leakage current on the excitability of the bushy cell models. A, B, C and D show the membrane voltage traces of the individual cells in the clusters for the specific g_{gap} and g_{leak} instances, highlighted as red dots. A) For low g_{gap} and g_{leak} levels, the Cell #2 in Cluster #1 is able to fire an AP and the amount of g_{gap} is enough for this AP to affect the other cells in Cluster #1 to fire an AP, but it is not high enough to help the cells in Cluster #2 to fire an AP. B) When g_{gap} is increased even more while the g_{leak} is kept the same, all of the cells in both clusters are able to produce an AP. C) At high g_{gap} and low g_{leak} values, all of the cells in both clusters stop firing an AP even though Cell #2 receives a level of current injection that is able to allow it to fire an AP in case of lower g_{gap} values since the gap junctions decreases the excitability. D) At high g_{leak} and low g_{gap} values, all of the cells in both clusters stop firing an AP since the leakage current decreases the excitability of the cells.

connections and the size of the clusters dictate the effectiveness of the spread of excitation among cells. Figures 2.5 and 2.6 show how gap junctions allow the spread of excitation between a pair of electrically coupled cells. As the strength of gap junction connections increased, the cell that receives a suprathreshold input affected the membrane potential of the other cell in the cluster more strongly. Although gap junctions help the cells that receive subthreshold input to produce an AP, they also decrease excitability because of the loading effect. Hence, when talking about gap junctions and excitation, the threshold for AP generation and the amplitude of the APs produced by the cells in the cluster should also be considered.

Results shown in Fig. 2.4 indicate that the effectiveness of subthreshold coupling between cells was a nonlinear function of the gap-junction strength and was not dependent on the level of subthreshold excitation. The effectiveness of the coupling is more complex when AP generation is considered. Figures 2.10 and 2.11 show that gap junctions and the number of cells in the clusters both effect the minimum amount of input needed to initiate an AP by the cells in the cluster that receive subthreshold input, when only one cell in the cluster received a simultaneous suprathreshold input in a fully connected setting. As the gap junction strength increased, the minimum amount of input needed by the other cells to initiate an AP decreased. At higher g_{gap} values, the excitation coming from the cell that received suprathreshold input was enough to initiate a spike in the other cells without the need for a simultaneous subthreshold input when the number of fully connected cells was low. But it is

evident in Figures 2.5, 2.6 and 2.12 that as g_{gap} increased even further, the cells lost their ability to produce an AP even when they received a level of input that would cause them to fire at low g_{gap} values. As the number of cells in the fully connected cluster increased, the excitability of the cells in the cluster decreased as the amount of necessary subthreshold input needed to initiate an AP increased. The dependency of excitability of the bushy cell models on the number of connected cells and the degree of coupling agreed with the results presented in Getting (1974) and Getting and Willows (1974) on burst-firing trigger-group neurons.

Watanabe (1958) investigated the effects of the distal gap junctions on the spread of excitation on large cells of Japanese lobster hearts, while our study investigated the effect of soma-somatic gap junctions. They identified the contribution of distal gap junctions on the spread of excitation as a delayed spikelet with a decreased amplitude and a low coupling coefficient. Since our study is more focused on soma-somatic gap junctions, stronger communication between cells with shorter delayed spikelets and higher transmission efficiency, which can be seen as a pre-junctional spike causing a large displacement in post-junctional cell-membrane potential, was expected and confirmed in our simulation results.

Another perspective on the contribution of gap junctions to the excitability of the cells is presented in Fig. 2.7. A pair of phasically firing cells were electrically coupled via gap junctions, and one cell was excited with a suprathreshold input while the other cell received a subthreshold input at different times. As the gap junction connection was increased, the AP in one cell helped initiating a spike in the other cell for a longer period of time. Also, as g_{gap} increased, the second cell's potential reached the threshold value for AP generation more quickly, hence the traces got closer to the AP produced by the cell that received suprathreshold input.

Weakly coupled oscillator theory states that weak coupling of individual oscillators can allow the oscillations in coupled cells to synchronize. Hence, the effect of electrical coupling on the oscillatory cells are of interest and studied extensively to understand epileptiform activity in the brain. Li and Hatton (1996) and Traub *et al.* (2002) investigated the role of gap junctions on the epileptiform activities which are induced by oscillatory bursting and concluded that gap junctions can play a role in this mechanism. Traub *et al.* (2002) explored the effect of gap junctions on the burst-firing activity of hippocampal pyramidal cells, which can show tonic or burst-firing activity, and found that gap junctions can allow the cells to produce burst firing even when there is no synaptic activity. Although the cells investigated in Li and Hatton (1996) can exhibit phasic firing, they also show burst-firing activity and the scope of that study was to investigate the effect of gap junctions on the burst firing. Shaffer *et al.* (2017) examined the effects of gap junctions on a chain of electrically coupled cell models that can show tonic or burst firing behavior. They found that gap junctions can allow the models to switch between tonic and burst-firing modes, depending

on the strength of gap-junction connections and intrinsic firing behavior of each cell. Since there are cells in the brain that can show both tonic and burst firing behavior, investigating the effects of gap junctions on the tonic firing cells can also give useful insights on information processing in the brain.

Our study extended the examination of the effects of gap junctions to phasically firing cells that do not exhibit intrinsic oscillations or burst firing even when connected via gap junctions. Since phasically firing cells are able to produce a fast action potential at the onset of incoming stimuli, they can encode fine-timing information in their firing patterns, and such timing cues are important in the function of bushy cells of the VCN. Investigating the effect of gap junctions on the cell excitability and the information propagation between coupled cells is crucial since gap junctions allow fast transmission between cells, and phasically firing bushy cells in the VCN are known to make soma-somatic gap-junction connections. Figure 2.7 shows how gap junctions can help the enhancement of the fine-timing coding in a population of phasic-firing cells with close characteristic frequencies by allowing different cells in the cluster to fire action potentials in a short time frame, even though some of the cells might receive delayed stimulation.

The nonlinearity of the effect of gap junctions on the excitability of cells is prominent also in Figs. 2.5 and 2.6. Even though an increase in g_{gap} helped both of the cells fire an action potential twice at moderate gap-junction strengths, the amplitude of the AP was lower than for low gap-junction strengths. At high values of g_{gap}, the excitability of the cells decreased enough to cause both of the cells to stop firing an AP. Since the gap junction channels effectively acted as current sinks, their effect on the excitability was compared with the leakage current. Figure 2.12 shows that the effect of g_{leak} on the excitability of the cells was stronger than g_{gap} because the amplitude of the action potentials declined faster as g_{leak} increased.

Gap junctions contribute to the function of cell networks depending on the biophysical properties of the cell. The role of gap junctions in producing subthreshold oscillations in a network of phasic firing cells is documented in Li and Hatton (1996). This chapter explored the effect of gap junctions on cell excitability and the spread of both subthreshold and supratheshold responses in networks of phasically firing bushy cells. The effect of gap junctions on the function of a more detailed bushy-cell network is explored in Chapter 3. The bushy cells of VCN are phasic-firing cells that send fine-timing information to the superior olivary complex, where fine-timing information coming from both ears is compared to compute ITDs (Joris *et al.*, 1998; Grothe *et al.*, 2010). Auditory nerve fibers (ANFs) have synchronized responses to incoming auditory stimuli, tending to fire at specific phases of the periodic inputs. The synchronization behavior in bushy cells is even more prominent than in ANFs (Joris *et al.*, 1994; Joris and Smith, 2008; Rhode, 2008; Dehmel *et al.*, 2010; Wei *et al.*, 2017). Because gap junctions are hypothesized to increase synchronization of neurons

in general (Fukuda and Kosaka, 2000; Migliore *et al.*, 2005; Curti *et al.*, 2012), the potential role of gap junctions to contribute to the synchrony enhancement of bushy cells is studied extensively in the next chapter.

2.6 Acknowledgments and Funding

This research was funded by NSERC Discovery Grants RGPIN-2018-05778 & RGPIN-2024-05888 (ICB) and was enabled in part by support provided by Compute Ontario (`www.computeontario.ca`) and the Digital Research Alliance of Canada (`www.alliancecan.ca`). The authors thank Dr. Laurel H. Carney for the suggestions to investigate gap junction connections in bushy cells and their potential effect on synchronization. No AI tools were used in generating the data, producing the figures, or writing or editing the manuscript.

2.7 Author Contribution

Conceptualization: ICB. Methodology: MY and ICB. Software: MY and ICB. Validation: MY and ICB. Formal Analysis: MY and ICB. Investigation: MY and ICB. Data Curation: MY. Writing - Original Draft: MY and ICB. Writing - Review & Editing: MY and ICB. Visualization: MY and ICB. Supervision: ICB. Project Administration: ICB. Funding Acquisition: ICB.

2.8 Code and Data Availability

The model code can be found here:
github.com/bushy_cell_network_model_with_gap_junctions. To reproduce the findings, the data can be provided upon request.

2.9 Declarations

2.9.1 Conflict of Interest

The authors declare no conflicts of interest, in any form.

Chapter 3

Effects of Gap Junctions and Inhibition on the Synchronization of a Biophysically Detailed Neural-Network Model of Bushy Cells

3.1 Abstract

Purpose: Auditory-nerve-fiber (ANF) responses to sound are processed by several distinct neural circuits in the cochlear nucleus (CN). One of the main cochlear nucleus cell types that projects to higher auditory nuclei is bushy cells (BCs), which can be divided into two types, globular and spherical, depending on the shape of their soma and their innervation patterns. Apart from receiving excitatory inputs from ANFs and inhibitory inputs from D-Stellate and tuberculoventral cells, BCs receive excitation via gap junctions (a.k.a electrical synapses) from neighboring BCs. One of the distinctive features of the BCs is the enhancement of the synchronization behavior in ANFs. For globular BCs, which receive subthreshold inputs from many ANFs, a coincidence-detection mechanism is proposed, whereas for spherical BCs, the mechanism for the synchronization enhancement is still not fully understood.

Methods: In this study, fully connected bushy-cell network models were created. The effect of gap junctions on the synchronization of the BCs were inspected by connecting the membrane potentials of clusters of five fully-connected BCs.

Results: As the strength of the gap junction connections was increased within a given cell network, the synchronization was enhanced. The effects of inhibition on the synchronization were also explored and were found to be non-monotonic.

Conclusion: Synchronization index values of the simulated network models with different gap junction strength indicated that gap junctions can strongly contribute to the synchronization of models for both globular and spherical BCs.

3.2 Introduction

The CN is the first stage in the central auditory nervous system that receives sound stimuli from ANFs. Features that help the brain to localize and identify the sound are extracted by different types of cells residing in the CN. Two of the main types of cells are bushy cells and T-stellate cells (Cant and Benson, 2003). These cells are distinguished by their morphological structures and how they integrate the information coming from the ANFs that converge on them (Doucet and Ryugo, 2006; Young and Sachs, 2008; Typlt *et al.*, 2012; Campagnola and Manis, 2014; Manis *et al.*, 2019). The resulting difference in the responses of these cells allows different features to be extracted and propagated through parallel streams to higher levels of the central auditory nervous system (Oertel *et al.*, 2011; Joris *et al.*, 1998; Grothe *et al.*, 2010). Bushy cells have transient responses at the onset of acoustic stimuli (phasically firing), while T-stellate cells respond with a train of spikes (tonically firing) to an incoming stimulus (Oertel, 1983; Rhode, 2008; Oertel *et al.*, 2011). The precise firing of bushy cells allows fine-timing information to be conveyed to the medial superior olivary complex, where the information coming from both ears is compared for sound localization (Joris *et al.*, 1998; Grothe *et al.*, 2010). Bushy cells can be divided into two categories: spherical bushy cells (SBCs) and globular bushy cells (GBCs). The SBCs are located in rostral anteroventral CN and receives few ANF inputs while GBCs reside in caudal anteroventral CN and integrates a higher number of inputs coming from ANFs (Smith *et al.*, 1993; Spirou *et al.*, 2005; Cao and Oertel, 2010).

ANFs show synchronized firing behavior to incoming sinusoidal stimuli, which can be seen in the firing patterns of ANFs that tend to fire at specific phases of periodic stimuli. This synchronization behavior can be quantified by the synchronization index (a.k.a. vector strength) which is calculated from period histograms (Johnson, 1980). Phase-locking is even more prominent in the bushy cells of ventral CN (Joris *et al.*, 1994; Joris and Smith, 2008; Rhode, 2008; Dehmel *et al.*, 2010; Wei *et al.*, 2017). Figure 3.1 shows an example of synchronization enhancement in an extracellular recording from a fiber in the trapezoid body, which is likely coming from a bushy cell, compared to an ANF. Figure. 3.2 shows the maximum synchronization index scores of a population of VCN cells. These recordings are taken from the trapezoid body and are thought to originate from either globular or spherical bushy cells.

Different models of bushy cells have been proposed in the literature. Rothman and Young (1996) investigated the synchrony enhancement in GBCs with a shot-noise

threshold model and a membrane-conductance model. The paper mentioned the proposed mechanism of coincidence detection for synchrony enhancement and concluded that the synchrony enhancement seen in GBCs can be explained by large number of subthreshold inputs converging to GBCs. Rudnicki and Hemmert (2017) created a modified version of the GBC model initially proposed in Rothman and Manis (2003), to investigate the effects of the number of synaptic inputs and synaptic depression on the synchronization behavior. One of the main findings from this paper was that the number of converging ANF inputs has little effect on the synchronization index. On the other hand, the strength of entrainment is greatly effected by the number of ANF inputs. Ashida *et al.* (2019) developed an adaptable-threshold coincidence-detection model of GBCs that shows enhanced synchronization compared to the ANF input model. The model explored the effects of six model parameters on the firing rate and synchronization index of the GBC model. One of the findings of this study was that the number of inputs converging on the GBC model and the EPSC amplitude had the largest effects on vector strength amongst all free parameters. Although the coincidence-detection mechanism is a good candidate to explain the synchrony enhancement in GBCs, because they receive a large number of subthreshold inputs, it cannot be a feasible explanation for SBCs since they receive very few suprathreshold inputs (Joris and Smith, 2008). There are several SBC studies that inspected the effects of different configurations on the synchronization behavior of SBCs. Apart from creating a GBC model, Rothman and Young (1996) also explored an SBC model and proposed that a mix of suprathreshold and subthreshold inputs can account for the low-CF SBCs having high SRs and enhanced synchronization. Kuenzel *et al.* (2015) investigates the effects of inhibition on the synchrony using a modified Rothman and Manis (2003) SBC model and shows that the inhibition by itself is not enough for reaching high temporal precision seen in SBCs, but hypothesizes that a combination of large EPSCs and inhibition can result in improved synchronization. Koert and Kuenzel (2021) modeled the effects of the small dendritic inputs coming from ANFs on synchronization index and consider them as a plausible mechanism for the improvement of temporal precision of SBCs. Xie and Manis (2013b) investigated the effects of inhibition on the synchronization index of bushy and T-stellate cells of VCN and found that the inhibition has a strong effect on the firing probability of SBCs and caused a small but significant improvement of the synchronization index.

All of these previous GBC and SBC models have only implemented fast chemical synaptic inputs from ANFs and CN interneurons. However, immunolabeling studies (Gómez-Nieto and Rubio, 2009, 2011; Rubio and Nagy, 2015) indicate that the bushy cells of the ventral CN have soma-somatic connections. One type of these connections, known as gap junctions, suggests that these cells are electrically coupled. These connections allow the excitation to spread across the cells in a cluster and have been

found in both SBCs and GBCs. Gap junctions are hypothesized to enable synchronization between connected cells (Fukuda and Kosaka, 2000; Migliore *et al.*, 2005; Curti *et al.*, 2012). Although Devor and Yarom (2002); Curti *et al.* (2012); Yaeger and Trussell (2016); Mercer *et al.* (2006) inspect the gap junction's effect on the firing behavior of cells connected via gap junctions that reside in different parts of the brain, their effect on the biophysically detailed network models of bushy cells are yet to be explored. In this study, the effect of gap junctions on the synchronization behavior of the bushy cells are inspected by using a biophysically detailed neural-network model of bushy cells.

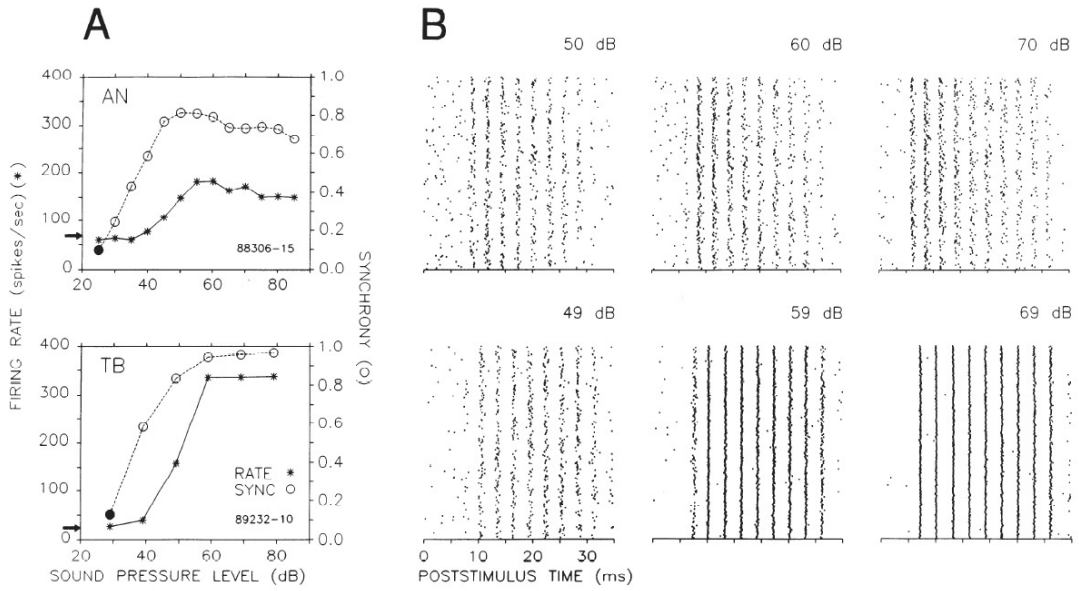

Figure 3.1: A) Firing rate and synchronization versus stimulus level plots of an ANF with a characteristic frequency (CF) of 350 Hz (top row) and a trapezoid body (TB) fiber with a CF of 340 Hz (bottom row). Fibers in the ascending pathways of the TB are believed to originate from bushy cells of the ventral CN. B) Raster plots showing the synchronization behavior in the firing patterns of an ANF (top row) and a TB fiber (bottom row). The synchronization enhancement behavior of the TB fiber compared to the ANF can be seen in the firing patterns, as the TB fiber fires in a more temporally-confined manner at each period of the stimuli. Figure from Joris *et al.* (1994), reprinted with permission from The American Physiological Society.

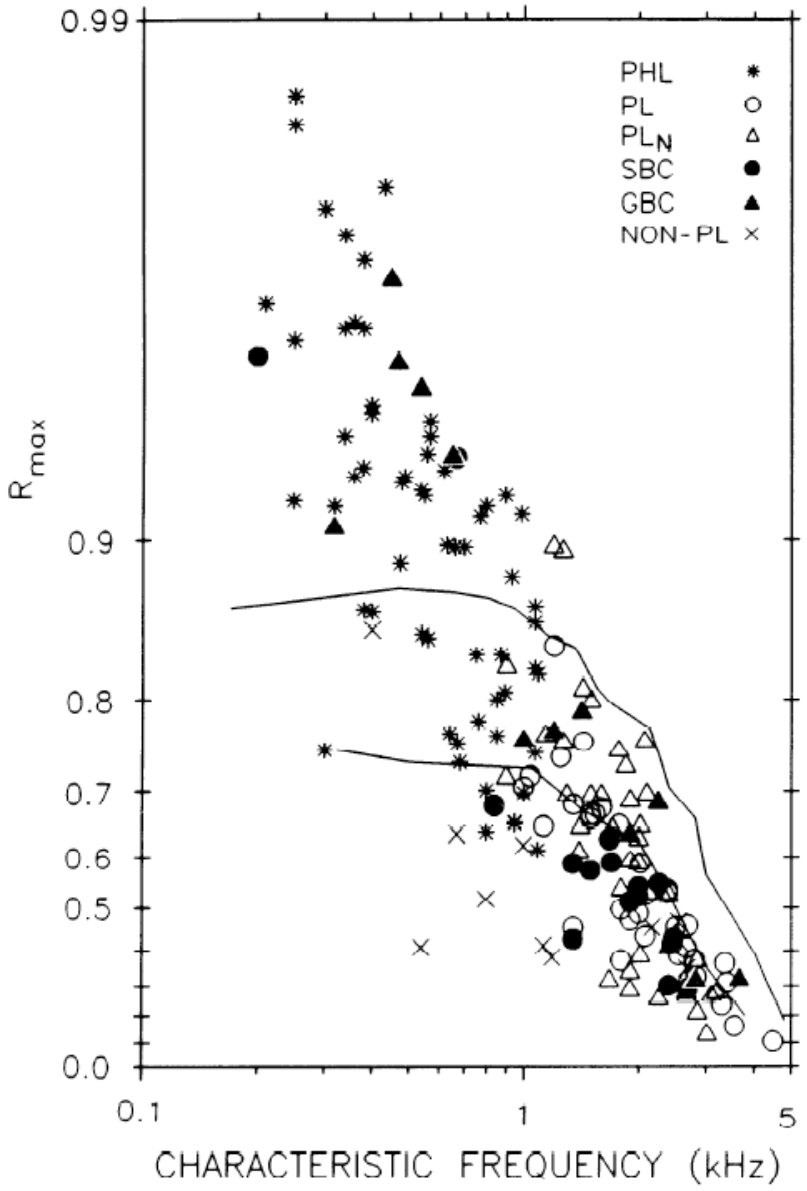

Figure 3.2: Maximum synchronization index values of a population of cells that projects through TB as a function of cells' CFs. The solid lines represent the upper and lower boundaries of synchronization index values of ANFs reported in Johnson (1980). Different cell types are identified according to their PSTHs and morphology and labeled as PHL: phase-locked (cells with CFs under 1.2 kHz that have no anatomical data), PL: primary-like, PL_N : primary-like with notch, SBC: spherical bushy cells, GBC: globular bushy cells, NON-PL: nonprimary-like. Figure from Joris *et al.* (1994), reprinted with permission from The American Physiological Society.

3.3 Methods

3.3.1 Biophysically Detailed Neural-Network Models of Bushy Cells of Ventral Cochlear Nucleus

The biophysically detailed neural network of bushy-cell models used in this study was based on Rothman and Manis (2003) and Xie and Manis (2013b).The cell models are single-compartment models without any dendrites. The bushy-cell models are connected to each other via gap junctions. A schematic representation of two bushy cells connected via gap junctions can be seen in Fig. 3.3. Gap junctions allow several bushy cells to be connected to each other in different configurations. The spread of excitation through the gap junctions in a pair of coupled cells is demonstrated in Supplementary Information Fig. B.1.

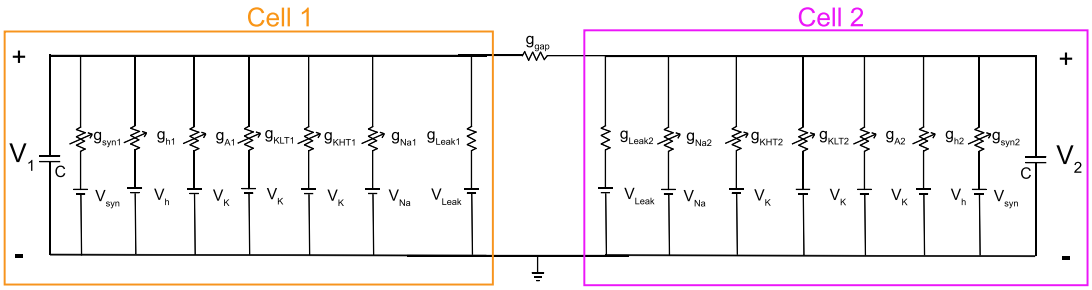

Figure 3.3: A circuit diagram showing two Hodgkin–Huxley type cell models connected via gap junctions. The ion channels are modeled as parallel branches in the circuit. Each voltage gated ion channel is represented as a variable conductance and a reversal potential while the passive channels such as the leakage current is represented with a fixed conductance and a reversal potential. The membrane capacitance is added as a parallel branch. The model receives excitatory and inhibitory chemical synaptic inputs through the synaptic channel.

From bottom to the top, the network is built of an ANF layer, a D-Stellate (DS) cell layer, a tuberculoventral (TV) cell layer and a bushy cell-layer (Fig. 3.4). The ANF layer provides excitatory inputs to all of the other layers in the network, the DS-cell layer provides broadband inhibition, and the TV-cell layer provides sharply tuned inhibition to the bushy-cell layer. The cells in the bushy-cell layer are also connected to each other via gap junctions. The range of convergence of excitatory and inhibitory inputs to the bushy cell layer can be found in Table 3.1 and Table 3.2. The SBC model receives 3 suprathreshold high-spontaneous-rate ANF inputs while the GBC model receives excitation from 12 subthreshold high-spontaneous-rate

ANFs. Liberman (1991) estimates that the number of ANF inputs converging onto GBCs is around 50, while Spirou *et al.* (2005) reports a range of 9 to 69 inputs, with a mean of 23 ANF inputs to GBCs. Spirou *et al.* (2005) argues that the number of inputs in Liberman (1991) might be an overestimate since the ANF terminals were not confirmed to make contact with the cell bodies in that study. In contrast, Cao and Oertel (2010) reports a much smaller number of only 5 inputs as most likely input count for GBCs. We conducted preliminary simulations with our GBC model testing a range of inputs from 4 to 52, in steps of 8. We found that 12 ANF inputs converging on our GBC model gave results most consistent with the physiological data, and this number is generally in line with the number of inputs estimated from the studies mentioned above. In this study, similar to the model described in Fig. 7 of Manis and Campagnola (2018), for DS and TV cells, only the excitatory inputs coming from ANFs were included. The glycinergic inhibitory synaptic connections and excitatory inputs coming from T-Stellate cells to DS cells (Ferragamo *et al.*, 1998), the inhibitory inputs to TV cells coming from DS cells, and the excitatory inputs coming from other T-Stellate cells (Zhang and Oertel, 1993) were not included in our model. DS cells received 12 high, 12 medium and 12 low-spontaneous-rate ANF inputs, while TV cells were innervated by 12 medium and 12 low-spontaneous-rate ANFs. In total, for SBC simulations, 1995 ANFs and 70 DS, TV, and SBC cell models were simulated. For GBC simulations, 2040 ANFs were simulated while the total numbers of simulated DS, TV, and GBCs were 70 again.

MATLAB 2023b.2 was used to simulate the cell models. The function `datasample` from the MATLAB Statistics and Machine Learning Toolbox was utilized to randomly select the synaptic inputs from the population of input cells with an appropriate statistical distribution of convergence parameters as given in Tables 3.1 and 3.2. This process was completed independently for each cell, such that different VCN cells could receive some common inputs by chance. The MATLAB function `randStream` was used to set the seed of the pseudorandom number generator to a fixed value at the start of each simulation, such that the connectivity patterns were identical across different simulations. MATLAB's built-in ODE solver `ode45` was used with a time step of 10 µs.

Table 3.1: Synaptic Convergence Parameters (number of cells)

	SBC	GBC	D-Stellate	TV
ANF	3	12	36	24
D-Stellate	7	7	0	0
Tuberculoventral	6	6	0	0

The bushy and tuberculoventral cell models were based on updated Rothman and

Table 3.2: Synaptic Convergence Range Parameters (octaves)

	Bushy	D-Stellate	TV
ANF	0.05	0.4	0.1
D-Stellate	0.208	N/A	N/A
Tuberculoventral	0.069	N/A	N/A

Manis (2003) models presented in Xie and Manis (2013b), while D-Stellate cell models were based on type12 models of Rothman and Manis (2003). Since the recordings in Xie and Manis (2013b) are taken at 34°C and the Rothman and Manis (2003) recordings are taken at 22°C, temperature scaling was applied to D-Stellate model to match bushy and tuberculoventral cell models. The temperature scaling applied to the conductivity and time constant parameters was as follows:

$$\mathrm{k_g} = 2^P \tag{3.1}$$

$$\mathrm{k_t} = 1/(3^P) \tag{3.2}$$

where

$$P = (\mathrm{T} - 22)/10 \tag{3.3}$$

and T is the temperature in °C. k_g is a scaling coefficient that is multiplied with the maximum conductivity of the channel, while k_t is a scaling coefficient that is multiplied with the channel time constant. The Q_{10} values for conductivity and time were 2 and 3, respectively.

The phenomenological model of the auditory periphery developed by Bruce *et al.* (2018) was used to provide the excitatory inputs. The cell models used in DS, TV, and bushy-cell layers were built from a high-threshold K^+ current, I_{HT}, a low-threshold K^+ current I_{LT} , a fast Na^+ current, I_{Na}, a fast inactivating potassium current, I_{A}, a hyperpolarization-activated cation current, I_{h}, and a leakage current, I_{lk}. The membrane voltage equation is given in Eq. 3.4. The parameters used to construct these models can be found in Table 3.3.

Excitatory and inhibitory synaptic inputs were provided to the models via I_{syn} current while a current injection can be applied to the models via I_{ext}.

Let k be the number of cells in a fully connected structure and $\mathbb{K}$ be the set of numbers $\mathbb{K} = \{1, 2, 3, 4, \ldots, k \mid k \in \mathbb{Z}^+\}$. The membrane voltage equations of cell n can be written in general form:

Table 3.3: Cell Model Parameters

	Bushy	D-Stellate	Tuberculoventral
C_m (µF)	26	12	35
g_Na (nS)	2300	1000	5800
g_HT (nS)	58	150	400
g_LT (nS)	80	20	0
g_A (nS)	0	0	65
g_h (nS)	30	2	2.5
g_lk (nS)	2	2	4.5
V_K (mV)	−84	−70	−81.5
V_Na (mV)	50	55	50
V_h (mV)	−43	−43	−43
V_lk (mV)	−65	−65	−72
V_syn_{exct} (mV)	0	0	0
V_syn_{inh} (mV)	−75	N/A	N/A

$$C_m \frac{dV_{\mathrm{n}}}{dt} = -(I_{\mathrm{HT_n}} + I_{\mathrm{LT_n}} + I_{\mathrm{Na_n}} + I_{\mathrm{A_n}} + I_{\mathrm{h_n}} + I_{\mathrm{lk_n}} + I_{\mathrm{syn_n}} + I_{\mathrm{gap_n}} - I_{\mathrm{ext_n}}) \quad (3.4)$$

For every $n \in \mathbb{K}$, if we define $\mathbb{M} = \mathbb{K} - \{n\}$, the $I_{\mathrm{gap_n}}$ can defined as:

$$I_{\mathrm{gap_n}} = g_{\mathrm{gap}} \sum_{m \in \mathbb{M}} (V_{\mathrm{n}} - V_{\mathrm{m}}) \quad (3.5)$$

where V_{m} is the membrane potential of the m^{th} cell. I_{gap} allows changes in the cells' membrane voltages to affect each other in a homotypic (bidirectional) way. Heterotypic gap junctions that allow transmission in one way which can be modeled as a diode also exist. However, the gap junctions seen in mammalians consist of Cx36 connexon, which is not voltage gated and only forms homotypic connections. This type of gap junction connection can be modeled as a passive conductance (Curti *et al.*, 2022). The current–voltage relationship of the gap junction channel is assumed to be linear. In Gómez-Nieto and Rubio (2011), bushy cells are observed to form clusters of 5–6 cells, hence in this study the fully connected networks are built by connecting 5 cells. A diagram of a fully connected network of five bushy cells used in this study is shown in Fig. 3.4. g_{gap} values explored in this study ranged from 0 nS to 100 nS. The upper limit was chosen based on preliminary simulations exploring bushy-cell excitability using single-synaptic-input stimuli for a pair of electrically coupled bushy cells without inhibitory connections. For gap junction strengths around 100 nS, both

cells in the cluster could not produce an action potential, even though they received the same level of synaptic input that allowed both cells to fire an action potential in the absence of gap junctions, so this value was chosen as the upper limit. The physiological feasibility of this range of values will be examined in the Discussion.

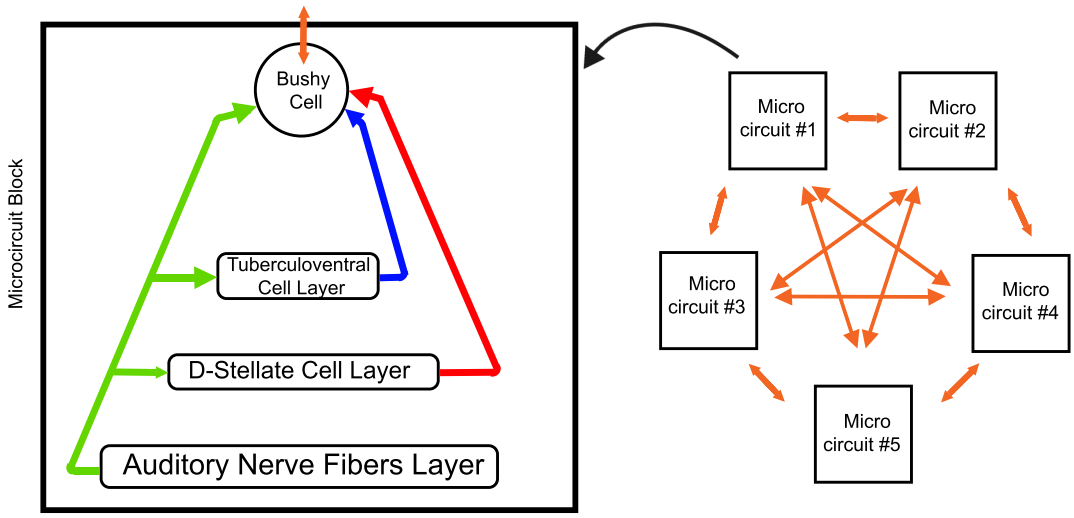

Figure 3.4: An example of a network model of five fully connected bushy cells. The excitatory inputs provided by ANFs to all the layers of the network are indicated with green arrows while the inhibitory inputs from DS and TV cells are shown as red and blue arrows respectively. Orange arrows indicate all of the bushy cells in the network are bidirectionally connected to each other via gap junctions.

The synaptic transmission was implemented in the model via the synaptic channel I_{syn}. A spike coming from a pre-synaptic cell causes a change in the conductance of the synaptic channel of the post-synaptic cell denoted as excitatory post synaptic currents (EPSCs) or inhibitory post synaptic currents (IPSCs). The changes in the conductance was modeled as a double exponential function with rise and fall time constants (τ_{rise} and τ_{fall}) and a peak of $\bar{g}_{exct}$. The peak values of the EPSCs and IPSCs for each cells were found via simulations and confirmed to be in the feasible range reported in physiological studies (Kuo *et al.*, 2012; Xie and Manis, 2017a; Wang *et al.*, 2019). The $\bar{g}_{exct}$ value presented in Table 3.4 for bushy cell models is the threshold value to produce an action potential when there were no gap junction connections between bushy cells. Since gap junctions significantly affect excitability of the bushy cells, the value of $\bar{g}_{exct}$ for bushy cells was empirically adjusted for each gap-junction conductance level to ensure that a spike was produced from a single synaptic input. The relationship between the threshold level and gap junction strength is shown in Fig. 3.5.

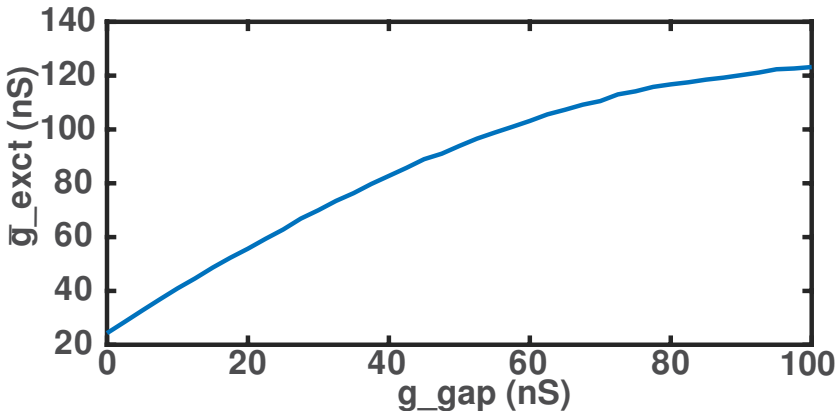

Figure 3.5: The threshold level of $\bar{g}_{exct}$ needed to produce a spike in a bushy cell changes in a non-linear manner with respect to the gap junction conductance value.

The τ_{rise}, τ_{fall} and $\bar{g}_{exct}$ values for each cell can be found in Table 3.4. To simulate the effect of suprathreshold and subthreshold inputs, the EPSCs and IPSCs were multiplied with k_exct = 3 if the connection was suprathreshold (spherical bushy cells) and k_exct = 0.7 if the connection was subthreshold (globular bushy cells). The effect of the strength of excitation on synchronization was explored by observing synchronization index scores over a range of k_exct. Because the D-Stellate and tuberculoventral cell models did not receive inhibition, the values in the table are represented as N/A. The maximum value of the conductance of the inhibitory synaptic channel $\bar{g}_{inh}$ is not provided in the Table 3.4 because it was a free parameter; its effect on the excitability and synchronization will be explored in the results. The EPSC decay time constant for bushy cells used in this study was in line with Xie and Manis (2017b), while the IPSC decay time constant parameter was close to the values reported in Xie and Manis (2013a), with the inhibitory time constants longer than the excitatory time constants, to be consistent with Xie and Manis (2013b). The EPSC time constants for DS and TV cells were in the ranges presented in Xie and Manis (2017b) and Gardner *et al.* (1999), respectively.

Table 3.4: Synaptic Transmission Parameters

	Bushy	D-Stellate	Tuberculoventral
$\tau_{rise_{exct}}$ (msec)	0.05	0.05	0.05
$\tau_{fall_{exct}}$ (msec)	0.4	0.2	0.2
$\tau_{rise_{inh}}$ (msec)	0.05	N/A	N/A
$\tau_{fall_{inh}}$ (msec)	4.88	N/A	N/A
$\bar{g}_{exct}$ (nS)	25	20	20

Population of ANFs with characteristic frequencies ranging from 200 Hz to 32 kHz with 1/32nd octave steps were created. The characteristic frequencies of the population of bushy cells also followed this frequency mapping. A cluster of five fully-connected bushy cells was created by connecting a central cell with 2 lower and 2 higher CF cells, assuming that the cells that are located close to each other would have similar CFs.

The stimulus used in model simulations was the same as presented in Joris *et al.* (1994). A 25-msec short tone burst with a rise and fall time of 3.9 msec was presented to the model 200 times with 75-msec pause between the tone bursts. Total duration of the stimulus used in the simulations was 20 seconds. To eliminate the effects of strong onset responses on the calculation of the synchronization index and firing rate, these were computed over a time window of 15 milliseconds starting 10 msec after the stimulus onset, consistent with Joris *et al.* (1994).

Action potential identification was done by MATLAB's built-in `findpeaks` function. The spike detection threshold was set to -20 mV. Large EPSPs occurring during the model's refractory period were excluded from being detected as spikes by setting the parameter `MinPeakDistance` to 1 msec. Supplementary Information Fig. B.2 shows an example SBC model membrane potential trace, with detected spikes indicated by red circles.

3.4 Results

This section will begin by presenting the SBC and GBC model results without gap junctions and inhibitory synaptic inputs. Then, the impact of gap junctions alone (without inhibitory inputs) on the synchronization and firing rates of the models are inspected, followed by an exploration of the effects of inhibition alone (without gap junctions). Finally, the combined effect of inhibition and gap junctions are examined.

3.4.1 SBC and GBC synchrony enhancement without gap junctions or inhibitory synapses

The firing rate and synchrony of SBC and GBC models was first examined without involving any effects of gap junctions or synaptic inhibition to determine how the baseline model responded to a periodic stimulus and how much enhancement can be obtained by just coincidence detection in the GBC model. Examples of firing rate versus level, synchrony versus level, and raster plots for models of an ANF and for models of an SBC and a GBC *without gap junctions or inhibitory synaptic inputs*, all with CFs of 340 Hz, can be seen in Fig. 3.6. The figure layout is arranged to allow direct comparison with the physiological data in Fig. 3.1. The synchronization

index plots indicate that a moderate synchrony enhancement behavior was exhibited by SBC models, and a strong onset response and a minor synchrony enhancement for the rest of the periodic stimulus for GBC models without inhibition or gap junctions. The synchrony enhancement in the GBC model was lower than the SBC model because the calculation of the SI values starts 10 msec after introducing the periodic stimuli to eliminate the contribution of the onset response to synchrony, following the methodology of Joris *et al.* (1994). As shown in Fig. 3.6, our GBC model without gap junctions and inhibition had a strong onset response and only had coincidence-detection like behavior for some periods of the stimulus and weakened synchrony for some periods. This kind of enhancement and weakening behavior occured as an alternating pattern at higher SPLs. This behavior obtained with an up-to-date biophysical model of a GBC contrasts with the synchrony enhancement throughout the duration of a periodic stimulus that has been generated in simpler coincidence-detection models. In comparison, the SBC model with just three suprathreshold ANF inputs fired in response to whichever ANF synaptic input comes arrived in each cycle of the stimulus, giving a modest enhancement of the synchrony. The reason behind the notch in the firing rate and synchrony plots at $\sim$ 100 dB SPL, which was not present in Fig. 3.1 because the plot did not show results higher than 80 dB SPL, was the C1/C2 transition behavior of the ANF model used in this study (Zilany and Bruce, 2006).

3.4.2 Increasing the gap junction strength enhances the synchronization of both SBC and GBC models

Fig. 3.7 shows the gap junction's effect on the synchronization index and firing rate of clusters of model SBCs and GBCs, each consisting of 5 fully connected cells (without inhibitory synaptic inputs). As the gap junction strength between the cells increased, SI values and firing rate also increased. For low g_gap values, the SBC model had higher firing rates and SI values than the GBC model. As g_gap increased, these differences between the two models diminished and both models reached high firing rates and SI values.

Maximum synchronization index values across a population of SBCs and GBCs are shown in Fig. 3.8. A fully connected network of 5 bushy cell models was simulated for both SBCs and GBCs. Bushy-cell models in a fully connected network receive a tone pip with the frequency equal to the CF of the central cell in the cluster. The other cells in the network also received the same frequency tone pip even though their CFs differed from the tone presented. No inhibition were present in the results presented in Fig. 3.8. As the CF of the cell increased, the maximum synchronization index value it reached decreased. The maximum SI values of simulated bushy-cell models decreased sharply at lower frequencies than what is seen in Fig. 3.2. A range of different model parameters such as the membrane capacitance and the time constant

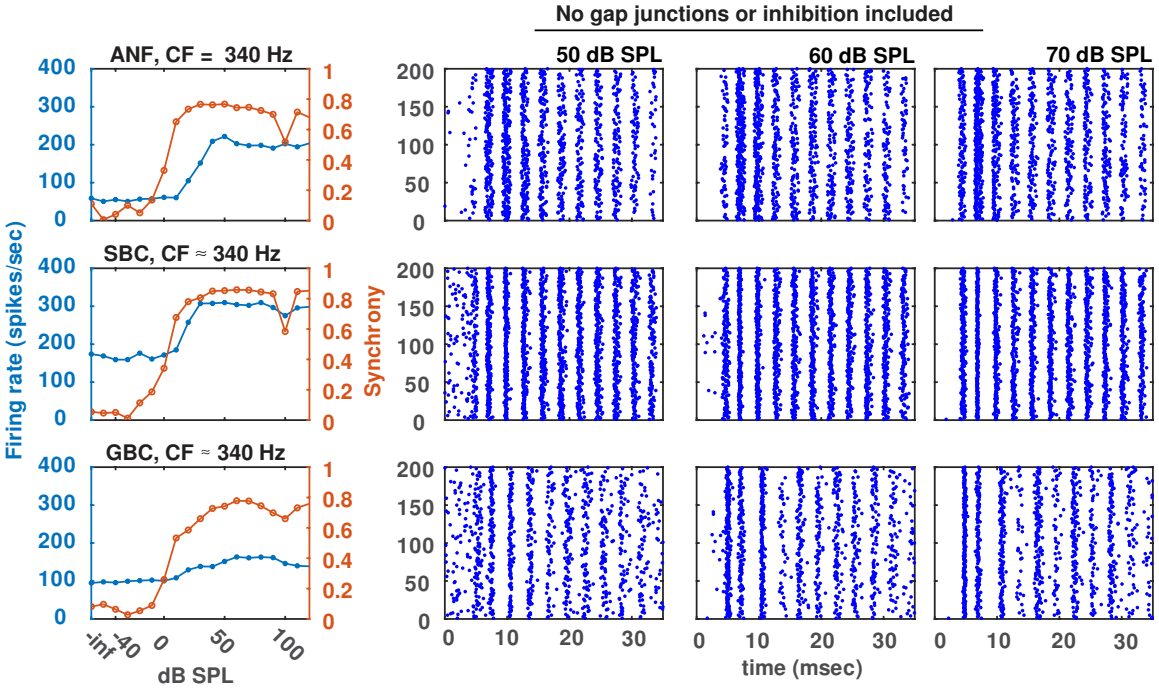

Figure 3.6: Raster plots, firing rate versus level, and synchronization index (SI) versus level for a simulated ANF with a CF of 340 Hz (upper row), a single SBC (middle row) and a single GBC (bottom row) with CFs close to 340 Hz. In these simulations, SBC and GBCs are not connected to any other SBC or GBC via gap junctions. The panels in the left-most column show the discharge rate versus level as blue curves and SI versus level as orange curves. SI values range between 0 and 1, where 0 means there is no synchrony and 1 means perfect synchrony. The −Inf SPL indicates the spontaneous firing rate of the ANF, SBC and GBC. In the raster plot panels, each blue dot represents a spike in a specific time bin over the 200 stimulus repetitions.

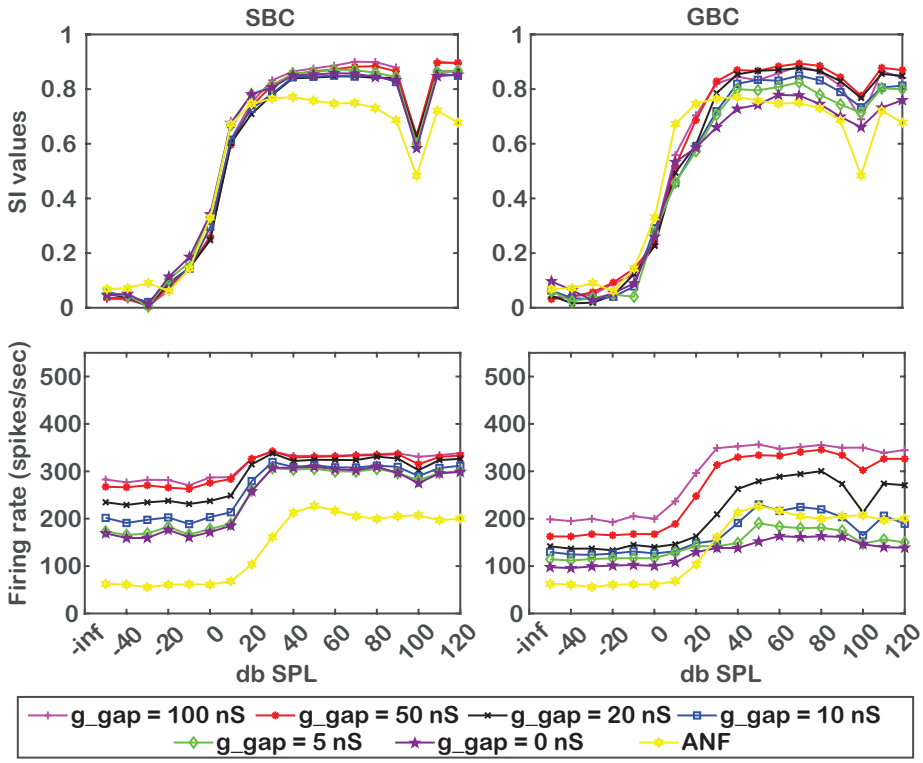

Figure 3.7: Gap junction's effect on synchronization index values (top row) and firing rate (bottom row) for SBC (left column) and GBC (right column) models. In these simulations, no inhibitory connections are included. All 5 fully connected cells in the clusters receive a 340 Hz stimulus. The curves shown in this figure are from the central cell in the cluster that has a CF of 340 Hz, while the other cells in the cluster have CFs slightly higher or lower than 340 Hz.

of the EPSCs of the SBC model (Supplementary Information, Fig. B.3), inhibition's strength on a population of SBC and GBC models (Fig. B.4) and the strength of excitation (Fig. B.5) were inspected to see their effect on this behavior.

3.4.3 Inhibition's effect on synchronization is non-monotonic for both SBCs and GBCs

Fig. 3.9 shows inhibition's effect on the synchronization index values and firing rate of SBCs and GBCs that were not connected to any other bushy cells via gap junctions. The effects of inhibition on the SI values were not as clear as the gap junction's effects. Strong inhibition allowed SBCs and GBCs to reach high SI values, but when the firing rates were inspected, it can be seen that these high SI scores were reached because of the low number of spikes per bin in the period histogram.

As shown in the previous subsection, gap junctions tended to increase the firing rate of model SBCs and GBCs, so it was likely that gap junctions and inhibition caused an interaction on the firing rate and synchrony of model bushy cells. Figure 3.10 shows the effects of a range of strengths of gap junctions and inhibition on the SI values and firing rate of model SBC and GBC clusters, each with CFs close to 340 Hz. Clusters of 5 fully connected bushy cells were simulated, all cells in the cluster received 340-Hz input with $k_{exct} = 3$ for SBCs and $k_{exct} = 0.7$ for GBCs. The color map plots were created by taking the mean of SI values and firing rates across 40 to 80 dB SPL, where they were fairly constant. The plots indicate that high SI values can be achieved with large g_gap and g_inh values (top left and bottom right parts of the SI values plot) for SBCs, but the high SI values for large g_inh are a result of having a low number of spikes per bin in the period histogram. Additionally, high SI values achieved in high g_gap regions might not be achievable because such g_gap values may not be physiologically realistic. For GBCs, high SI values could be obtained by high g_gap and g_inh values (top right of the SI values plot) but at the expense of having unreasonably low firing rates. Therefore g_gap and g_inh values must be carefully chosen to obtain high SI values without having physiologically unrealistic low firing rates.

3.4.4 Parameter set chosen to yield best results

A 3-parameter (g_gap, g_inh, and k_exct) grid search was performed to choose the best parameter set that exhibited low-frequency synchrony enhancement while maximizing the mid-frequency SI values, thereby shifting the drop in maximum SI values of mid-frequency range to be more consistent with the physiological data. It was found that for the SBC model, a g_gap value of 20 nS, g_inh value of 15 nS, and a multiplier k_exct of 4 resulted in the cutoff frequency closest to what has been reported in physiological

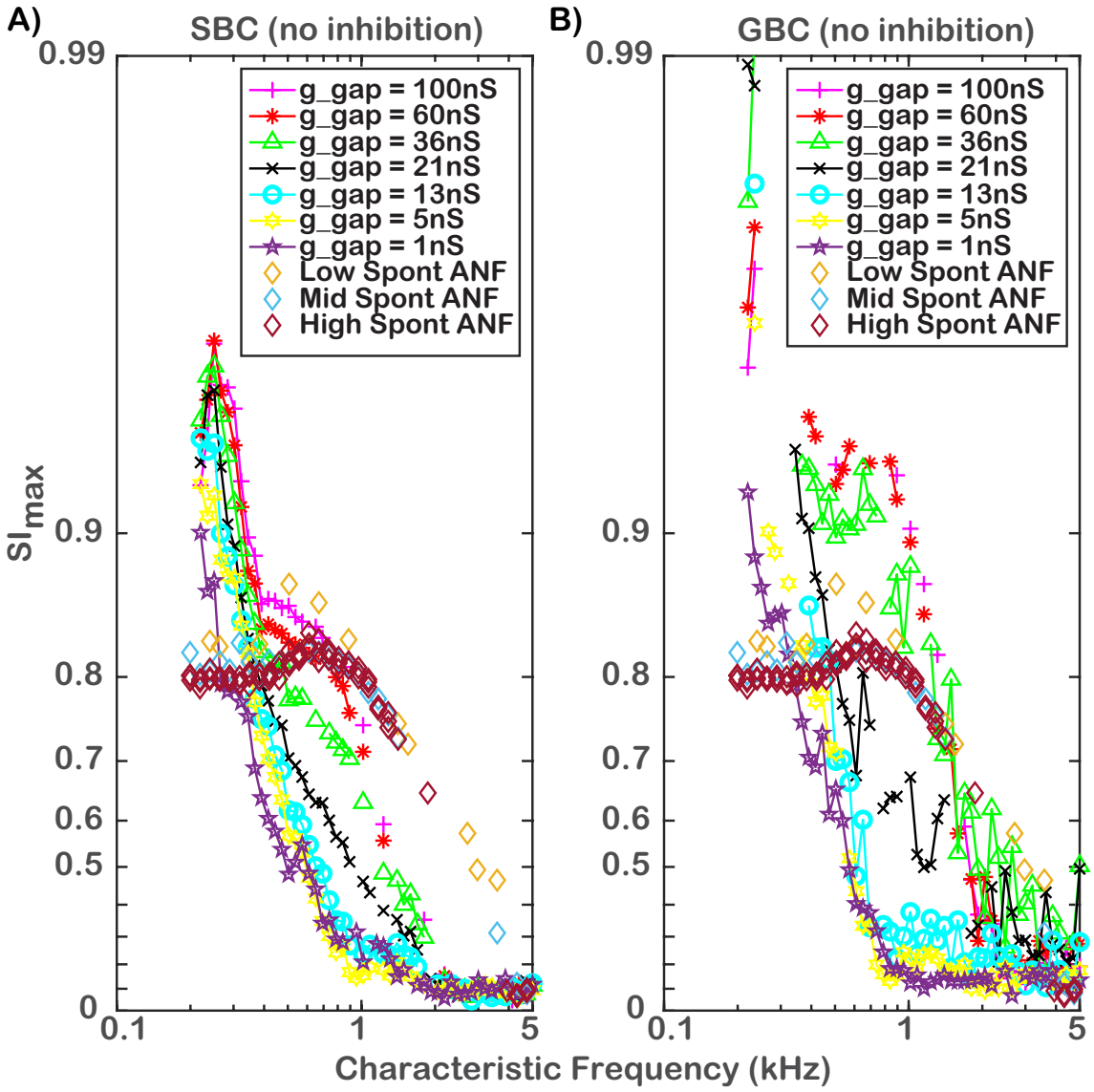

Figure 3.8: Max SI values of population of A) SBCs and B) GBCs with and without gap junctions and ANFs across a range of characteristic frequencies. No inhibition is present in the model for these simulations. The maximum SI values are chosen according to the criteria described in Johnson (1980); Joris *et al.* (1994). Both SBC and GBC models are showing a significant increase in their maximum SI scores as gap junction strength is increased.

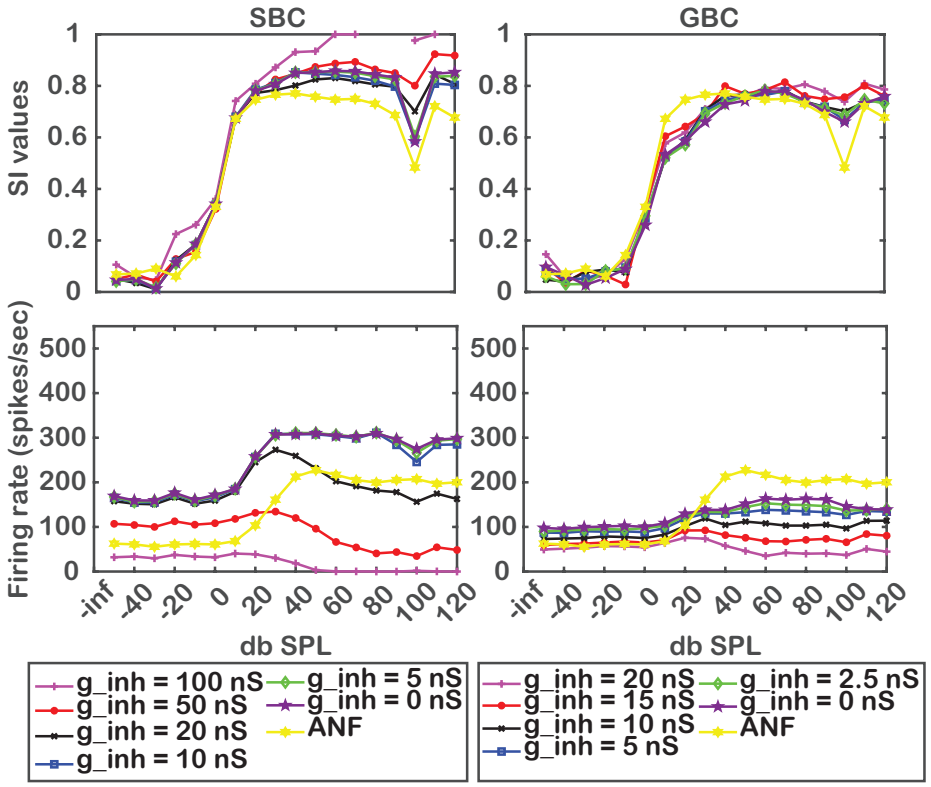

Figure 3.9: Inhibition's effect on synchronization index values (top row) and firing rate (bottom row) of SBC (left column) and GBC (right column) models. In these simulations, the SBC and GBC models do not receive any additional excitation through gap junctions and are stimulated with a 340 Hz sinusoidal input. The CFs of cell models in the cluster are all close to 340 Hz. The curves shown in this figure are from the central cell in the cluster that has a CF of 340 Hz, while the other cells in the cluster have CFs slightly higher or lower than 340 Hz.

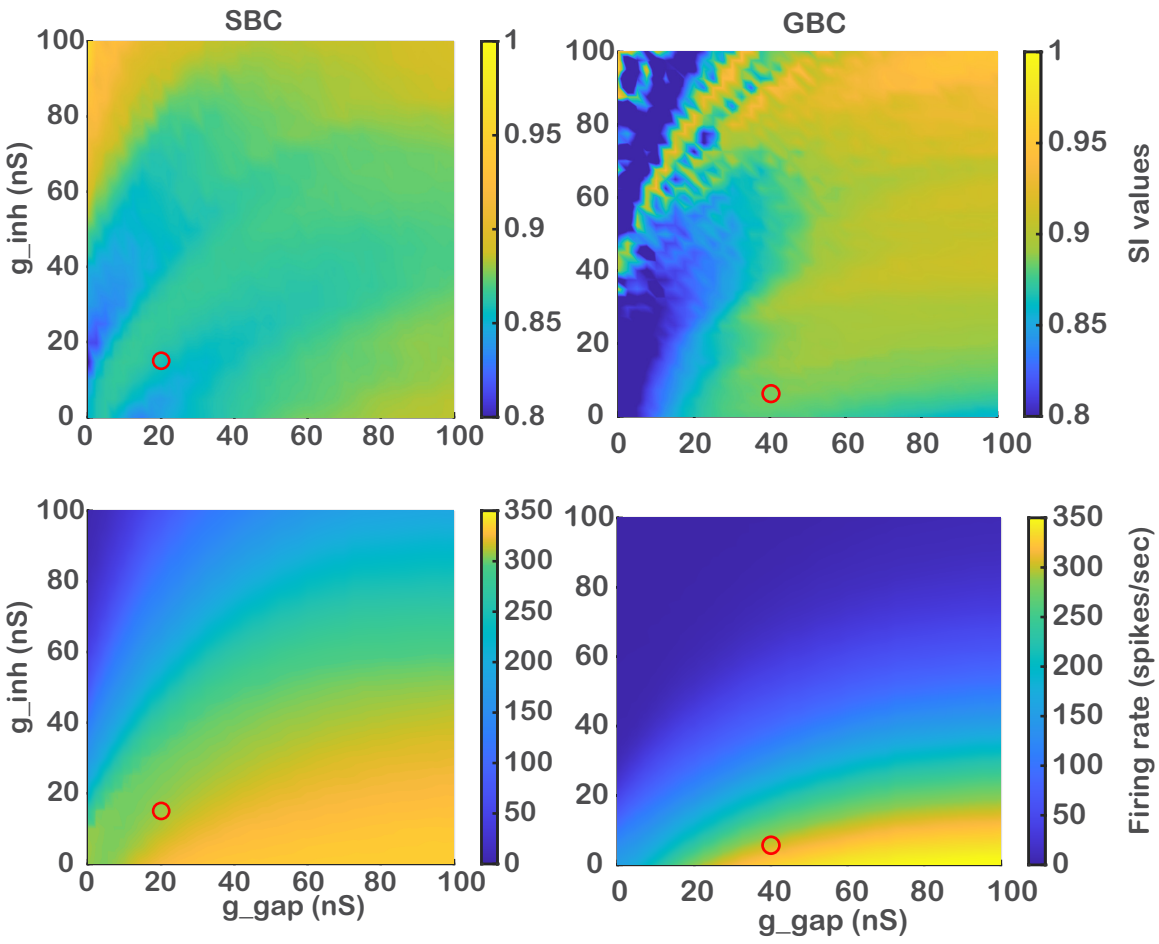

Figure 3.10: Color-map plots of SI values (top row) and firing rates (bottom row) of SBC (left column) and GBC (right column) models with CFs close to 340 Hz. The SBC and GBC models are residing in a fully connected cluster of 5 cells. The red circles indicate the g_gap and g_inh levels chosen as the best parameter set. The values presented in the figure are obtained from the mean of SI and firing rate values when the models are presented with stimulus levels of 40 to 80 dB SPL.

studies, while still maintaining a reasonable firing rate (as seen in Fig. 3.10) without pulling the gap junction strength to potentially unrealistic physiological levels. For the GBC model, g_gap value of 40 nS, g_inh value of 4 nS, and a multiplier k_exct of 0.7 was chosen as the best parameter set. A low level of inhibition was chosen for the 'best' GBC model since the inhibition's effect on the cutoff frequency of the filtering behavior was unstable (Supplementary Information, Fig. B.4) for high inhibition strength values. A reasonable firing rate was achieved for a model GBC with CF of 340 Hz at high g_gap and low g_inh values, as seen in Fig. 3.10. The red circles in Fig. 3.10 indicate the parameter set chosen for g_gap and g_inh for each model cell type. The k_exct values considered as best parameters were the ones that pulled the cutoff frequency of the low pass filter to more physiologically feasible levels (Fig. B.5). Fig. 3.11 shows the raster plots, firing rate versus level, and SI versus level for the bushy cell models with CFs close to 340Hz for their respective 'best parameters'. Fig. 3.12 shows the maximum SI scores of bushy cell models across a range of characteristic frequencies, comparing the results for the 'best parameters' to those for the models without gap junctions or inhibition ('base model').

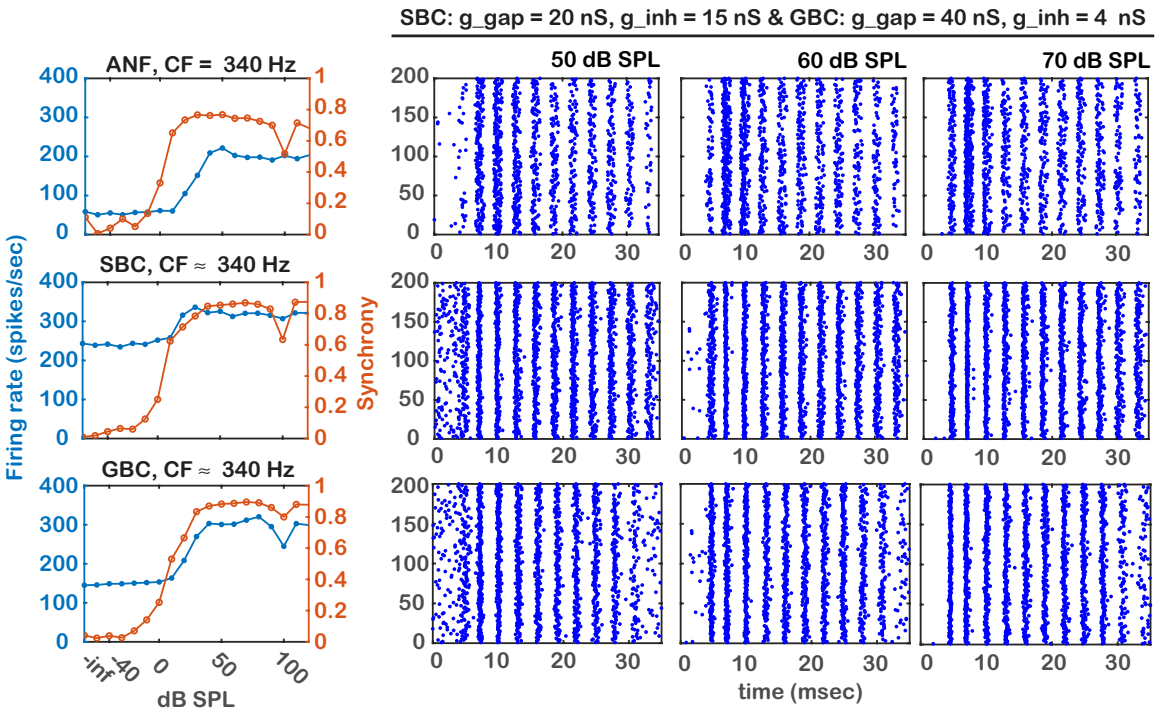

Figure 3.11: Raster plots and firing rate and synchronization index (SI) scores of simulated ANF with a CF of 340 Hz (upper row), a fully connected cluster of 5 SBCs (middle row) and a fully connected cluster of 5 GBCs (bottom row) with CFs close to 340 Hz. The SBC model parameters are g_gap = 20 nS and g_inh = 15 nS with an EPSC multiplier k_exct of 4, and the GBC model parameters are g_gap = 40 nS and g_inh = 4 nS with an EPSC multiplier of 0.7.

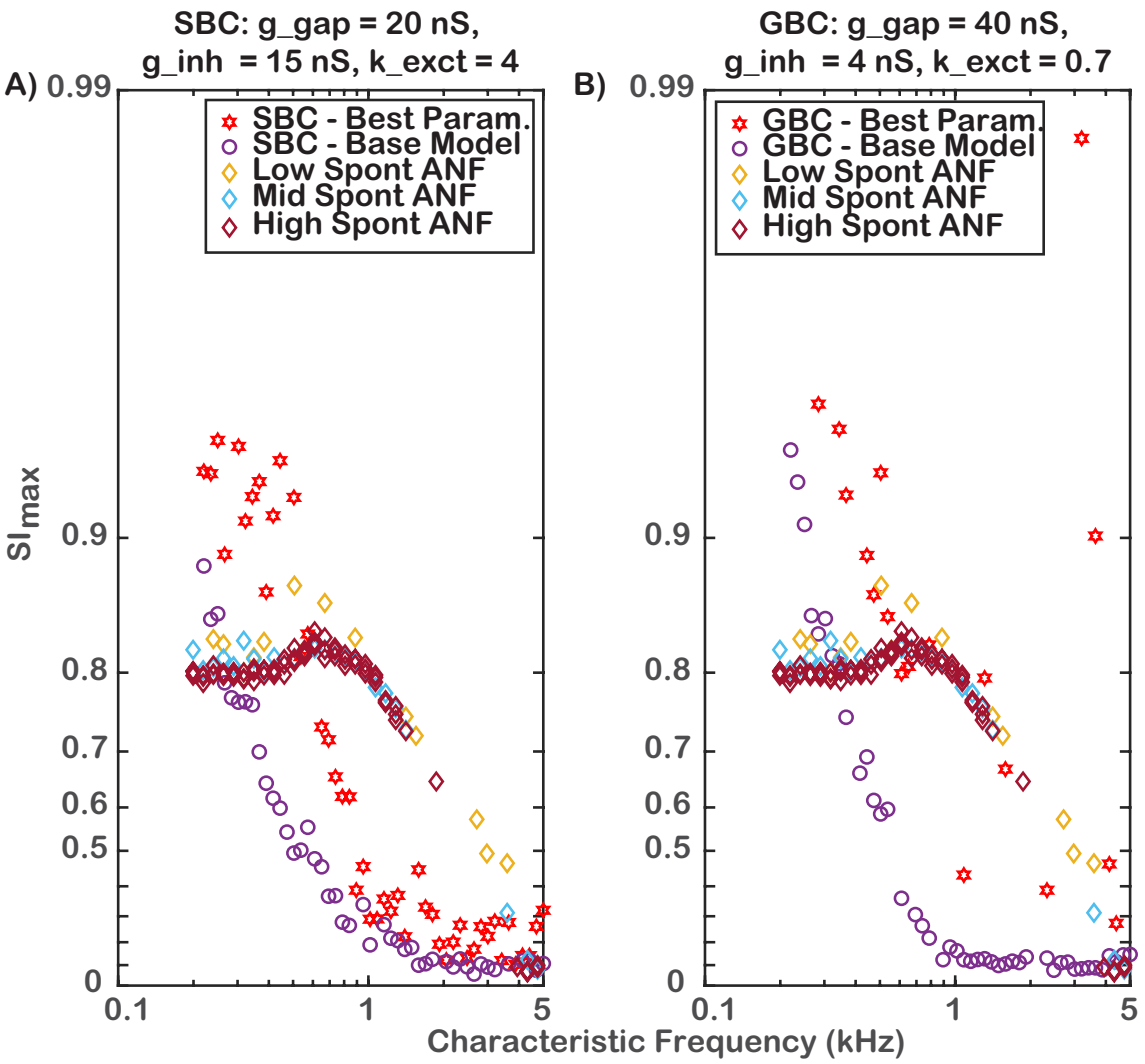

Figure 3.12: Comparison of the max SI values of (left panel) population of SBCs without gap junctions and inhibition, population of a fully connected SBCs with g_gap = 20 nS and g_inh = 15 nS with an EPSC multiplier k_exct of 4, (right panel) population of GBCs without gap junctions and inhibitions, population of a fully connected GBCs with g_gap = 40 nS and g_inh = 4 nS with an EPSC multiplier k_exct of 0.7, and ANFs across a range of characteristic frequencies. The red hexagram data markers indicate the SBC and GBC model with the parameters chosen to make the model's low pass filtering cutoff frequency as close as possible to the physiological recordings. The unusually high SI scores observed around 4 kHz for the GBC model are caused by the model producing only a few spikes in period histogram bins due to inhibition.

3.5 Discussion & Conclusion

In this study, the synchronization of bushy cells of the ventral CN was evaluated using a biophysically-detailed neural-network model. Previous modeling studies of bushy cells have not incorporated gap junctions. This investigation assesses the feasibility of gap junctions as a mechanism that contributes to synchrony enhancement in SBCs. While the SBC models had some level of enhanced synchrony behavior without gap junctions or inhibitory synaptic input, the results of this study show that both gap junctions and inhibition had profound effects on synchronization. The effect of gap junctions on synchronization has a clear increasing trend for both SBCs and GBCs, while inhibition's effect on the synchronization is nonmonotonic for both models. In fully connected bushy-cell clusters of SBCs and GBCs, gap junctions increased synchronization by allowing excitation to spread between the cells in the cluster. For lower gap-junction levels, the subthreshold inputs coming from the neighboring cells can help each cell reach the spiking threshold earlier than it would without gap junctions. For higher gap-junction levels, the spikes coming from the neighboring cells can act like suprathreshold inputs and allow each cell to spike at times when it would not be able to without the gap junction connection. For SBCs, while this effect was relatively small for the model cell that has a CF close to 340 Hz (Fig. 3.13A), a model SBC with CF close to 700 Hz showed the enhancement effect clearly (Fig. 3.13B). Comparison of the SI values between the base GBC model and 'best' GBC model with CF close to 340 Hz are presented in Fig. 3.13C. The SBC model did not show a synchrony enhancement for low CFs since SI values were already high for low CF SBC models. Meanwhile, including gap junctions and inhibition in the low CF GBC model resulted in synchrony enhancement, because including these connections enabled the model to fire synchronously at each cycle of the periodic stimulus.

Example PSTHs of the GBC and SBC models with CF = 1544 Hz are provided in Supplementary Information Fig. B.6. The SBC model without any inhibition or gap junction connections had a primary-like response (Fig. B.6A). When the model parameters were chosen as g_{gap} = 20 nS, g_{inh} = 15 nS, and k_{exct} = 4, the model exhibited an enhanced onset response with reduced late activity (Fig. B.6B). The GBC model without any gap junctions or inhibition connections showed a primary-like-with-notch response (Fig. B.6C). The GBC model with g_{gap} = 40 nS, g_{inh} = 4 nS and the k_{exct} = 0.7 displayed a strong onset response with a notch followed by reduced late activity (Fig. B.6D).

The enhancement in the SBC and GBC models with low-frequency CFs was successfully simulated with the inclusion of gap junctions and inhibition in the model (Fig. 3.12), while the drop in the mid frequencies, which we denoted as the cutoff frequency of the low-pass filtering behavior, still started at a lower frequency than

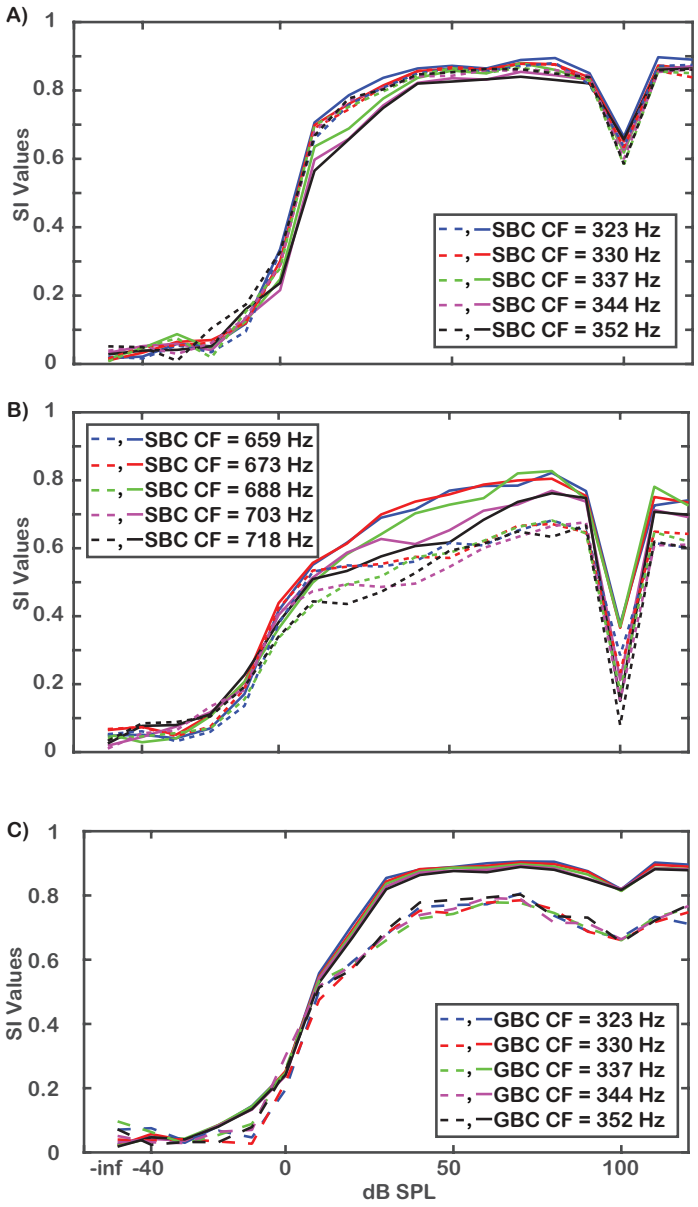

Figure 3.13: Comparison of SI versus sound presentation level curves for cells residing in a fully connected cluster of SBCs with CFs around A) 340 Hz and B) 694 Hz, with sinusoidal inputs matching those two frequencies, respectively. Dashed lines show the model results without any gap junctions and inhibition while solid lines show the model results with g_gap = 20 nS and g_inh = 15 nS and $k_{exct} = 4$ (the parameters chosen for our 'best model'). C) Comparison of SI values of cells residing in a fully connected cluster of GBCs with CFs around 340 Hz. All cells in the cluster receive 340 Hz sinusoidal input. Dashed lines show the model results without any gap junctions and inhibition while solid lines show the model results with g_gap = 40 nS and g_inh = 4 nS and $k_{exct} = 0.7$ (the parameters chosen for our 'best model').

what is observed in physiological studies (Fig. 3.2). The effects of SBC model parameters on fitting the model's cutoff frequency to physiological levels were inspected and gap junction strength, the membrane capacitance, the strength of excitation and inhibition had profound effects, while the decay time of EPSCs had little effect (Supplementary Information Fig. B.3). For GBCs, the strength of excitation and gap junctions had profound effects on pulling the cutoff frequency higher, but the effects of internal model parameters remain to be investigated. To reach the higher cutoff frequency for synchrony enhancement observed in physiological recordings, other mechanisms not investigated in this study may be necessary, such as dendritic inputs (as proposed in Koert and Kuenzel (2021)), a more detailed synaptic model (Xie and Manis, 2013b; Manis and Campagnola, 2018), EPSC/IPSC amplitude variability and a range of ANFs having different SRs rather than only high SR ANF inputs (Spirou *et al.*, 2023). Subtypes of endbulbs of held converging on bushy cells (Wang *et al.*, 2021) suggest that bushy cells receive inputs from ANFs with different spontaneous rates and Spirou *et al.* (2005) indicates that the GBC populations are not uniform and vary in the number of excitatory and inhibitory inputs they receive.

Parameters such as the amplitude of EPSCs, inhibition and gap junctions played a crucial role on synchronization behavior of the bushy-cell models. The parameter space was explored via a grid search to identify sets of best parameters for the SBC and GBC models. When choosing the best parameter sets, the cutoff frequency of the low frequency filtering behavior, spontaneous firing, and maximum SI scores achieved by SBCs and GBCs were considered. Although inhibition had a prominent effect on synchronization, its effect was not as clear as that of gap junctions, since it was non-monotonic as a function of inhibition strength. Inhibition increased the SI scores by suppressing the generation of spikes between the peaks of synchronized firing, hence narrowing the spread of spike times for each period of the stimulus. But this increase in the model's SI corresponded to a decreased firing rate that was lower than that observed in physiological recordings. The inhibition's effect had similar trends for SBCs and GBCs, although the mechanisms of spike production in both models differed. For model GBCs that received many subthreshold inputs, even though the inhibition might suppress some of the subthreshold EPSPs, the model still fired if many subthreshold EPSPs occured in the same time window. Therefore, for low g_inh values, the model continued firing synchronously, even though some subthreshold inputs were suppressed by the inhibition, as shown in Fig. 3.9, as the synchronization index traces for GBC were close to each other for low g_inh values. As the inhibitory strength increased, inhibition started suppressing most of the subthreshold inputs, such that the model's firing rate dropped drastically, and the high SI values were caused by this effect (Fig. 3.10). For SBCs, low levels of inhibition did not have a profound effect on the firing rate or synchronization (Fig. 3.9), because the excitation the SBC models received from ANFs was suprathreshold

and any inhibition that was not enough to disrupt the spike production would not effect the spiking dynamics of the models drastically. As the inhibition got stronger, the firing rate of the SBC model decreased and the rate-level curve flattened. High SI values at high inhibition levels were not caused by highly synchronized spiking behavior, instead it was caused by simply having few spikes in each time bin.

Rothman and Young (1996) investigated the effects of subthreshold/suprathreshold inputs on model GBC's synchronization behavior and found that their model had lower synchronization in the 1–5 kHz region when the model received all subthreshold inputs. A mixed input GBC model which received both subthreshold and suprathreshold inputs exhibited increased synchronization behavior in the 1–5 kHz region. Our model results are in line with this study, since all of our GBC model inputs were subthreshold and the mid-frequency synchrony values were lower than what is reported in Joris *et al.* (1994), without gap junctions in our model. We were able to increase the 1–5 kHz synchronization by introducing high levels of gap junctions or increasing the strength of excitation to almost threshold level. Future investigations with our model could consider a mix of subthreshold and suprathreholds inputs to GBCs in addition to gap junctions. In Rudnicki and Hemmert (2017), the number of ANF inputs converging on GBC models had little effect on the synchronization of the model. Unlike the findings of that model, our simulations indicated that the number of ANF inputs had a strong effect on the synchronization of the GBC model. The initial results presented in Supplementary Information Fig. B.7 indicates that the combined effects of the number of ANF inputs and the strength of gap junction has a profound effect on the synchronization and needs further exploration. The GBC model presented in Ashida *et al.* (2019) indicates the amount of excitation has the biggest effect on the synchrony. We explored the effect of the excitation on the synchrony by changing the k_exct and found that the excitation did indeed have a big effect on the synchrony. Apart from EPSC size, we considered the spread of excitation via gap junctions as an overall excitation the bushy cell models received, and we found that this also had a substantial effect on the synchronization behavior of the model. Ashida *et al.* (2019) also investigates the effect of the model's refractory period on the regularity of the spiking, finding that a long refractory period causes the coincidence detection model to spike regularly. Therefore, while the synaptic inputs arriving within a short time window were important to produce a spike for models with a built-in coincidence-detection mechanism, refractoriness may prevent spiking even when the inputs from ANFs are coincident. In contrast to GBC models with an explicit coincidence-detection mechanism, our model is a modified Hodgkin–Huxley type model based on an SBC model by changing the number of inputs to 12 and making them subthreshold by multiplying with a k_exct $= 0.7$. Thus, our model is not specifically designed to implement a coincidence detection mechanism, but coincidence detection can occur as a result of the dynamics of the membrane potential

and ion channel gating particles. For the GBC model without gap junctions or inhibition, Fig. 3.6 shows that coincidence detection did occur and enhance synchrony on some cycles of a periodic stimulus, but synchrony was not enhanced in all cycles and can even be weakened relative to ANF synchrony. We conducted a preliminary investigation of the membrane and gating-particle dynamics for the GBC model simulations shown in this figure to understand why the synchronization enhancement seen in our GBC model did not match that of simpler coincidence-detection models that do not include adaptation effects. When the dynamics of the low-threshold potassium ion channel I_{LT} are observed, the channel's activation particle w seems to limit the model's ability to spike if too many synaptic inputs come directly after a spike and keep this potassium-channel conductance high (Supplementary Information, Fig. B.8). No matter how many synaptic inputs came from ANFs, the model was not going to initiate another spike until the w particle returned back to the level where the model was able to fire a spike again. When gap junctions were added to the GBC model, the spikes from GBCs within a cluster spread excitation through the gap junctions that overcame the effects of the low-threshold potassium channel, hence allowing the model to show consistent enhanced synchronization behavior (Fig. 3.11). The EPSC decay time constant and other intrinsic GBC model dynamics beyond the I_{LT} current may also have some impact on the effective coincidence-detection behavior of the model and warrant future investigation.

The findings obtained from including inhibitory inputs in our bushy cell models were in line with what is hypothesized in Keine *et al.* (2017). Although including the inhibition helped the bushy cells fire with more temporal precision, it also flattened the model rate-level curves, which reduced the dynamic range in the neural representation of the sound stimuli in the model bushy cells (Keine *et al.*, 2016). As proposed in Kuenzel *et al.* (2015), including both inhibition and large EPSCs tended to increase SI values in our model, and we found that the addition of gap junctions further increased the SI values. Rothman and Young (1996) found that the high SI values could be obtained by their SBC model by receiving a mixture of suprathreshold and subthreshold ANF inputs. Our SBC model reached high SI values by the implementation of gap junctions and inhibition without a need to include subthreshold inputs.

While choosing the best parameter sets for the GBC and SBC models (Figs. 3.10, 3.11 and 3.12), we focused on capturing the synchronization enhancement behavior while keeping the firing rate of the models in a physiologically feasible range. The parameter sets were hand picked by observing the trends in the synchronization and firing-rate with respect to a range of g_gap, g_inh and k_exct levels. Future research could explore finding the best parameter sets using multiobjective optimization algorithms with a cost function that considers the low - mid - high frequency synchronization enhancement and spontaneous and driven firing rates of the bushy-cell

models.

The range of gap junction strength of 0 to 100 nS was chosen empirically to cover a range of effects observed in initial simulations. At the lower end of this range, the gap junctions tended to increase both firing and synchrony, whereas at the higher end of the range, excitation tended to be suppressed. This suppression effect was due to the resting membrane resistance becoming too small for the membrane to reach the threshold for action-potential generation. In the middle range of values, there is partial suppression such that the threshold current increases (relative to no gap junctions), so we scaled the EPSC amplitudes for each gap junction level to compensate (see Fig. 3.5). The existence of gap junctions in VCN is presented in several studies (Gómez-Nieto and Rubio, 2009, 2011; Rubio and Nagy, 2015), yet the conductance values of the gap junction connections between bushy cells are not directly measured. Apostolides and Trussell (2013) presents example gap-junction connections between fusiform and superficial stellate cells of DCN, reporting gap junction conductance values of 0.41 ± 0.04 (std) nS (fusiform to stellate) and 0.98 ± 0.11 (std) nS (stellate to fusiform). However, these were dendro-dendritic gap junctions, and it is reasonable to assume that the gap junction strength is higher in bushy cells because some of the connections are soma-somatic. Curti *et al.* (2012) report that soma-somatic junctional conductance in neurons of the mesencephalic trigeminal nucleus are in the range 2.8 ± 2.0 (std) nS or 7.3 ± 5.0 (std) nS, depending on the estimation methodology. The effective soma-somatic gap-junction strength between cardiac cells reported in Jongsma and Wilders (2000) is 3000 to 12000 nS, which are orders of magnitudes stronger than the connections between the neurons located in the brain and brainstem. Thus, values of g_gap up to 100 nS could be a reasonable estimate for bushy cells, since it falls between the pS level gap junction strengths reported in the other parts of the brainstem and µS levels reported in cardiac cells. Our "best model" gap junction values are just above the upper range of values for the mesencephalic trigeminal nucleus cells, indicating that they could be physiologically realistic.

Gómez-Nieto and Rubio (2011) show in a 3D reconstruction of a cluster of bushy cells that there are a mixture of dendo-dendritic and soma-somatic connections. Although the typical cluster size reported in the paper is 5-6 cells, the exact number of dendo-dendritic and soma-somatic connections made between the bushy cells is unclear. For this study, we assumed all connections made between the bushy cells in the cluster were soma-somatic. Cluster structures which consisted of a mixture of soma-somatic and dendo-dendritic connections could be explored in future research.

Another model behavior that warrants further investigation is the spontaneous discharge rate. Smith *et al.* (1993) and Joris *et al.* (1994) found that SBC with low CFs could have a spontaneous rate above 150 spikes/sec, but higher-CF bushy cells had lower spontaneous rates. The overall spontaneous rates observed in our model

of SBCs and GBCs were higher than what is reported in these physiological studies, since the SBC model received suprathreshold inputs from 3 high-spontaneous-rate (HSR) ANFs and the GBC model received subthreshold inputs from 12 HSR ANFs. Initial simulations exploring the input combination of 1 medium-spontaneous-rate and 2 HSR ANF inputs did not show promising results in terms of decreasing the spontaneous rate of the SBC model, and the SI scores reached for this setting were lower than what was achieved by having 3 HSR ANF inputs. We also explored different number of inputs to the GBC model. In simulations with 23 ANF inputs having the spontaneous-rate distribution reported in Liberman (1991), the spontaneous rate of the model was decreased to be more within the physiological range, but the driven rate was reduced too much, and SI scores could not reach higher values than ANFs. Hence, for our present GBC model structure, 12 inputs from ANFs appears to be more appropriate. In our model, the evoked inhibition coming from TV and D-Stellate cell models activates at higher stimulus levels, hence it has no effect on the spontaneous rate of the model. Therefore, a different source of inhibition that is spontaneously active must be provided to pull the spontaneous rate of the model to physiologically feasible levels, as proposed by Rothman and Young (1996). The inclusion of local inhibitory inputs such as L-stellate cells might be a solution to this problem (Ngodup *et al.*, 2020). Another solution to reduce the spontaneous rates of the SBC and GBC models could be implementing synaptic desensitization, as presented in Xie and Manis (2013b); Spirou *et al.* (2023).

Including the inhibitory and gap junction connections at the same time in the model not only allowed inspecting of the individual effects of each mechanism, but also allowed us to examine the combined effects of both mechanisms on synchronization. Although the model does not yet include some recently-discovered inhibitory input types and the physiological recordings directly made from gap junctions of bushy cells are not currently available for us to confirm if the strength of gap-junction connections implemented in the model was in a biophysically feasible range or not, the model shows promising results in terms of how gap junctions can effect the synchronization and could be a crucial piece of the synchrony enhancement puzzle.

3.6 Acknowledgements and Funding

This research was funded by NSERC Discovery Grants RGPIN-2018-05778 & RGPIN-2024-05888 (ICB) and was enabled in part by support provided by Compute Ontario (`www.computeontario.ca`) and the Digital Research Alliance of Canada (`www.alliancecan.ca`). The authors thank Dr. Laurel H. Carney for the suggestions to investigate gap junction connections in bushy cells and their potential effect on synchronization. No AI tools were used in generating the data, producing the figures, or

writing or editing the manuscript.

3.7 Author Contribution

Conceptualization: ICB. Methodology: MY and ICB. Software: MY and ICB. Validation: MY and ICB. Formal Analysis: MY and ICB. Investigation: MY and ICB. Data Curation: MY. Writing - Original Draft: MY and ICB. Writing - Review & Editing: MY and ICB. Visualization: MY and ICB. Supervision: ICB. Project Administration: ICB. Funding Acquisition: ICB.

3.8 Code and Data Availability

The model code can be found here:
github.com/bushy_cell_network_model_with_gap_junctions. To reproduce the findings, the data can be provided upon request.

3.9 Declarations

3.9.1 Conflict of Interest

The authors declare no conflicts of interest, in any form.

Chapter 4

Model Bushy–Cell Neurogram Responses to Broadband Speech Signals

In the previous chapter, the responses of SBC and GBC models to short pure–tone stimuli near the CF of each central cell in the bushy–cell clusters were inspected. The pure-tone responses provided useful information in terms of showing the ability of the models to synchronize and how gap junction affects this behavior, and published data from electrophysiological recordings in animal models are available for comparison and optimization of the model. However, it is also of interest to inspect bushy–cell model responses to more realistic stimuli such as speech to understand the neural processing of sounds in the brainstem. In this chapter, bushy–cell model responses to broadband speech stimuli, to the word "besh" and the sentence "How do we define it?", were investigated.

First, the ANF responses to the speech stimuli is introduced. Then, the responses of the base SBC and GBC models (without gap junctions and inhibition) to the same stimuli is provided and compared with ANF responses. The SBC and GBC models are also constructed with the "best model" parameters chosen in Chapter 3 and their responses to the same stimuli are examined. Neurograms and synchronized rate plots (Young and Sachs, 1979) are used to visualize bushy–cell model responses to the speech stimuli.

4.1 Methods

A population of Bruce *et al.* (2018) type ANF models with CFs from 250 Hz to 16 kHz was simulated to create the fine-timing and mean-rate ANF neurograms (Wirtzfeld *et al.*, 2017). At each CF, 50 ANFs with spontaneous-rate (SR) distribution of 10

low SRs, 10 mid SRs and 30 high SRs were simulated and the outputs obtained from each fiber were pooled to form the population response to the stimulus. To create fine-timing neurograms, a hamming window of 32 samples with a %50 overlap was applied to spike trains. Mean-rate neurograms were created by rebinning the PSTHs over 100 µsec and applying a 128-sample hamming window with a %50 overlap of spike trains.

The SBC and GBC models were constructed as described in Chapter 3. The word "besh" and the sentence "How do we define it?" at 65 dB SPL stimulus level were provided to the bushy-cell models 20 times. A population of bushy cell clusters were simulated, with the central cell in each cluster having a CF ranging from 250 Hz to 15 kHz. Each cluster consisting of 5 fully-connected bushy cells, and the results presented in this chapter were the combined responses of all cells in each cluster. Because the response at each CF of the bushy cell neurograms was the summed activity of only 5 bushy cells compared to 50 fibers in the ANF neurograms, and the bushy cells typically have lower firing rates than the ANFs. The bushy cell model responses were pooled across 20 repetitions of the stimulus, to obtain spike counts with approximately the same order of magnitude for the ANF and bushy-cell neurograms. Base SBC and GBC models do not have any gap junctions or inhibitory inputs while the models referred as "best SBC & GBC models" have g_gap = 20 nS, g_inh = 15 nS and k_exct = 4 for SBCs and g_gap = 40 nS, g_inh = 4 nS and k_exct = 0.7 for GBCs.

Synchronized rate $R(f)$ plots were created by taking the Fourier transform of the PSTHs of ANF, SBC and GBC responses over a windowed segment of voiced speech (Young and Sachs, 1979). These plots provide a visual representation of how strongly the ANFs, SBCs and GBCs responded to the harmonics of voiced speech segments of the stimuli. To compare the peaks in the frequency domain better, the pooled ANF PSTH response was divided by 50 (the number of fibers per each CF), while the pooled bushy cell PSTH response was divided by 100 (20 repetitions $\times$ 5 cells in the cluster) when the synchronized rate plots were created.

4.2 Results

Figure 4.1 provides the spectrogram of the word "besh" at 65 dB SPL, and fine-timing and mean-rate ANF neurogram responses to the stimulus. The vowel segment of "besh" has a voicing pitch of 100 Hz and formants at 500 Hz, 1.7 kHz, 2.5 kHz. The ANF model synchronizes to different harmonics of the vowel segment of "besh" as a function of the CF, with synchronization to resolved low-frequency harmonics for CFs at and near the voicing pitch (100–300 Hz), synchrony capture to the formant frequencies at CFs near the respective formant frequencies (0.5, 1.7, and 2.5 kHz),

and some synchrony to the voicing pitch (100 Hz) at mid-to-high CFs in between the formant frequencies, consistent with physiological data (Young and Sachs, 1979). Figure 4.2 provides the spectrogram of the sentence "How do we define it?" at 65 dB SPL, and fine-timing and mean-rate ANF neurogram responses to the stimulus. The ANF model responded strongly to acoustic onsets and showed distinctive patterns of synchronization to different harmonics of the voiced segments of the stimuli from low to mid CFs in a similar fashion to the responses to the vowel segment "besh".

Bushy-cell fine-timing neurogram responses are depicted in the same way as ANF neurogram responses. In both Figures 4.3 and 4.4, the spike per bin counts were lower than ANFs because the phasic firing nature of bushy cells means that they tend to fire fewer spikes than ANFs. Figure 4.3 shows the fine-timing SBC and GBC neurograms to the stimulus "besh" for the base model (no gap junctions or inhibition). The low-frequency resolved harmonics of the stimulus were successfully encoded in the firing patterns of the SBC model at low CFs, with the responses to the voicing pitch only at higher CFs, while the GBC model responded only to the voicing pitch across a wide range of CFs. SBC and GBC models with best parameter sets, chosen according to the results presented in Chapter 3, were used to create the neurogram responses to the stimulus "besh" in Figure 4.4. Since inhibition was included in both SBC and GBC best models, the neural representation to the speech stimuli was sparser than base SBC and GBC models. In both models, the responses to the voicing pitch become more pronounced because of the effects of gap junctions and inhibition.

To better understand the SBC and GBC model responses to the harmonics of the vowel segment of the stimulus, synchronized rate plots were created. Figures 4.5 and 4.6 show the harmonic structure of "besh" by taking the Fourier transform of the stimulus between 90 msec to 170 msec (blue curves), and compare the SBC & GBC (red curves for "best model", black curves for base model) and ANF (green curves) responses over the same stimulus window. The responses of SBCs and GBCs with different CFs are presented in these figures. SBC and GBC models with low CFs had a better synchronized response to the first couple of harmonics than the ANF fibers do (Figures 4.5A and 4.6A). Panels C and D in Figures 4.5 and 4.6 show that both SBC and GBC models with high CFs have strong synchronized rates across a range of harmonics. Looking back at the bushy-cell fine-timing neurograms (Figs. 4.3 and 4.4), this response is primarily at the voicing pitch (100 Hz), and the high values of $R(f)$ at the harmonics are due to the peaky shape of the PSTHs for phasic-firing bushy cells and rectification (i.e., spike counts cannot go negative), rather than there being synchrony to the harmonics at those frequencies. These types of harmonic distortions are well documented in previous studies of vowel responses (e.g., Young and Sachs, 1979). For low CFs, the best SBC model shows a small enhancement at the harmonic at 100 Hz compared to the base SBC model. For high CFs, the improvement in the low-frequency harmonics are more pronounced. For best GBC

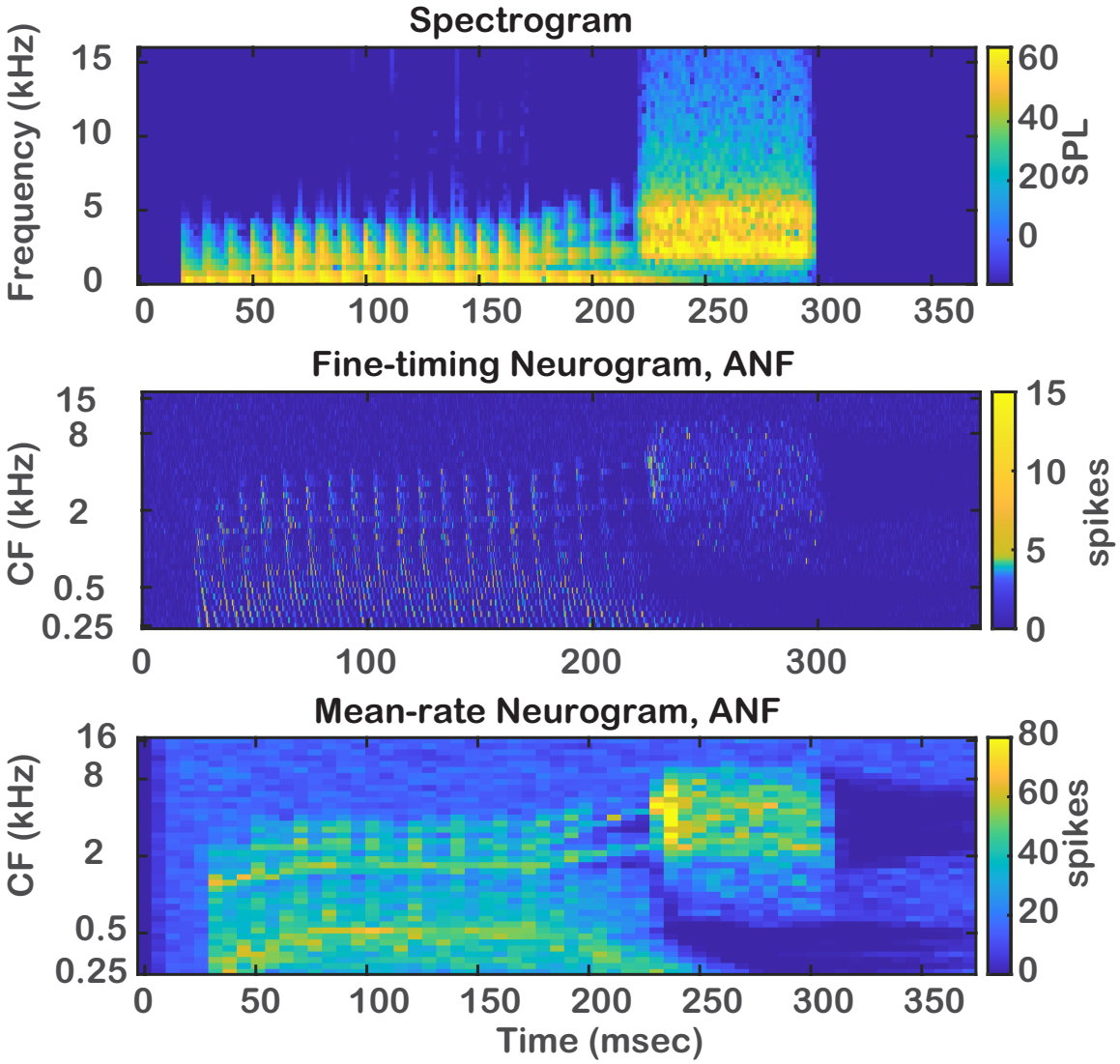

Figure 4.1: Spectrogram, mean-rate and fine-timing ANF neurogram responses to the word "besh" at 65 dB SPL. The color bars on the right show the number of spikes per PSTH bin. The ANF model is able to represent the low-frequency resolved harmonic content of the stimulus in its firing pattern. Notice the scaling and range differences in the spectrogram and neurogram y-axis in the plots.

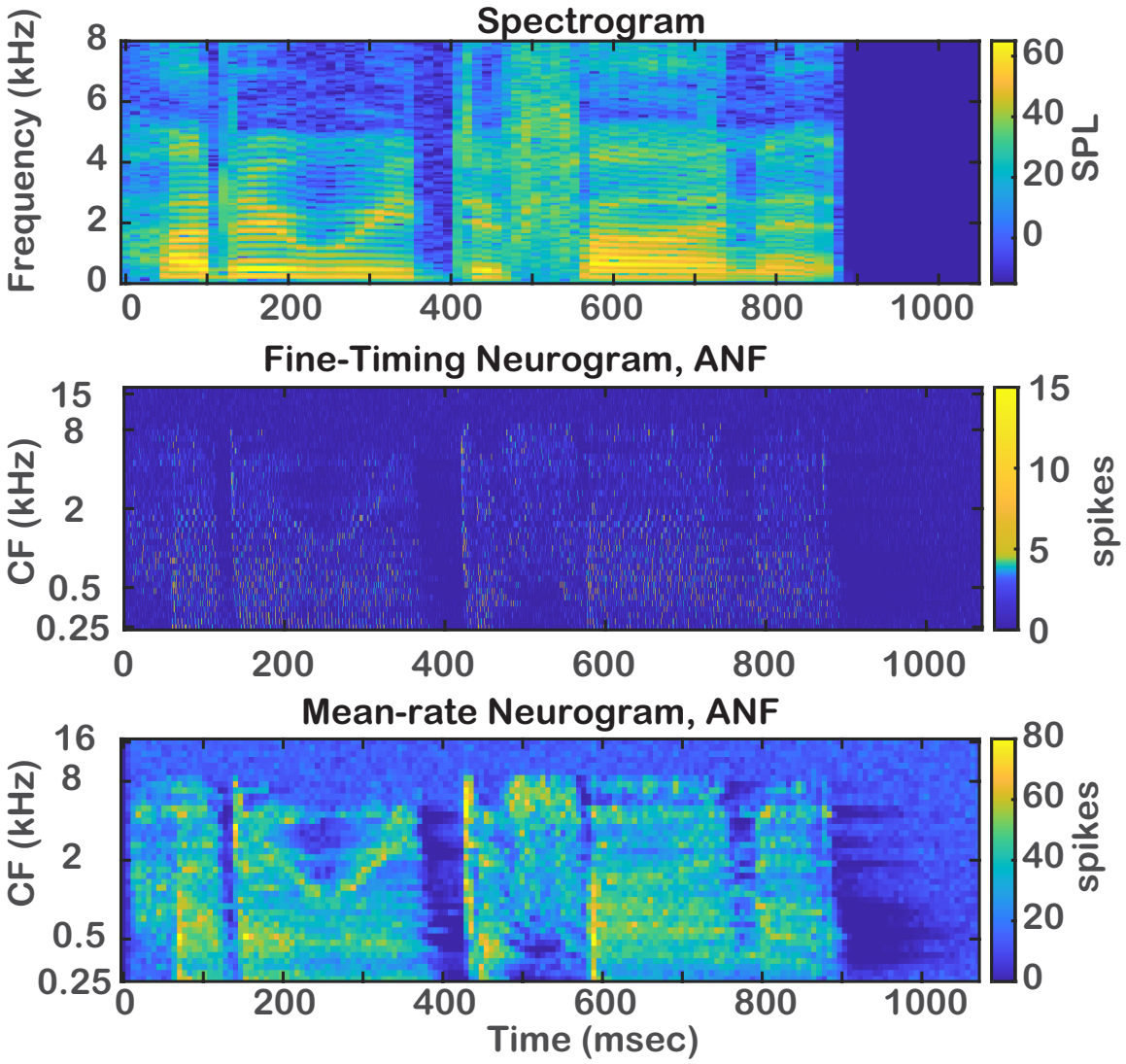

Figure 4.2: Spectrogram, mean-rate and fine-timing ANF neurogram responses to the sentence "How do we define it?" at 65 dB SPL. The color bars on the right show the number of spikes per PSTH bin. Notice the scaling and range differences in y-axis in the spectrogram and neurogram plots.

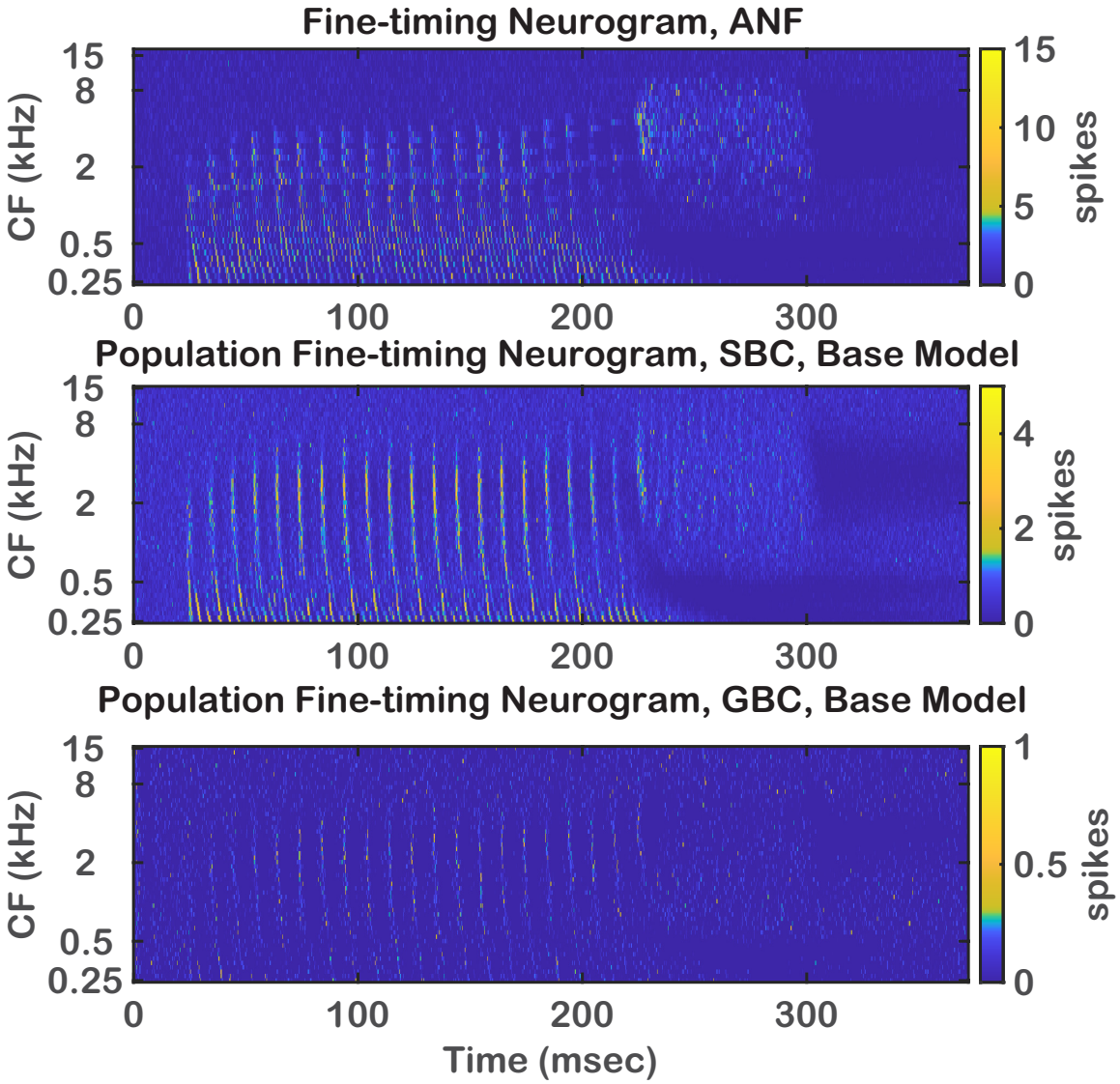

Figure 4.3: Top panel shows the fine-timing ANF neurogram response to the word "besh" at 65 dB SPL. Middle and bottom panels show the base SBC and GBC model responses to the word "besh" respectively. Base SBC model shows a strong response to low-frequency resolved harmonics and voicing pitch content of the stimuli while the base GBC model's response to those frequency components are sparse yet still distinguishable.

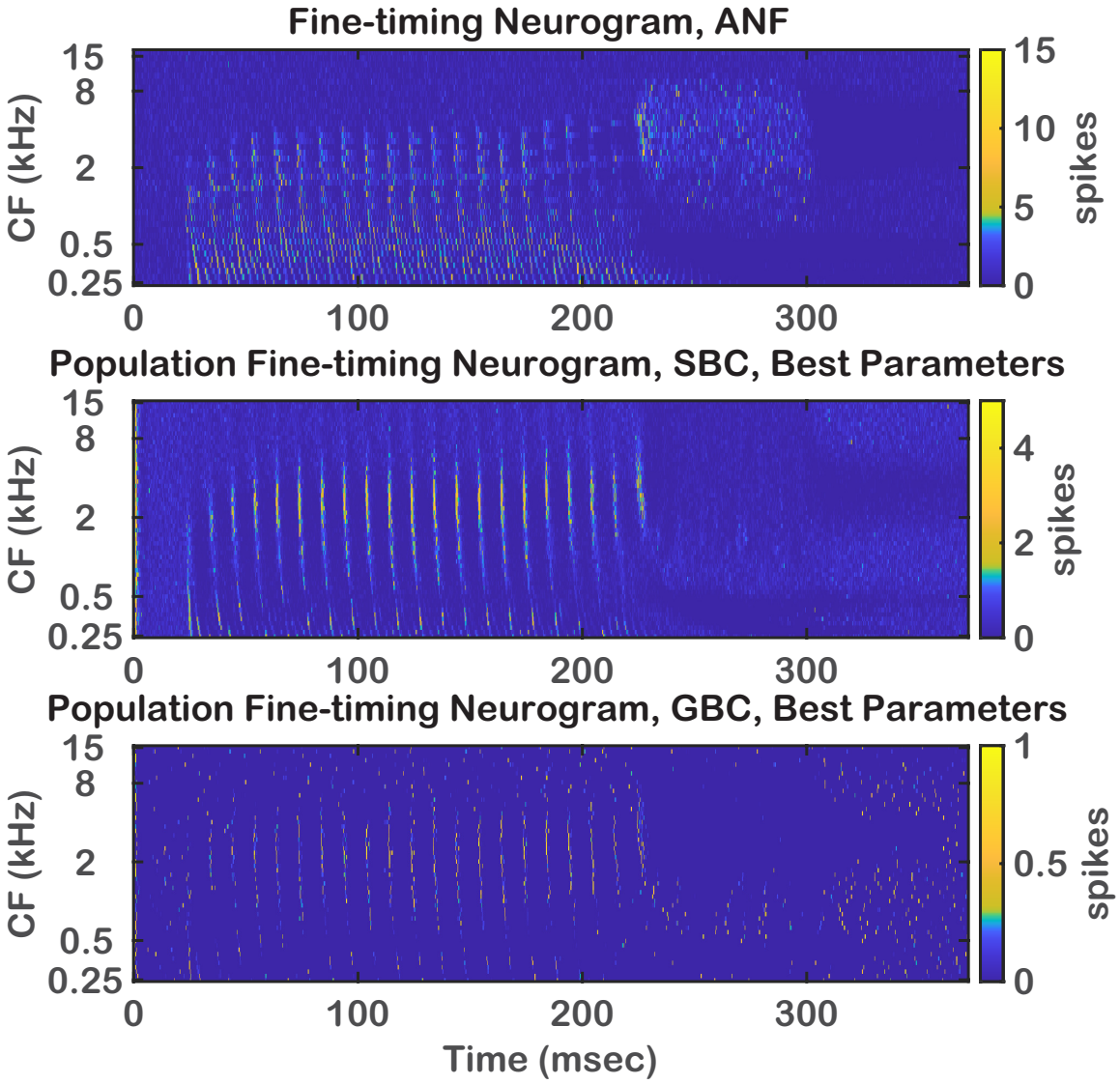

Figure 4.4: Top panel shows the fine-timing ANF neurogram response to the word "besh" at 65 dB SPL. Middle and bottom panels show the best SBC and GBC model responses to the word "besh" respectively. For both SBC and GBC models, the responses to the low-frequency resolved harmonic components of the stimulus weakens because of the inhibition but the responses to the voicing pitch get even more pronounced.

model, the improvement in the low-frequency harmonic responses was consistently improved compared to the base GBC model at high CFs.

Figures 4.7 and 4.8 show the SBC and GBC model mean-rate neurograms. Base SBC model responses to low-frequency components of the stimuli were stronger than the ANFs. The sparsity of the base GBC mean-rate neurogram response is also clear in Fig. 4.7. The best SBC and GBC model mean-rate neurograms show how including the gap junctions and inhibition to the model enhances the responses to the voicing pitch.

Figures 4.9 and 4.10 show the fine-timing neurograms responses of base and best bushy-cell models to the sentence "How do we define it?". These figures indicate that the base SBC models are noticeably responding to the onset of the words and have a strong low-frequency responses. The sparsity of the GBC model response to the stimuli is also clear here. Best SBC model fine-timing neurogram shows a more pronounced onset and low-frequency response (Fig. 4.10, middle panel) while including gap junctions and inhibitions help the GBC model to respond to the onset and low-frequency components more strongly than the base model (Fig. 4.10, bottom panel). These behaviors are more visibly clear in the mean-rate neurograms shown in Figures 4.14 and Fig. 4.15.

The 250 to 350 msec section of the sentence stimulus was used to create the synchronized rate plots to investigate the model responses to a vowel different than what is investigated in "besh". Figure 4.11 shows the sentence stimulus and PSTH responses of ANF and base SBC models used to create the synchronized rate responses.

Figures 4.12 and 4.13 show the synchronized rate plots of SBC and GBC models respectively. For low CFs, both SBC and GBC models respond strongly to the first harmonics of the signal. The base models exhibit a stronger response than ANF, while the "best" models show a weaker response to the same component (Figs. 4.12A and 4.13A). The higher CF SBC and GBC models did not show a significant response to this particular signal section as it can also be seen in the fine-timing and mean-rate neurograms. The responses of GBC models to the same signal segment is similar to the SBC responses.

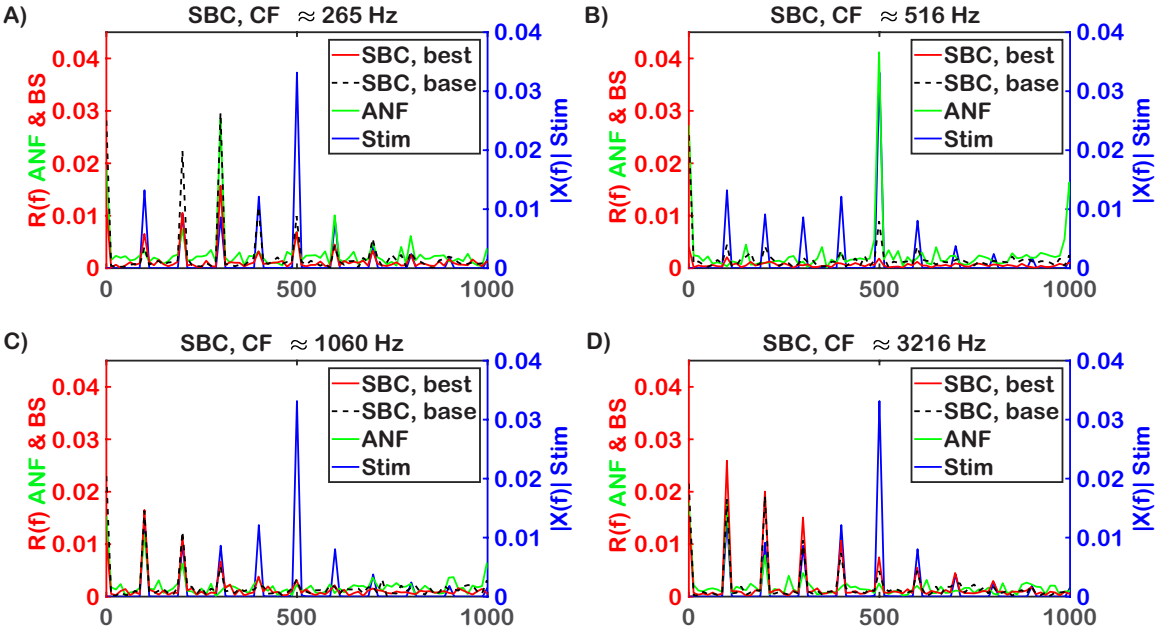

Figure 4.5: Synchronized rate plots of base SBC model in response to 90 msec to 170 msec section of the word "besh" at 65 dB SPL. The CFs of SBCs and ANFs in the panels are as followed; A) SBC with CF = 252 Hz, ANF with CF = 279 Hz. B) SBC with CF = 504 Hz, ANF with CF = 528 Hz. C) SBC with CF = 1008 Hz, ANF with CF = 1113 Hz. D) SBC with CF = 3200 Hz, ANF with CF = 3232 Hz. The base SBC model have stronger responses to the low-frequency components of the stimuli than ANFs. A) Although the responses to harmonic at 100 Hz is improved in the "best model" compared to the base model, the responses to the harmonics at the higher frequencies are weakened. B) The ANF model strongly responds to the formant frequency while the base SBC model shows a weak response at the formant frequency. The "best" SBC model does not respond to any of the harmonic components. C) Both base and "best" SBC models responds to the first few low-frequency resolved harmonic components of the stimuli as strong as ANF does. D) For high CF bushy cells, the responses to the low-frequency resolved harmonics are improved consistently in the "best model" compared to the base model.

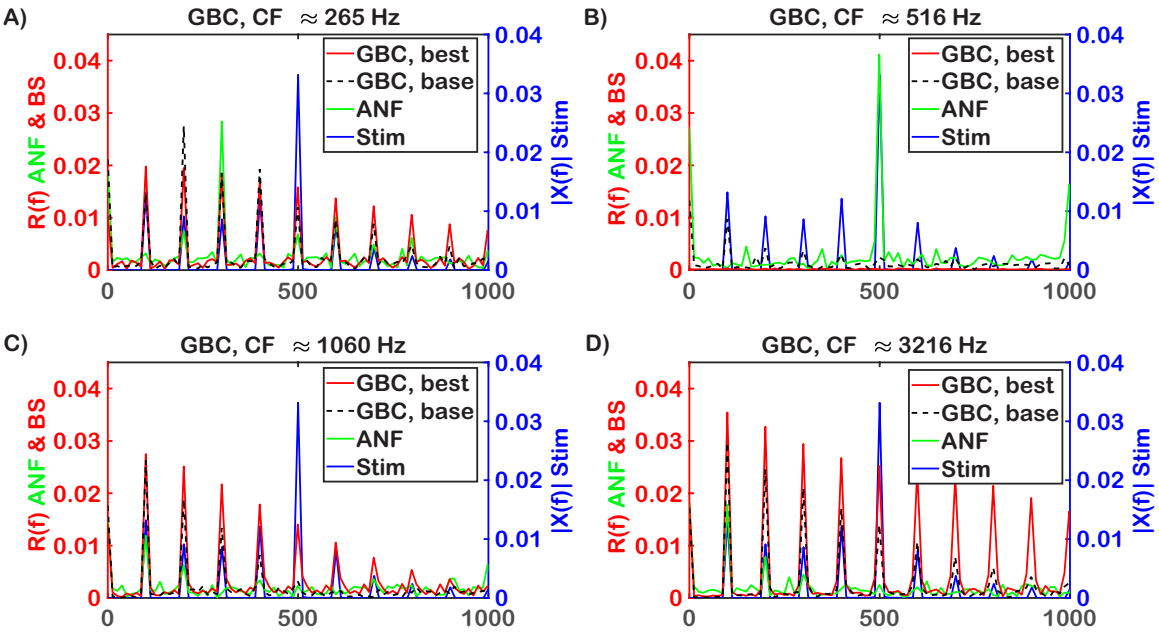

Figure 4.6: Synchronized rate plots of base GBC model in response to 90 msec to 170 msec section of the word "besh" at 65 dB SPL. The CFs of GBCs and ANFs in the panels are as presented in Fig. 4.5. A) The base GBC model has stronger responses to the low-frequency resolved harmonics of the stimuli than ANFs. B) As in SBC model responses, the base GBC model shows a weak response to the first few harmonics, while the "best" GBC model does not respond to any of the components. C & D) The best GBC model shows enhanced responses at low-frequency resolved harmonics compared to the base GBC model at higher CFs.

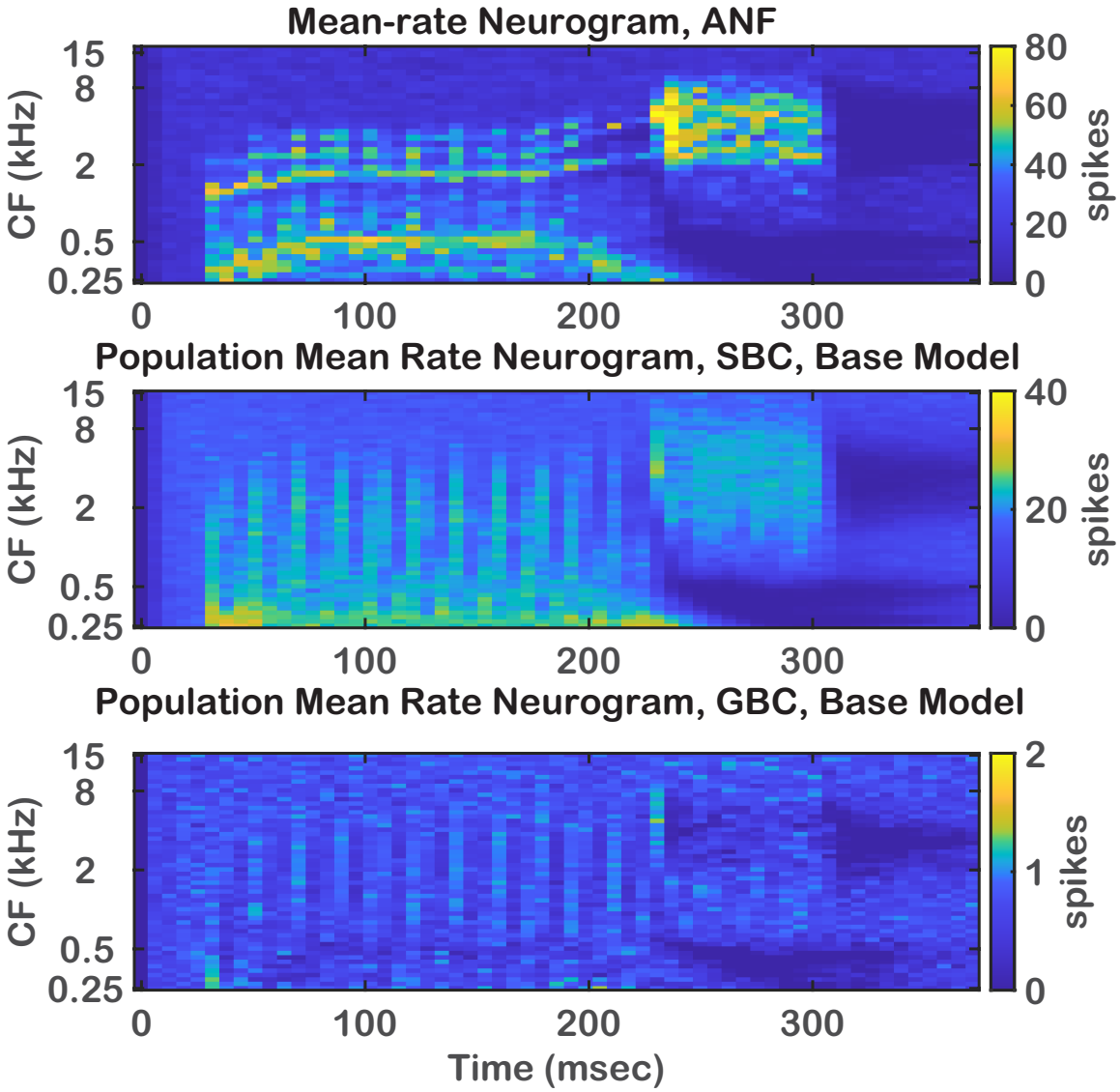

Figure 4.7: Top panel shows the mean-rate ANF neurogram response to the word "besh" at 65 dB SPL. Middle and bottom panels show the base SBC and GBC model neurogram responses to the word "besh" respectively. The strong low-frequency responses and more pronounced voicing pitch response can be seen in SBC model mean-rate neurogram. The GBC mean-rate neurogram on the other hand indicates a more sparse response.

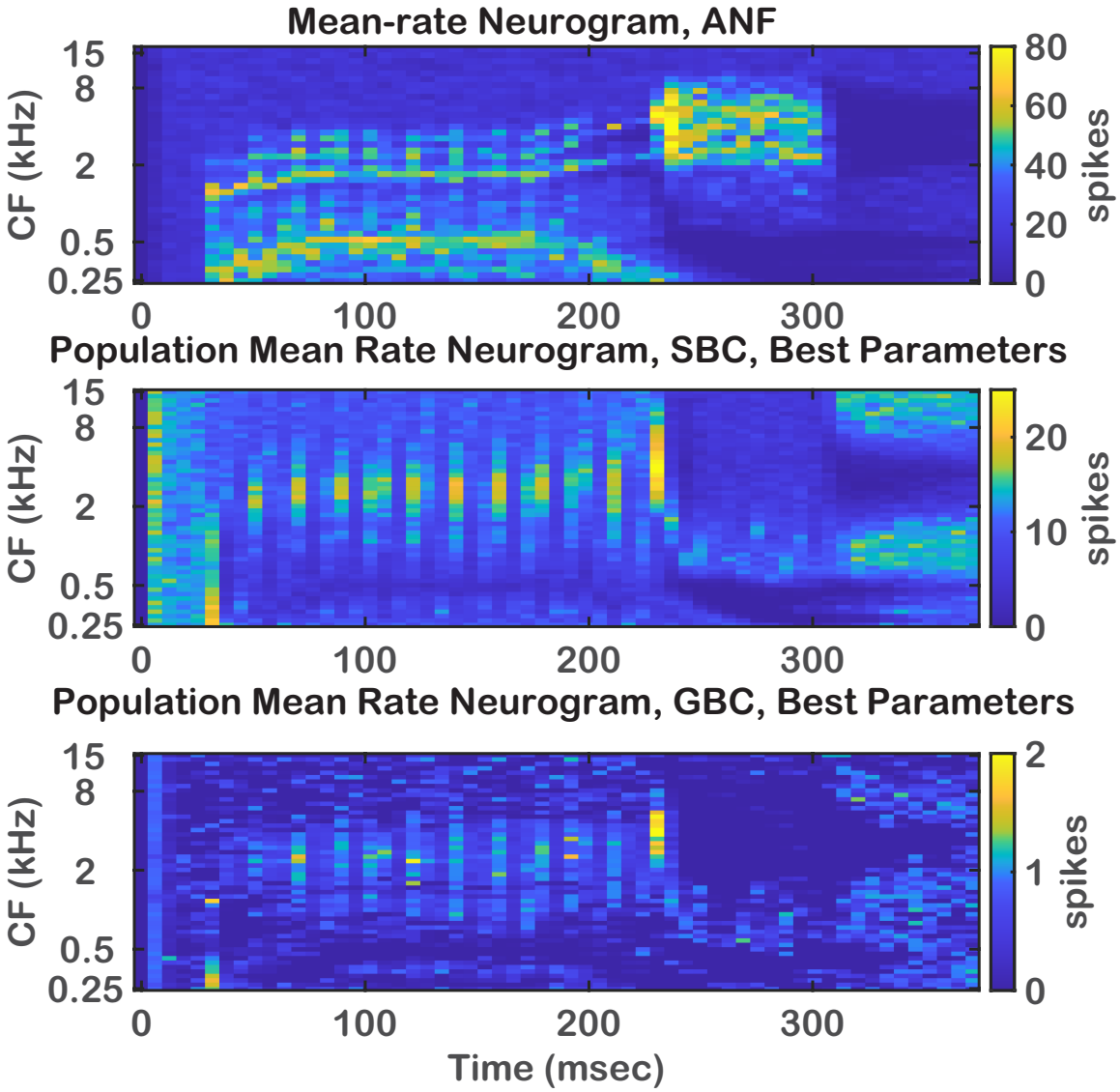

Figure 4.8: Top panel shows the mean-rate ANF neurogram response to the word "besh" at 65 dB SPL. Middle and bottom panels show the best SBC and GBC model neurogram responses to the word "besh" respectively. The effect of inhibition on low-frequency components can be seen clearly, while the effect on gap junctions on the voicing pitch are more pronounced.

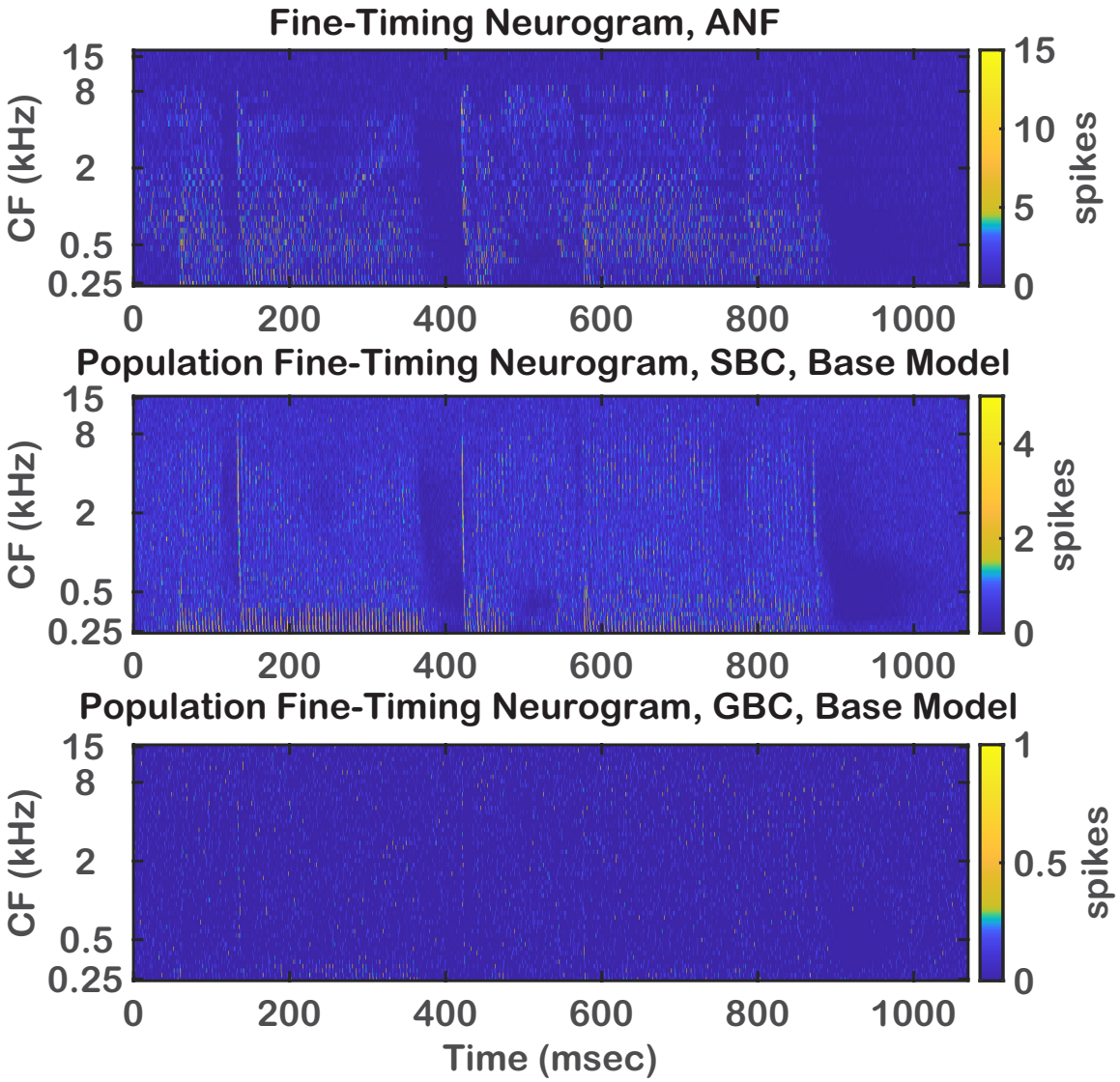

Figure 4.9: Top panel shows the fine-timing ANF neurogram response to the sentence "How do we define it?" at 65 dB SPL. Middle and bottom panels show the base SBC and GBC model responses to same stimulus, respectively. Base SBC model shows a strong response to the onset of the words and low-frequency components. On the other hand, base GBC model only shows weak responses to the low-frequency components.

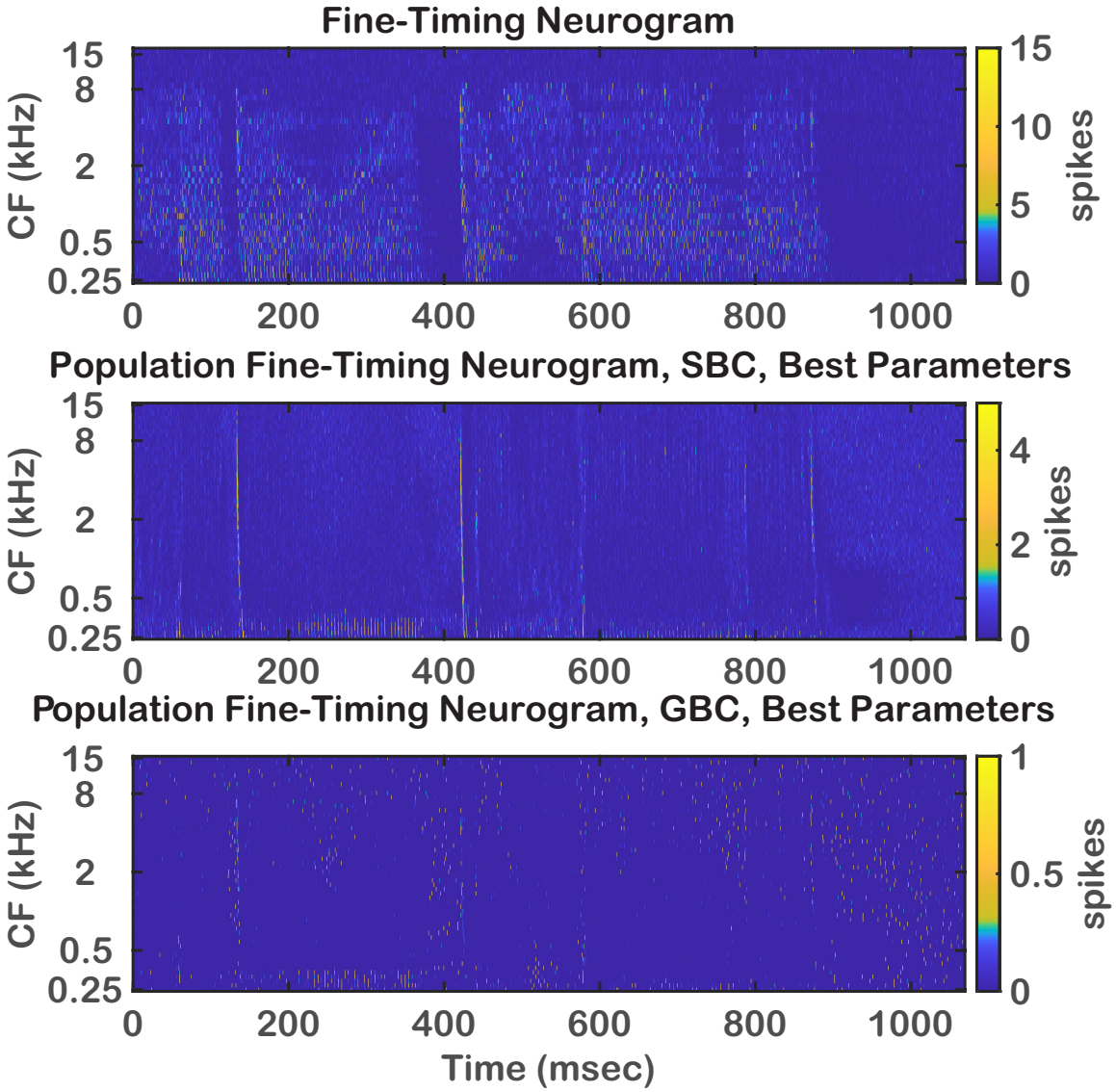

Figure 4.10: Top panel shows the fine-timing ANF neurogram response to the sentence "How do we define it?" at 65 dB SPL. Middle and bottom panels show the best SBC and GBC model responses to same stimulus, respectively. Best SBC model only respond to the onset of the stimuli and low-frequency components. The response of best GBC model becomes more pronounced to the onset and low-frequency components compared to the base model.

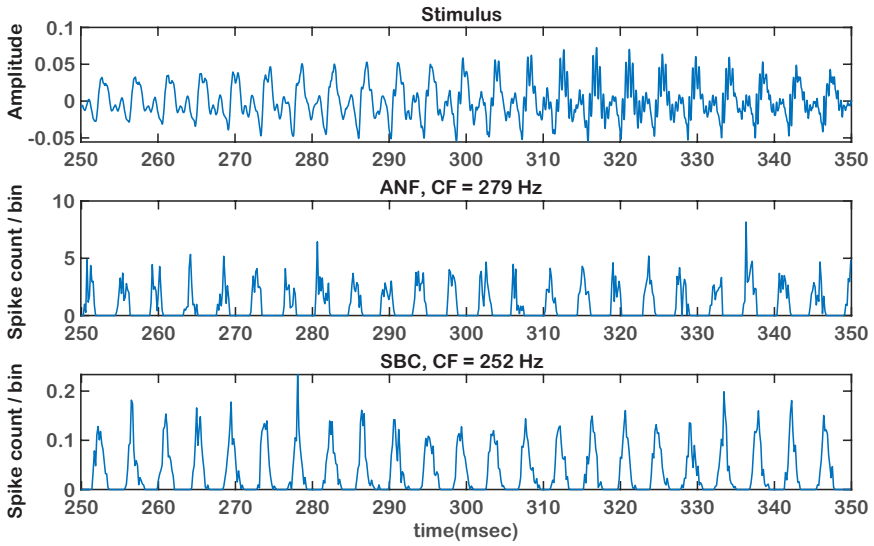

Figure 4.11: Top panel shows the stimulus section (250–350 msec) used in creating the synchronized rate responses at 65 dB SPL. Middle panel shows the PSTH response of the ANF with a CF of 279 Hz and bottom panel shows the PSTH response of the base SBC model with a CF of 252 Hz to the same stimulus section. Both ANF and base SBC models show a synchronized firing to the specific phases of the periodic stimuli.

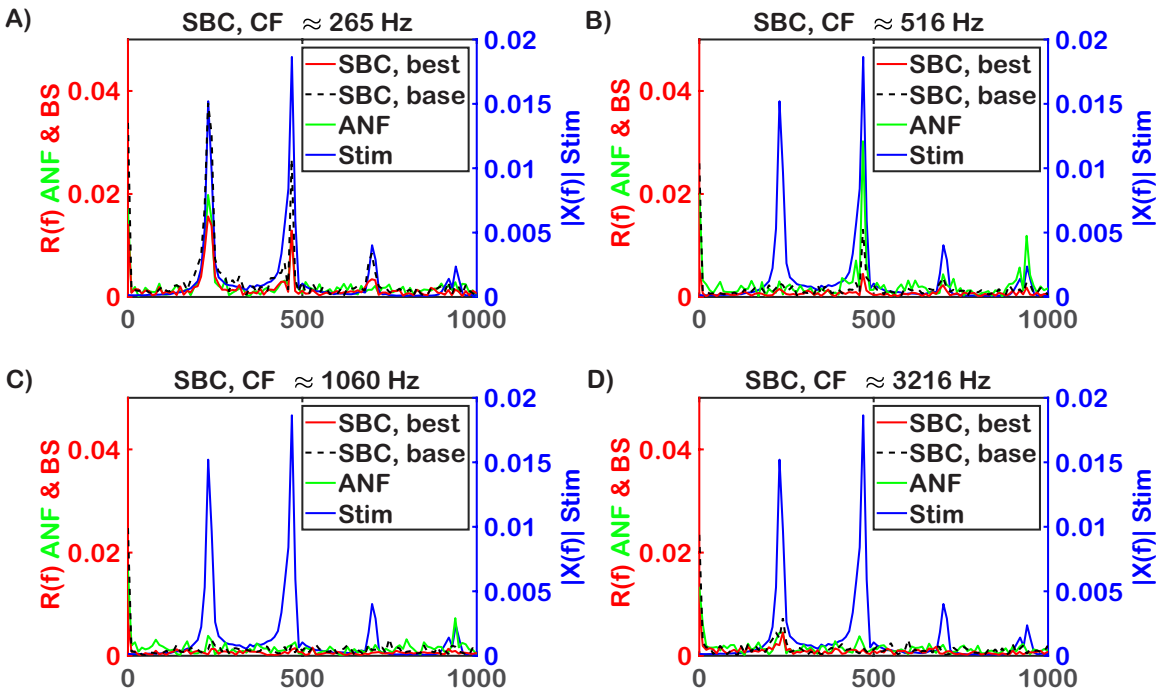

Figure 4.12: Synchronized rate plots of the base SBC model in response to the 250 msec to 350 msec portion of the sentence "How do we define it?" at 65 dB SPL. The CFs of SBCs and ANFs in the panels are as presented in Fig. 4.5. A) Base SBC model show a strong response to the first two harmonics at 230 Hz and 470 Hz at low CFs. The best SBC model shows a reduced response to the harmonics at these frequencies at low CFs. For high CFs, the responses of both base and best SBC models are diminished.

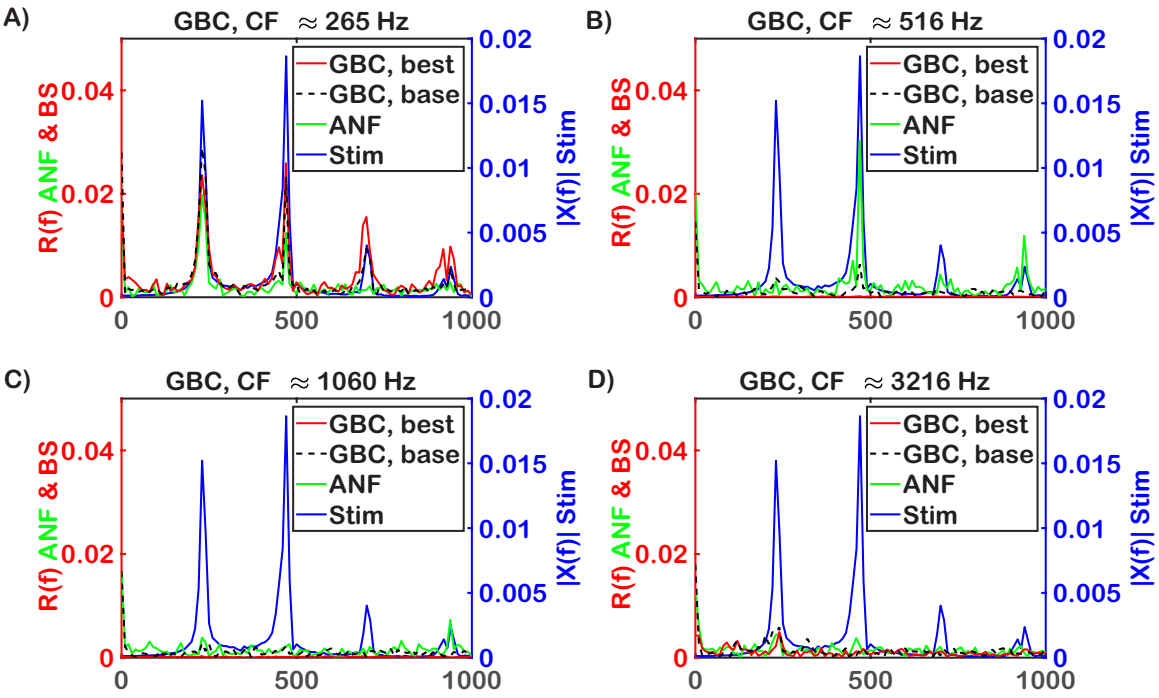

Figure 4.13: Synchronized rate plots of the base GBC model in response to the 250 msec to 350 msec portion of the sentence "How do we define it?" at 65 dB SPL. The CFs of GBCs and ANFs in the panels are as presented in Fig. 4.5. The GBC model synchronized rate plots are similar to the SBC for the specific stimulus section used in these simulations.

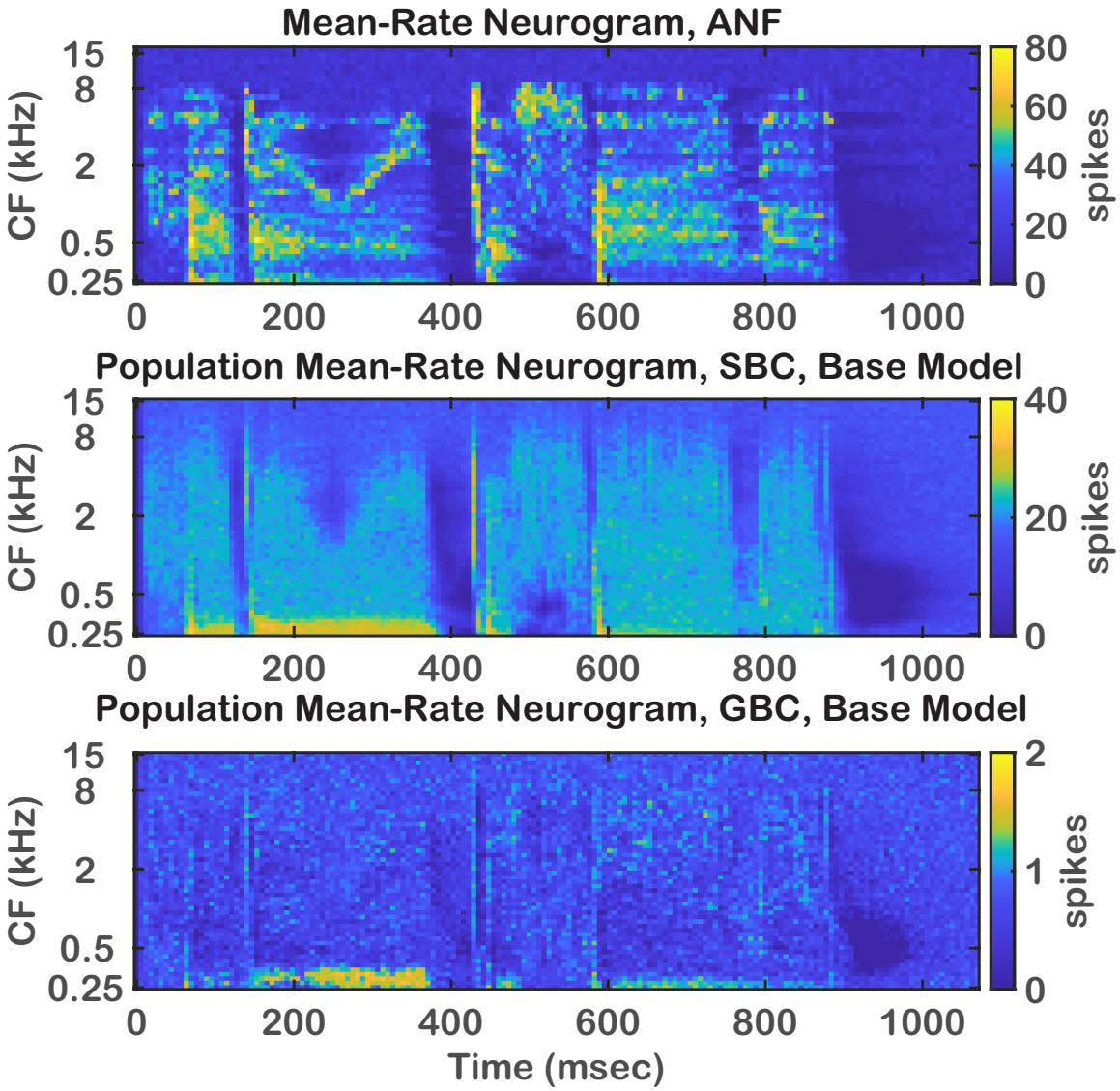

Figure 4.14: Top panel shows the mean-rate ANF neurogram response to the sentence "How do we define it?" at 65 dB SPL. Middle and bottom panels show the base SBC and GBC model neurogram responses to the the same stimulus, respectively. Base SBC model shows a strong onset response to the voiced section of the words and low-frequency resolved harmonics while the base GBC models only show a weak response to the low-frequency resolved harmonics.

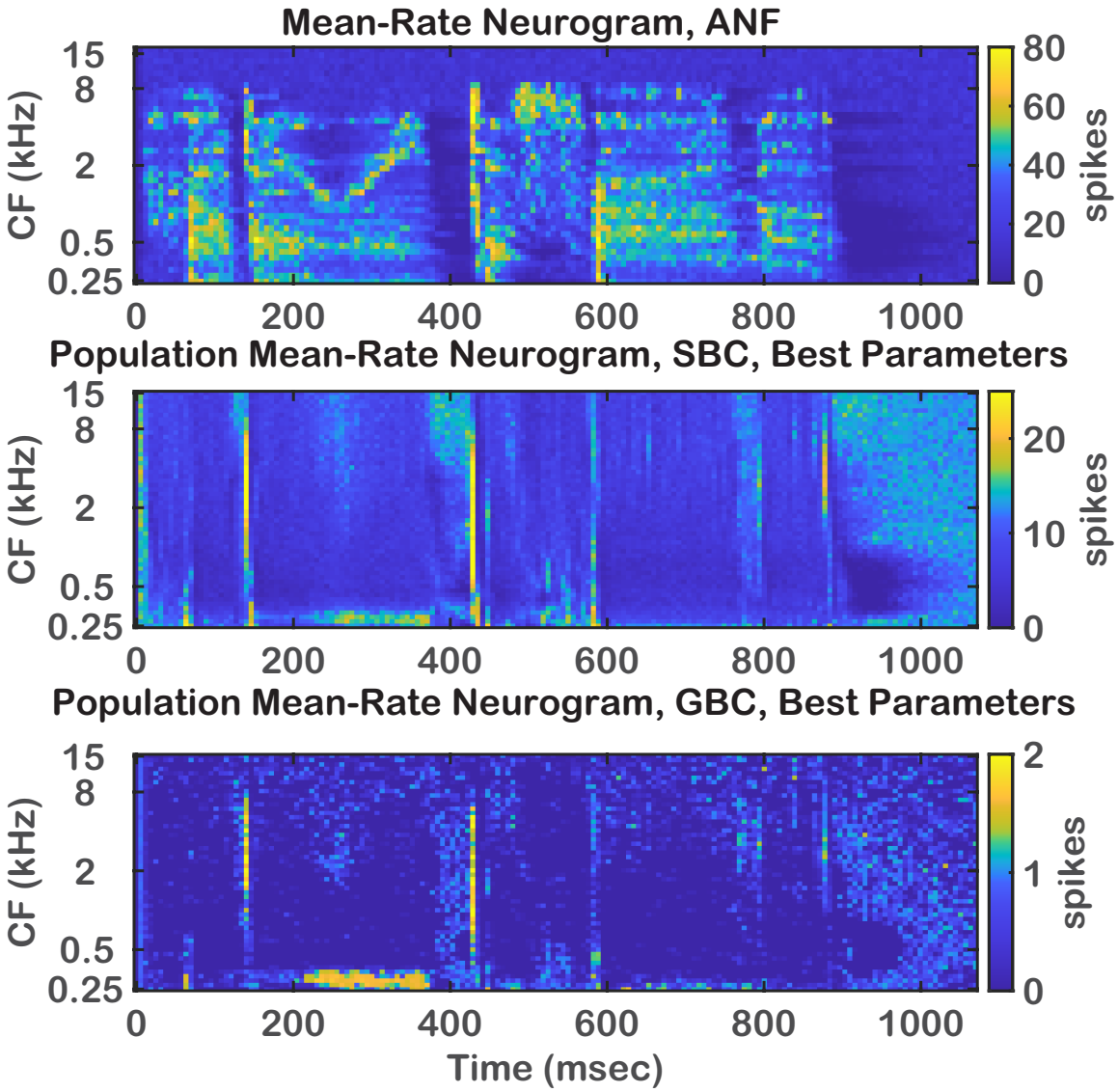

Figure 4.15: Top panel shows the mean-rate ANF neurogram response to the sentence "How do we define it?" at 65 dB SPL. Middle and bottom panels show the best SBC and GBC model neurogram responses to the the same stimulus, respectively. Best SBC model responses to low-frequency resolved harmonics are diminished while the responses to the voicing pitch is enhanced. The best GBC model does not have a significant change in the low-frequency resolved harmonic response but the response to the voicing pitch gets stronger.

4.3 Discussion & Conclusion

In this chapter, the preliminary results of base and best bushy-cell model responses to broadband stimuli, the word "besh" and the sentence "How do we define it?", was examined. The mean-rate and fine-timing neurograms show that the base SBC model (without gap junctions and inhibition) shows strong responses to the low-frequency resolved harmonics of "besh" at low CFs and the voicing pitch across a range of CFs. While the parameter sets were chosen in Chapter 3, one of the main aims was to increase the cutoff frequency of the low-pass filtering behavior seen in bushy cell models (Fig. 3.12), which increased the model responses in the mid-CF region. We can see the effect of this decision on the neurograms as the best SBC model shows a less pronounced low-frequency resolved harmonic response while enhancing the response to the voicing pitch. On the other hand, the base GBC model neurogram responses to the stimulus "besh" was sparser than the base SBC model. While the GBC model does not respond to the low-frequency resolved harmonics strongly, it still shows a distinguishable response to the voicing pitch. The GBC model created with the best parameter set only shows a strong response to the voicing pitch. The syncronized rate plots of the SBC models show how including the gap junctions and inhibition can improve responses to the voicing pitch and low-frequency harmonic components of the stimulus. While this improvement was subtle in the low-CF SBC models (Fig. 4.5A), the GBC model with high CF showed a stronger improvement consistently to the voicing pitch, with strong harmonic components due to the peaky shape of the PSTHs and rectification rather than responses to multiple harmonics in the stimulus (Fig. 4.6D).

The neurogram responses to the sentence "How do we define it?" show that the base SBC model had a strong onset and low-frequency harmonics were resolved. In the best SBC model, the low-frequency resolved harmonic response was diminished while the response to the voicing pitch was increased. Similar to the responses to "besh", the base GBC model did not show a distinguishable response to the low-frequency resolved harmonics, while the best GBC model enhanced the onset responses to the voiced segments of the words.

The results presented in this chapter suggest that when the best parameter set is chosen, neurogram responses should also be considered. Blackburn and Sachs (1990) recorded the responses of primary-like (Pri) and primary-like with notch (Pri-N) cells in VCN to the vowel /ε/ and found that spherical and globular bushy cells (Pri and Pri-N units, respectively) followed ANF vowel responses in both temporal and rate coding at low to moderate stimulus levels, but the representation of the first vowel formant was degraded in Pri cells at 55 and 75 dB SPL, which were above and below the speech level that we investigated in this chapter (65 dB SPL). Our preliminary results

were consistent with what is presented in Blackburn and Sachs (1990) since the response to the first formant frequency of high level "besh" stimuli was not pronounced in the synchronized rate plots of the SBC model. The recordings in Blackburn and Sachs (1990) do not include the low to mid CF GBCs and their responses were to stimuli above 55 dB SPL, hence we were not able to compare the GBC model results with the recorded data. In future work, the SBC and GBC cell model responses to lower dB SPL stimuli could be inspected and compared with the results presented in Blackburn and Sachs (1990). Improving the bushy-cell model responses to the broadband stimuli is important since these models can give useful insights on brainstem processing of complex sound stimuli such as speech. The bushy-cell models can be implemented in the neural-based objective speech-intelligibility metrics, such as Neurogram similarity index (NSIM) and Spectro-Temporal Modulation Index(STMI) (Elhilali *et al.*, 2003; Hines and Harte, 2012), which uses ANF neurograms to calculate the metrics, to integrate brainstem processing in the speech-intelligibility metrics.

Chapter 5

General Discussion and Conclusions

In this thesis, Hodgkin–Huxley-type bushy cell models were created to examine the effects of gap junctions and inhibition on the excitability and synchronization of the bushy cells of ventral cochlear nucleus. In Chapter 2, the effects of gap junctions on the excitability of bushy cell models were inspected mechanistically with direct current injections and synaptic inputs. Various sizes of fully connected clusters and two fully connected clusters sharing a single cell were built. The number of cells in fully connected clusters and gap junction strength were found to have a strong effect on the excitability of the bushy-cell models in a nonlinear manner. As the gap-junction strength increased, the excitability of the bushy-cell models decreased, seen as an increase in the threshold to fire an AP. Gap junctions allowed the excitation to spread within and between the fully connected clusters, and the amount of time an action potential in one cell helped the other electrically coupled cells in the cluster to fire an AP was dependent on the strength of the gap junctions. We also compared the effects of gap junctions and leakage current on the excitability of the bushy-cell models and found that both significantly affect the model excitability, but the leakage current's influence was stronger than that of the gap junctions.

Chapter 3 investigated the effect of gap junctions and inhibition on the synchronization behavior and firing rate of the bushy cell models receiving sound-driven synaptic inputs via a model of the auditory periphery. Our simulation results suggested that both gap junctions and inhibition had strong effects on the synchronization of bushy-cell models. While gap junctions caused a monotonic increase in the synchronization index scores of the bushy-cell models, the effect of inhibition on the SI scores was not as straight-forward. The maximum SI scores of populations of bushy cells indicated that the cutoff frequency of the low-pass filtering behavior of the base bushy-cell models was not high enough to match the physiological data. A parameter

set of g_{gap}, g_{inh} and k_{exct} were hand picked to obtain a higher cutoff frequency while keeping the SI scores and firing rates of the model in a physiological range, and these models are referred as the current "best models". Best bushy-cell models created in this study had very high maximum SI scores compared to ANFs, matching the physiological data, supporting the argument that gap junctions can help the bushy cells fire more synchronously.

Lastly, in Chapter 4, preliminary results of bushy cell models' responses to broadband stimuli are presented. Neurograms and synchronized rate plots were used to analyze the model responses to conversation-level speech stimuli. Fine-timing and mean-rate neurogram responses to the word "besh" revealed that the base SBC models (without gap junctions and inhibition) had strong low-frequency resolved harmonics and voicing-pitch responses. The SBC model created with the "best parameter set" chosen in Chapter 3 had a diminished harmonic response but a stronger emphasis on voicing pitch. On the other hand, the base GBC model had a weak low-frequency resolved harmonic and voicing-pitch response. The "best GBC model" shows a more pronounced response to the voicing pitch. The neurogram responses to the sentence "How do we define it?" indicated that the SBC model responses were more focused on the onset of the voiced segments of the sentence and showed a strong response to the low-frequency resolved harmonics. The "best SBC model" had even stronger responses to the voiced segments of the stimuli while the response to the low-frequency harmonics was diminished. The base GBC model responses to the low-frequency resolved harmonics and the voiced segments of the speech were less pronounced than the SBC models. The "best GBC model" had a stronger response to both of these components of the speech.

5.1 Limitations and Future Directions

The internal bushy-cell model parameters used to produce the results in this thesis were tuned for models to have a strong synchronization index scores while keeping the driven firing rates at a physiological level. One challenge we faced while choosing the "best model parameters" was that the spontaneous rates of our GBC models were consistently high across a range of CFs. Although there are biophysiological recordings reporting high-spontaneous-rate bushy cells, one of the identifying aspects of the GBCs is a tendency toward low spontaneous firing rates. In our model, we included the inhibition from D-stellate and tuberculoventral cells. These inhibitory inputs reduce the driven firing rates but have minimal effect on the spontaneous activity or responses at low sound pressure levels. One way to reduce the spontaneous firing rate could be implementing additional local inhibitory inputs, such as the recently-discovered L-stellate cells (Ngodup *et al.*, 2020). Another solution to fixing this issue

could be including a more complex synaptic model that simulates synaptic desensitization (Xie and Manis, 2013a; Spirou *et al.*, 2023). We also inspected the effect of input count on the spontaneous rate of the GBC model and found that, although including a higher number of weaker inputs can reduce the spontaneous rate, the driven rate of the GBC model was not in line with the physiological recordings. Therefore we used 12 high-spontaneous-rate ANF inputs for our GBC model, and focused on enhancing the synchronization. In the future, different input configurations such as a mixture of low, mid and high SR ANFs and strength of the subthreshold excitation can be explored to create a GBC model with both low spontaneous rate and high synchronization-index scores.

Another issue we come across while choosing the appropriate gap-junction connection strength in our model is the lack of physiological data on the gap-junction conductance between bushy cells. Gómez-Nieto and Rubio (2009) and Gómez-Nieto and Rubio (2011) present the evidence of gap junction connections between the bushy cells of the VCN, but there are no recordings done simultaneously in electrically coupled bushy cells to determine the gap junction connection strength. Considering the gap-junction conductance values reported in other parts of the brain and heart muscles, we approximated a range of gap-junction conductance between bushy-cell models and conducted the simulations using these values. In Gómez-Nieto and Rubio (2009) and Gómez-Nieto and Rubio (2011), the gap-junction connections between the bushy cells are identified as a mixture of soma-somatic and dendro-dendritic connections but a definitive cluster structure is not presented. Hence, in our simulations, we assumed all connections were soma-somatic in a fully-connected cluster structure, and for Chapters 3 and 4 only a cluster size of 5 cells was considered. Dendo-dendritic gap junctions could be included in addition to soma-somatic gap junctions in the model for further investigation, and the behavior of cluster structures other than full connectivity of 5 cells could be explored.

To choose the best parameter sets for SBC and GBC models, a visual inspection was done on the maximum SI scores of population of bushy cells, and color-map plots of SI scores and firing rates to decide the gap junction conductance and the inhibition strength. While this approach was initially useful in terms of choosing the model parameters, a more objective approach such as multi-objective optimization can also be used to better fit the model behavior to physiological data. A cost function can be created using the SI scores, firing rate and the slope of decay at the mid-frequency region on the population response plots for optimizing the internal model parameters. Although the comparison of base and best bushy cell model neurogram and synchronization rate responses gives useful insight on how the gap junctions affect the neural processing of broadband stimuli, a deeper investigation has to be done over a range of gap-junction conductances to fully understand its effect on the neural processing of speech stimuli. And the effect of gap junctions on processing of the

broadband stimuli could also be taken into count when choosing the optimal parameter set. Additionally, in Chapters 3 and 4 the model parameters were constant across all CFs. In future work, it would be interesting to determine if an improved match to both the pure-tone and vowel data could be achieved by having CF-dependent model parameters.

One issue we encountered during the development of our bushy-cell network models was the interspecies variability. The SBC and GBC, D-stellate, and tuberculoventral cell models presented in this thesis were derived from mouse data following the model of Manis and Campagnola (2018). However, the Bruce *et al.* (2018) ANF model was based on data obtained from cats, and the physiological recordings referenced in Joris *et al.* (1994) were conducted on cats. Thus, in this thesis we used a mixed-species ANF and brainstem cell model to generate predictions of bushy cell data recorded in cats. This may contribute a fundamental difficulty in optimizing model parameters to fit the bushy cell data. It would be ideal if suitable ion channel data could be collected from cat VCN cells to create a cat-specific version of the bushy-cell circuit model, however collecting such data in cat is much more difficult than in smaller species, and therefore may not be practical.

The results presented in this thesis were created by using the phenomenological Bruce *et al.* (2018) ANF model as inputs to the bushy-cell models. The ANF model was able to successfully simulate the hearing impairment caused by inner and outer hair cell loss. In our simulations, all of the ANFs are considered healthy. An impaired ANF model can be used to investigate how hearing impairment can change the behavior of the bushy cells and the neural processing of the sound signals in the brainstem.

We were interested in creating the fine-timing and mean-rate neurogram responses of bushy-cell models to complex sound stimuli, such as speech, and compare them with the ANF neurograms because of its potential use in the neural-based speech intelligibility metrics. The NSIM and STMI metrics use ANF neurograms to calculate the speech intelligibility, and implementing the brainstem processing in these metrics could be helpful. However, to fully optimize the model for prediction of human speech intelligibility, a human version of the model would be beneficial. A partially humanized version of the ANF model is available (Ibrahim and Bruce, 2010), but creating a human version of the bushy-cell circuit model would be much more difficult.

Another application of this model could be its use as an input for models of the next stages of the central auditory nervous system. The medial superior olive (MSO) and the lateral superior olive (LSO) are key stages in the brain that receives binaural inputs from bushy cells and compare them to extract interaural time difference (ITD) and interaural level difference (ILD) cues. While quite a few different models of MSO and LSO processing have been proposed in the literature, the majority of these do not included detailed biophysical models of bushy cells. One exception is the MSO model

proposed by Brughera *et al.* (1996), which used the Rothman *et al.* (1993) model of bushy cells, but the model bushy cells only received excitatory inputs from auditory nerve fibers, and inhibitory inputs from interneurons were not considered. It would be of interest to incorporate our more detailed model of SBCs and GBCs into MSO and LSO models, to determine how gap junctions and inhibitory inputs in the bushy cell circuitry affect ITD and ILD coding and processing by the MSO and LSO.

5.2 Conclusions

Investigating the neural processing of sound in the brainstem is crucial in terms of understanding how the neural cues that are used for sound localization and identification in the upper levels of the central auditory nervous system. Bushy cells are particularly important since they have the ability to encode fine-timing information and show enhanced synchronization behavior. Creating computational models of the brainstem circuitry can help us understand the mechanisms underlying the information processing in the brainstem. Although various bushy-cell models exist in the literature, this thesis describes the first biophysically detailed neural-network model of bushy cells with gap-junction connections. Hence, this work is important regarding the contributions of bushy cells in the neural processing of the sound and the potential implications of the effects of gap junctions on the behavior of bushy cells.

Appendix A

Additional equations for Chapter 2

Fast Na^+ channel:

$$I_{\text{nacn}} = \overline{g}_{\text{Na}} m^3 h (V - V_{\text{Na}}) \tag{A.1}$$

$$m_\infty = [1 + \exp(-(V + 38)/7)]^{-1} \tag{A.2}$$

$$h_\infty = [1 + \exp((V + 65)/6)]^{-1} \tag{A.3}$$

$$\tau_m = [(10/(5\exp((V + 60)/18) + 36\exp(-(V + 60)/25))) + 0.04] \tag{A.4}$$

$$\tau_h = [(100/(7\exp((V + 60)/11) + 10\exp(-(V + 60)/25))) + 0.6] \tag{A.5}$$

Hyper-polarization activated cation channel:

$$I_{\text{h}} = \overline{g}_{\text{h}} r (V - V_{\text{h}}) \tag{A.6}$$

$$r_\infty = [1 + \exp((V + 76)/7)]^{-1} \tag{A.7}$$

$$\tau_{\text{r}} = [(10000/(237\exp((V + 60)/12) + 17\exp(-(V + 60)/14))) + 25] \tag{A.8}$$

High-threshold K^+ current:

$$I_{\text{HT}} = \overline{g}_{\text{HT}}[\varphi n^2 + (1 - \varphi)p](V - V_{\text{K}}) \quad (\varphi = 0.85) \tag{A.9}$$

$$n_\infty = [1 + \exp(-(V + 15 + v_{\text{shift}})/5]^{-1/2} \quad (v_{\text{shift}} = 4.3mV) \tag{A.10}$$

$$p_\infty = [1 + \exp(-(V + 23 + v_{\text{shift}})/6)]^{-1} \tag{A.11}$$

$$\tau_{\rm n} = [(100(11\exp((V{+}60{+}v_{\rm shift})/24){+}21\exp(-(V{+}60{+}v_{\rm shift})/23))^{-1}){+}0.7] \quad \text{(A.12)}$$

$$\tau_{\rm p} = [(100(4\exp((V+60+v_{\rm shift})/32)+5\exp(-(V+60+v_{\rm shift})/22))^{-1})+5] \quad \text{(A.13)}$$

Low-threshold K^+ current:

$$I_{\rm LT} = \overline{g}_{\rm LT} w^4 z (V - V_{\rm K}) \quad \text{(A.14)}$$

$$w_\infty = [1+\exp(-(V+48)/6)]^{-1/4} \quad \text{(A.15)}$$

$$z_\infty = (1-\zeta)[1+\exp((V+71)/10)]^{-1} + \zeta \quad (\zeta = 0.5) \quad \text{(A.16)}$$

$$\tau_{\rm w} = [100(6\exp((V+60)/6)+16\exp(-(V+60)/45))^{-1}+1.5] \quad \text{(A.17)}$$

$$\tau_{\rm z} = [1000(\exp((V+60)/20)+\exp(-(V+60)/8))^{-1}+50] \quad \text{(A.18)}$$

Leakage current

$$I_{\rm leak} = \overline{g}_{\rm leak}(V - V_{\rm leak}) \quad \text{(A.19)}$$

Fast transient K^+ current:

$$I_{\rm A} = \overline{g}_A a^4 bc (V - V_K) \quad \text{(A.20)}$$

$$a_\infty = [1+\exp(-(V+31)/6)]^{-1/4} \quad \text{(A.21)}$$

$$b_\infty = [1+\exp((V+66)/7)]^{-1/2} \quad \text{(A.22)}$$

$$c_\infty = b_\infty \quad \text{(A.23)}$$

$$\tau_{\rm a} = 100[7\exp((V+60)/14)+29\exp(-(V+60)/24)]^{-1}+0.1 \quad \text{(A.24)}$$

$$\tau_{\rm b} = 1000[14\exp((V+60)/27)+29\exp(-(V+60)/24)]^{-1}+1 \quad \text{(A.25)}$$

$$\tau_{\rm c} = 90[1+\exp(-(V+66)/17)]^{-1}+10 \quad \text{(A.26)}$$

Table A.1: Model Ion Channel Parameters

Type of Channel	Max Conductance ($\overline{g}_n$, nS)	Reversal Potential (V_n, mV)
I_{Na}	2300	50
I_{h}	30	-43
I_{HT}	58	-84
I_{LT}	80	-84
I_{leak}	2	-65
I_{A}	0	-84
I_{syn}	Variable	0

Appendix B

Supplementary results for Chapter 3

The supplementary figures presented in this appendix are provided to give a better understanding of how internal model parameters such as membrane capacitance, decay time of excitatory post-synaptic currents (EPSCs), suprathreshold input level and strength of inhibition effect the synchronization index values for spherical bushy cell (SBC) models across a range of characteristic frequencies. The strength of subthreshold inputs, number of inputs and inhibition's effect on the synchronization and firing rate behavior of globular bushy cells (GBCs) are also inspected. As the membrane capacitance and the decay time of EPSCs changes, the threshold voltage of the model also changes. Therefore, the respective threshold for different membrane capacitance values and EPSC decay times is found by a pattern search algorithm on MATLAB first. Apart from the simulations where the suprathreshold input level's effect is explored, the level of suprathreshold inputs are set to be 3 times the level of threshold in the SBC simulations and 0.7 for the GBC simulations. The SI values across a range of stimulus levels and bushy cell characteristic frequencies are calculated, then the max of SI values are found according to the criteria presented in Joris *et al.* (1994).

Apart from the internal parameters' effect on the firing rate and synchronization index scores, demonstration of the propagation of excitation through gap junctions are also presented. The PSTH shapes of the models for different gap junction and inhibition strengths are also provided. The spike identification process explained in the main manuscript is shown on a voltage trace for better visual representation.

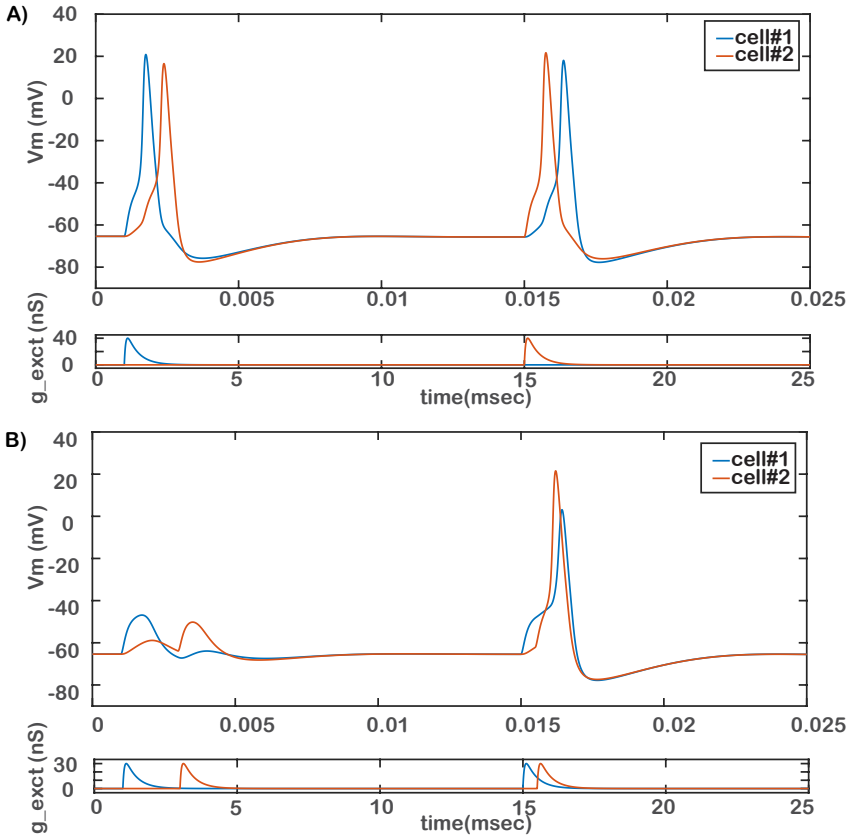

Figure B.1: A) A pair of coupled cells with a $g_{gap} = 20$ nS. At t = 1 msec, Cell #1 receives a suprathreshold input and it causes the Cell #2 to fire an action potential too, even though Cell #2 does not receive any chemical synaptic input. At t = 15 msec, Cell #2 receives a suprathreshold input and causes Cell #1 to fire an action potential, again despite the lack of chemical synaptic input to that cell. The comparison between the two action potentials produced by Cell #1 shows that the excitation coming through the gap junction can cause a delayed action potential with lower amplitude. B) A pair of coupled cells with same level of gap junction strength as in A. In this scenario, both cells receive subthreshold synaptic input. Cell #1 receives a subthreshold input at t = 1 msec while Cell #2 receives a subthreshold input at t = 3 msec. Even though the gap junction causes a displacement at the cell membrane potentials, it is not enough to help them to produce a spike. Later in the membrane trace, when both subthreshold inputs occur closer in time (t = 15.0 and 15.5 msec), the excitation spread through the gap junction now causes Cell #1 to reach threshold and fire an action potential which in turn spreads through the gap junction and help Cell #2 to fire an action potential as well. The time window where one cell helps the other cell to fire an action potential is dependent on the gap junction strength and the level of subthreshold input presented to the cells.

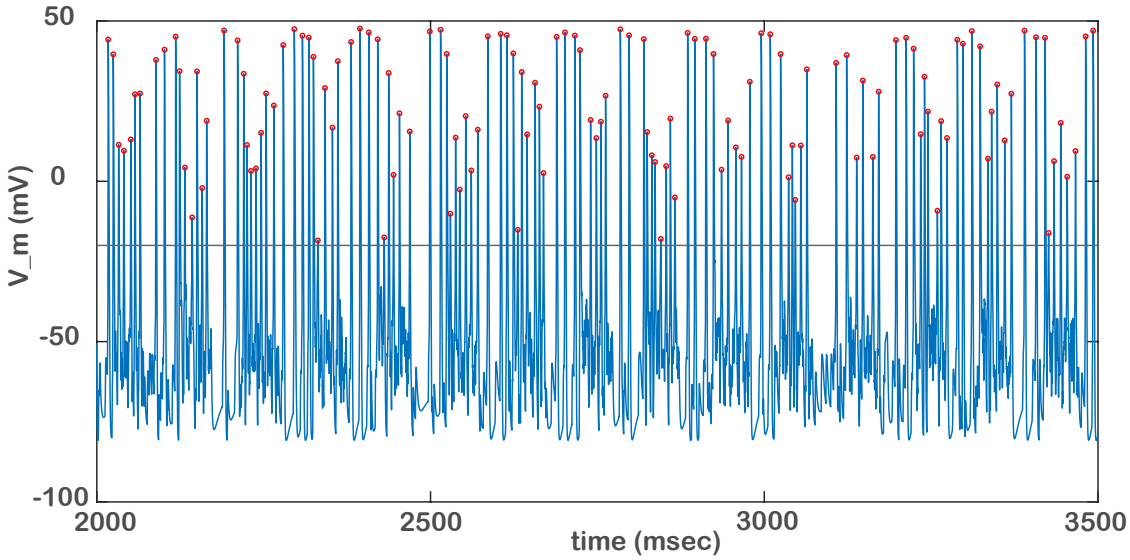

Figure B.2: An example voltage trace of an SBC model. The spikes are identified used MATLAB's built-in `findpeaks` function. The spike detection threshold is set to -20 mV. Large EPSPs occurring during the model's refractory period are excluded from being detected as spikes by setting the parameter `MinPeakDistance` to 1 msec.

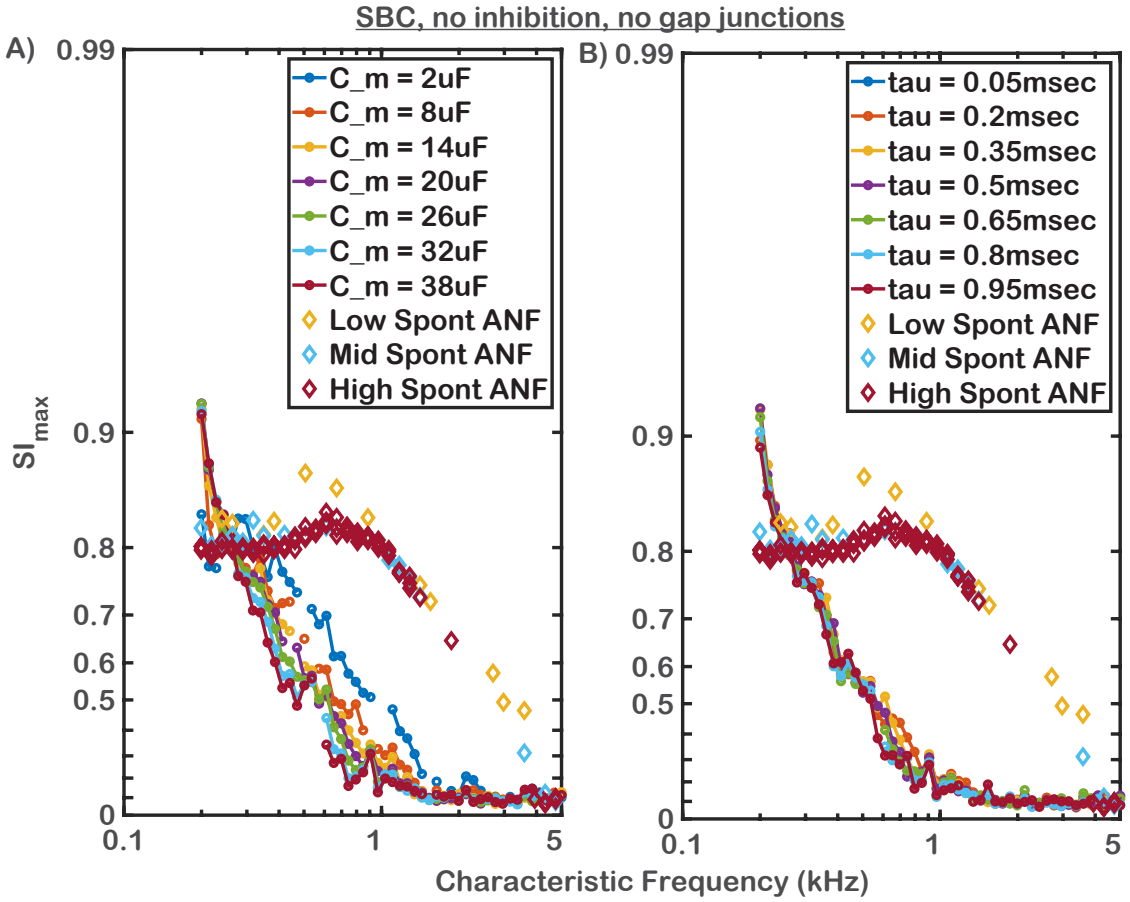

Figure B.3: A) The effect of membrane capacitance on SI across a range of SBC characteristic frequencies. As the membrane capacitance gets higher, the curves shift towards the left, lowering the cut off frequency of the low pass filtering behavior of the SBC model. No gap junctions or inhibition are included in this simulation setting. B) The effect of the EPSC decay time constant on SI across a range of SBC characteristic frequencies. The change in the EPSC decay time constant does not cause a drastic change in the cut off frequency of the low pass behavior seen in the model. No gap junctions or inhibition are included in this simulation setting.

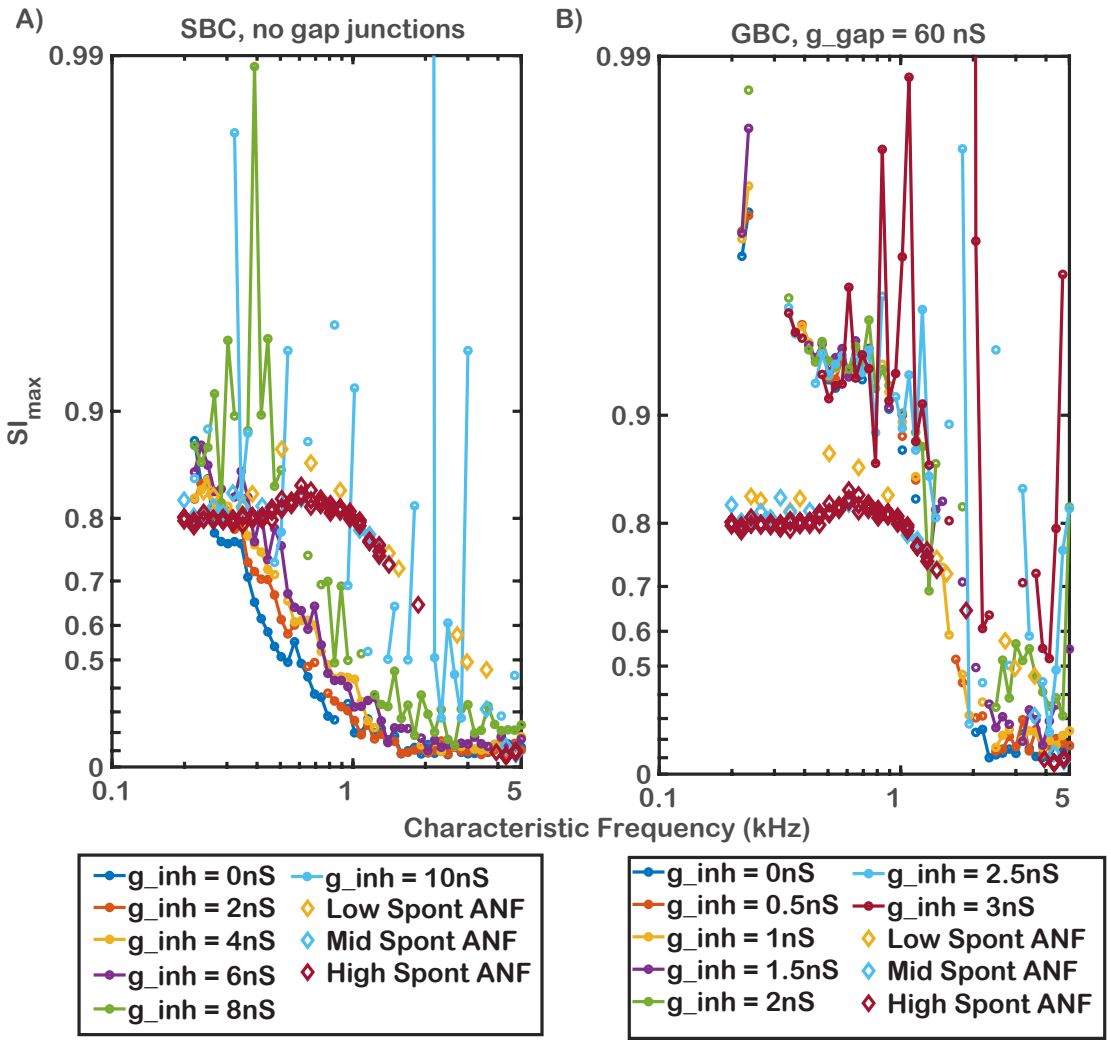

Figure B.4: Inhibition's effect on SI across a range of characteristic frequencies for SBC and GBC models. A) Inhibition has a large effect on the SI behavior of the SBC model. With no gap junctions and low strength of inhibition, the SI versus frequency curve falls below the model ANF curves. Small increases in the strength of inhibition cause the SBC curves to shifts more towards the ANF curves. Higher levels of inhibition cause high but erratic SI scores because many SBC model spikes are eliminated by the inhibition and the remaining few spikes tend to occur in the same time bin. B) Inhibition's effect on SI across a range of GBC characteristic frequencies. A large gap junction conductance of $g_{gap} = 60$ nS was used here to better enable a potential effect of inhibition, however the inhibition's effect on the cutoff frequency behavior is observed to be minimal for GBCs for lower levels of inhibition, while for strong inhibition the SI scores tend to be erratic, as was also observed for the SBC model in Panel A.

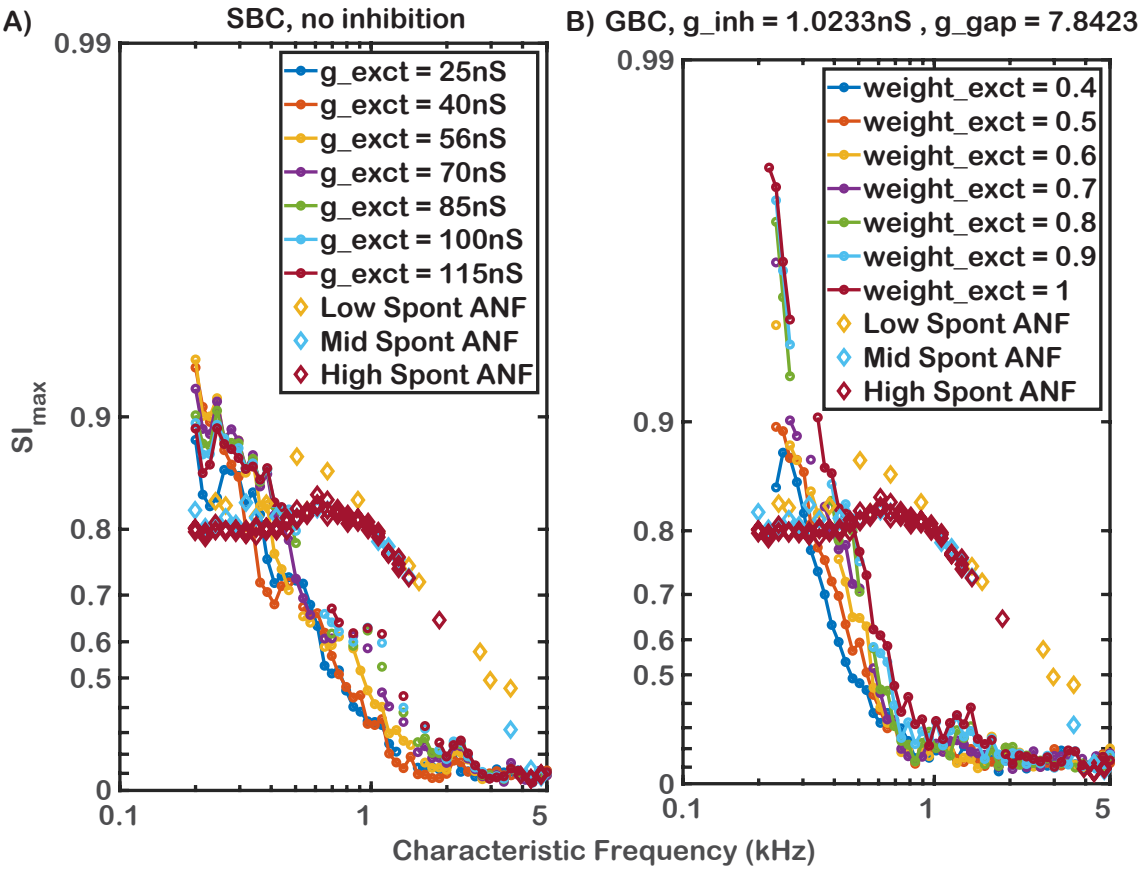

Figure B.5: A) The effect of the EPSC amplitude on SI across a range of SBC characteristic frequencies. $\bar{g}_{exct} = 25$ nS is the threshold value for the bushy cell model used. No gap junctions or inhibition is present in these simulations. Although the increase in the level of excitation shifts the curve towards the curve obtained from the ANF simulations, the cut off frequency is still too low compared to the physiological data. B) The effect of the subthreshold excitatory multiplier (k_{exct}) on SI across a range of characteristic frequencies for model GBCs. As k_{exct} increases, the cut off frequency of the low pass behavior seen in the model shifts towards higher frequencies which makes the model more biophysically feasible. But considering the GBCs receive subthreshold inputs, increasing the k_{exct} makes the model working close to the threshold instead of subthreshold, therefore a k_{exct} value of 0.7 is chosen in our set of "best parameters" for the GBC model.

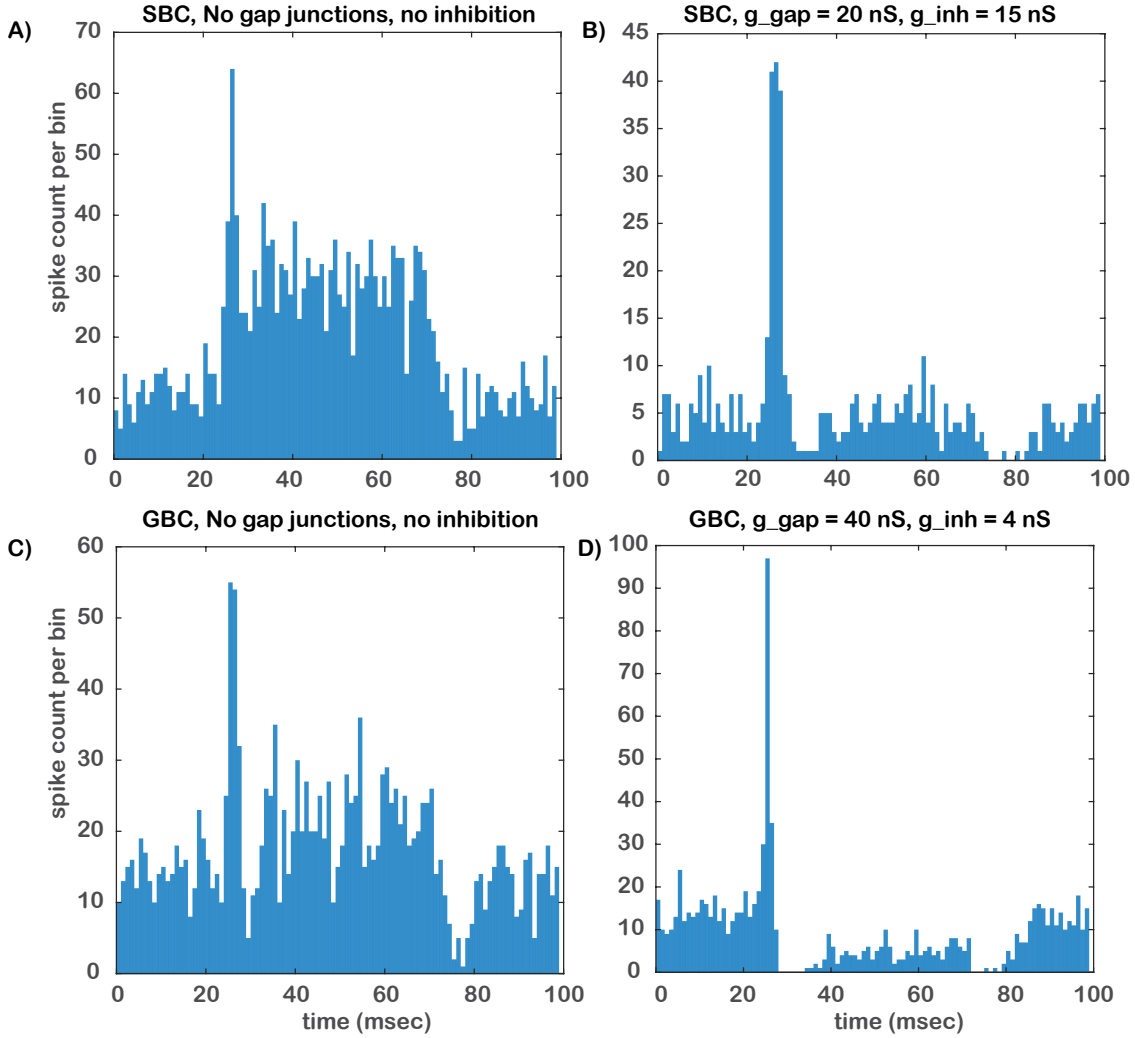

Figure B.6: PSTHs of the GBC and SBC models with CF = 1544 Hz. The models are presented with 30 dB SPL sinosidal inputs with a rise and fall time of 3.9 msec. The stimulus duration is 50 msec, followed by 50 msec of silence. The stimulus is presented to the model 200 times as a single long signal, with an initial onset time at 20 msec, such that the total duration of the stimulus is 20 seconds. The bin width for the PSTHs shown in this figure is 1 msec. A) PSTH of an SBC model with a CF of 1544 Hz. No gap junction or inhibitory connections are included. The model exhibits a primary-like response. B) PSTH of an SBC model with a CF of 1544 Hz. The model has a $g_{gap} = 20$ nS, $g_{inh} = 15$ nS and the $k_{exct} = 4$. The model shows an enhanced onset response with reduced late activity. C) PSTH of a GBC model with a CF of 1544 Hz. No gap junction or inhibitory connections are included. The model exhibits a primary-like with notch response. D) PSTH of a GBC model with a CF of 1544 Hz. The model has a $g_{gap} = 40$ nS, $g_{inh} = 4$ nS and the $k_{exct} = 0.7$. The model shows a strong onset response with a notch followed by reduced late activity.

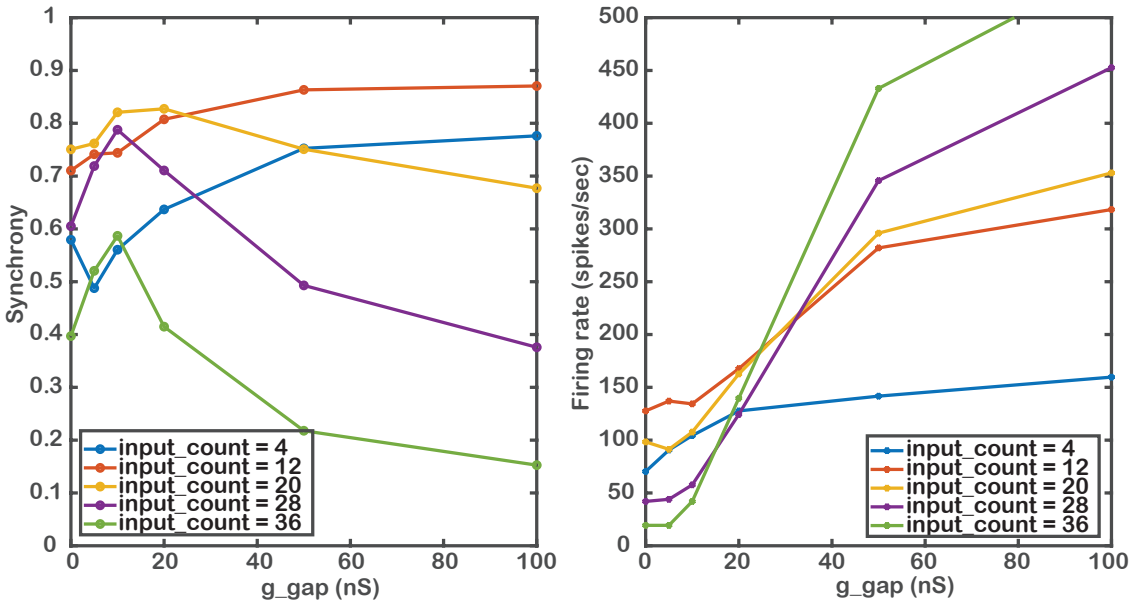

Figure B.7: The effect of the number of subthreshold inputs on the synchronization and firing rate across a range of gap junction levels in a fully connected cluster of GBCs with CFs around 340 Hz. A stimulus level of 40 dB SPL is presented to the model. Synchronization index as a function of gap junction strength is plotted in the panel on the left. For lower input counts, increasing the gap junction strength causes a monotonic increase in SI scores. As the number of inputs becomes higher, the increase in g_{gap} causes an increase in SI for low levels, but this effect saturates and starts causing a decrease as g_{gap} levels gets higher and higher. As shown in the panel on the right, increasing gap junction strength causes a monotonic increase in firing rate of the model GBC with a CF of 336 Hz, and the rate of growth is dependent on the number of synaptic inputs. For gap junction strengths above $\sim$ 30 nS, increasing the number of synaptic inputs causes a monotonic increase in the firing rate at 40 dB SPL. In contrast, for lower gap junction strengths the firing rate at 40 dB SPL first increases with an increasing number of synaptic inputs but then drops again. The effect of input count on the spontaneous rate is more clear; as the input count increases, the spontaneous rate of the model increases (not presented in this figure).

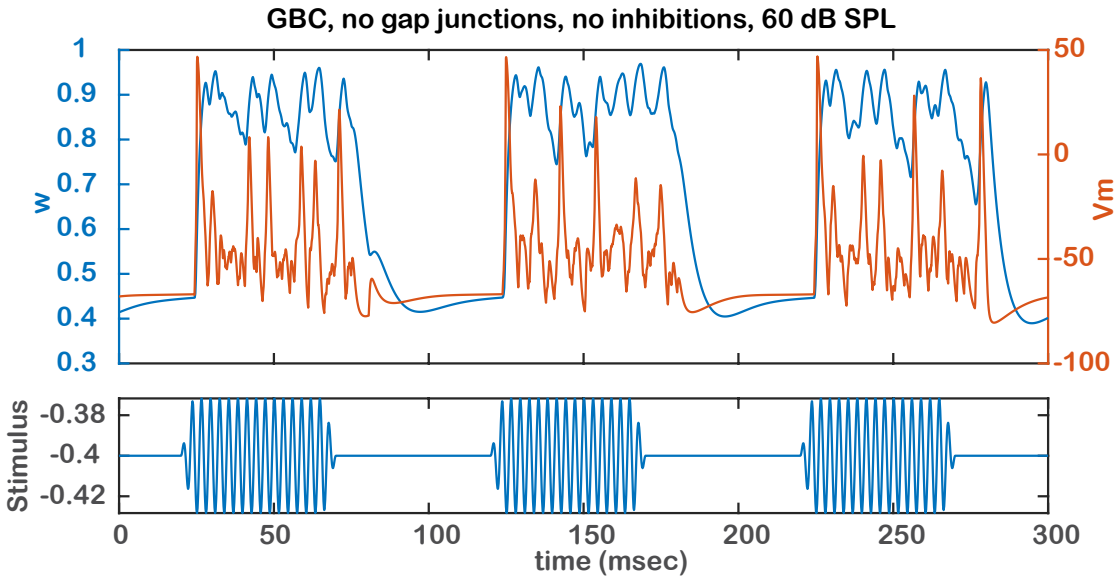

Figure B.8: Simulation results for the GBC model, showing the activation gating particle 'w' of the low threshold potassium channel I_{LT} and the membrane potential's trajectory over time in response to a 340 Hz pure tone stimulus presented at 60 dB SPL. It can be observed that if a large number of synaptic inputs arrive within a short time period, the I_{LT} channel activates and action potential generation is suppressed until the 'w' parameter drops sufficiently low.

Bibliography

Alcamí, P. and Pereda, A. E. (2019). Beyond plasticity: the dynamic impact of electrical synapses on neural circuits. *Nature Reviews Neuroscience*, **20**(5), 253–271.

Apostolides, P. F. and Trussell, L. O. (2013). Regulation of interneuron excitability by gap junction coupling with principal cells. *Nature Neuroscience*, **16**(12), 1764–1772.

Arnott, R. H., Wallace, M. N., Shackleton, T. M., and Palmer, A. R. (2004). Onset neurones in the anteroventral cochlear nucleus project to the dorsal cochlear nucleus. *Journal of the Association for Research in Otolaryngology*, **5**, 153–170.

Ashida, G., Heinermann, H. T., and Kretzberg, J. (2019). Neuronal population model of globular bushy cells covering unit-to-unit variability. *PLoS Computational Biology*, **15**(12), e1007563.

Belluardo, N., Mudò, G., Trovato-Salinaro, A., Le Gurun, S., Charollais, A., Serre-Beinier, V., Amato, G., Haefliger, J.-A., Meda, P., and Condorelli, D. F. (2000). Expression of connexin36 in the adult and developing rat brain. *Brain research*, **865**(1), 121–138.

Bennett, M. V. and Zukin, R. S. (2004). Electrical coupling and neuronal synchronization in the mammalian brain. *Neuron*, **41**(4), 495–511.

Blackburn, C. C. and Sachs, M. B. (1990). The representations of the steady-state vowel sound /ɛ/ in the discharge patterns of cat anteroventral cochlear nucleus neurons. *Journal of Neurophysiology*, **63**(5), 1191–1212.

Bruce, I. C., Erfani, Y., and Zilany, M. S. (2018). A phenomenological model of the synapse between the inner hair cell and auditory nerve: Implications of limited neurotransmitter release sites. *Hearing Research*, **360**, 40–54.

Brughera, A. R., Stutman, E. R., Carney, L. H., and Colburn, H. S. (1996). A model with excitation and inhibition for cells in the medial superior olive. *Auditory Neuroscience*, **2**, 219–233.

Campagnola, L. and Manis, P. B. (2014). A map of functional synaptic connectivity in the mouse anteroventral cochlear nucleus. *Journal of Neuroscience*, **34**(6), 2214–2230.

Cant, N. B. and Benson, C. G. (2003). Parallel auditory pathways: projection patterns of the different neuronal populations in the dorsal and ventral cochlear nuclei. *Brain Research Bulletin*, **60**(5-6), 457–474.

Cao, X.-J. and Oertel, D. (2010). Auditory nerve fibers excite targets through synapses that vary in convergence, strength, and short-term plasticity. *Journal of Neurophysiology*, **104**(5), 2308–2320.

Cao, X.-J., Shatadal, S., and Oertel, D. (2007). Voltage-sensitive conductances of bushy cells of the mammalian ventral cochlear nucleus. *Journal of Neurophysiology*, **97**(6), 3961–3975.

Condorelli, D. F., Belluardo, N., Trovato-Salinaro, A., and Mudò, G. (2000). Expression of Cx36 in mammalian neurons. *Brain Research Reviews*, **32**(1), 72–85.

Curti, S., Hoge, G., Nagy, J. I., and Pereda, A. E. (2012). Synergy between electrical coupling and membrane properties promotes strong synchronization of neurons of the mesencephalic trigeminal nucleus. *Journal of Neuroscience*, **32**(13), 4341–4359.

Curti, S., Davoine, F., and Dapino, A. (2022). Function and plasticity of electrical synapses in the mammalian brain: role of non-junctional mechanisms. *Biology*, **11**(1), 81.

De Zeeuw, C. I., Hoogenraad, C. C., Koekkoek, S., Ruigrok, T. J., Galjart, N., and Simpson, J. I. (1998). Microcircuitry and function of the inferior olive. *Trends in Neurosciences*, **21**(9), 391–400.

Dehmel, S., Kopp-Scheinpflug, C., Weick, M., Dörrscheidt, G. J., and Rübsamen, R. (2010). Transmission of phase-coupling accuracy from the auditory nerve to spherical bushy cells in the Mongolian gerbil. *Hearing Research*, **268**(1-2), 234–249.

Dermietzel, R. and Spray, D. C. (1993). Gap junctions in the brain: where, what type, how many and why? *Trends in Neurosciences*, **16**(5), 186–192.

Devor, A. and Yarom, Y. (2002). Electrotonic coupling in the inferior olivary nucleus revealed by simultaneous double patch recordings. *Journal of Neurophysiology*, **87**(6), 3048–3058.

Doucet, J. R. and Ryugo, D. K. (2006). Structural and functional classes of multipolar cells in the ventral cochlear nucleus. *The Anatomical Record Part A: Discoveries in Molecular, Cellular, and Evolutionary Biology: An Official Publication of the American Association of Anatomists*, **288**(4), 331–344.

Elhilali, M., Chi, T., and Shamma, S. A. (2003). A spectro-temporal modulation index (stmi) for assessment of speech intelligibility. *Speech Communication*, **41**(2-3), 331–348.

Ferragamo, M. J., Golding, N. L., and Oertel, D. (1998). Synaptic inputs to stellate cells in the ventral cochlear nucleus. *Journal of Neurophysiology*, **79**(1), 51–63.

Fukuda, T. and Kosaka, T. (2000). Gap junctions linking the dendritic network of GABAergic interneurons in the hippocampus. *Journal of Neuroscience*, **20**(4), 1519–1528.

Gardner, S. M., Trussell, L. O., and Oertel, D. (1999). Time course and permeation of synaptic ampa receptors in cochlear nuclear neurons correlate with input. *Journal of Neuroscience*, **19**(20), 8721–8729.

Getting, P. and Willows, A. (1974). Modification of neuron properties by electrotonic synapses. ii. burst formation by electrotonic synapses. *Journal of Neurophysiology*, **37**(5), 858–868.

Getting, P. A. (1974). Modification of neuron properties by electrotonic synapses. i. input resistance, time constant, and integration. *Journal of Neurophysiology*, **37**(5), 846–857.

Gómez-Nieto, R. and Rubio, M. (2011). Ultrastructure, synaptic organization, and molecular components of bushy cell networks in the anteroventral cochlear nucleus of the rhesus monkey. *Neuroscience*, **179**, 188–207.

Gómez-Nieto, R. and Rubio, M. E. (2009). A bushy cell network in the rat ventral cochlear nucleus. *Journal of Comparative Neurology*, **516**(4), 241–263.

Grothe, B., Pecka, M., and McAlpine, D. (2010). Mechanisms of sound localization in mammals. *Physiological Reviews*, **90**(3), 983–1012.

Hines, A. and Harte, N. (2012). Speech intelligibility prediction using a neurogram similarity index measure. *Speech Communication*, **54**(2), 306–320.

Hoppensteadt, F. C. and Izhikevich, E. M. (2012). *Weakly connected neural networks*, volume 126. Springer Science & Business Media.

Ibrahim, R. A. and Bruce, I. C. (2010). Effects of peripheral tuning on the auditory nerve's representation of speech envelope and temporal fine structure cues. In E. A. Lopez-Poveda, A. R. Palmer, and R. Meddis, editors, *The Neurophysiological Bases of Auditory Perception*, pages 429–438, New York, NY. Springer New York.

Johnson, D. H. (1980). The relationship between spike rate and synchrony in responses of auditory-nerve fibers to single tones. *The Journal of the Acoustical Society of America*, **68**(4), 1115–1122.

Jongsma, H. J. and Wilders, R. (2000). Gap junctions in cardiovascular disease. *Circulation Research*, **86**(12), 1193–1197.

Joris, P. X. and Smith, P. H. (2008). The volley theory and the spherical cell puzzle. *Neuroscience*, **154**(1), 65–76.

Joris, P. X., Carney, L. H., Smith, P. H., and Yin, T. (1994). Enhancement of neural synchronization in the anteroventral cochlear nucleus. I. Responses to tones at the characteristic frequency. *Journal of Neurophysiology*, **71**(3), 1022–1036.

Joris, P. X., Smith, P. H., and Yin, T. C. (1998). Coincidence detection in the auditory system: 50 years after jeffress. *Neuron*, **21**(6), 1235–1238.

Keine, C., Rübsamen, R., and Englitz, B. (2016). Inhibition in the auditory brainstem enhances signal representation and regulates gain in complex acoustic environments. *eLife*, **5**, e19295.

Keine, C., Rübsamen, R., and Englitz, B. (2017). Signal integration at spherical bushy cells enhances representation of temporal structure but limits its range. *eLife*, **6**, e29639.

Koert, E. and Kuenzel, T. (2021). Small dendritic synapses enhance temporal coding in a model of cochlear nucleus bushy cells. *Journal of Neurophysiology*, **125**(3), 915–937.

Kuenzel, T., Nerlich, J., Wagner, H., Rübsamen, R., and Milenkovic, I. (2015). Inhibitory properties underlying non-monotonic input-output relationship in low-frequency spherical bushy neurons of the gerbil. *Frontiers in Neural Circuits*, **9**, 14.

Kuo, S. P., Lu, H.-W., and Trussell, L. O. (2012). Intrinsic and synaptic properties of vertical cells of the mouse dorsal cochlear nucleus. *Journal of Neurophysiology*, **108**(4), 1186–1198.

Li, Z. and Hatton, G. I. (1996). Oscillatory bursting of phasically firing rat supraoptic neurones in low-Ca2+ medium: Na+ influx, cytosolic Ca2+ and gap junctions. *The Journal of Physiology*, **496**(2), 379–394.

Liberman, M. C. (1978). Auditory-nerve response from cats raised in a low-noise chamber. *The Journal of the Acoustical Society of America*, **63**(2), 442–455.

Liberman, M. C. (1991). Central projections of auditory-nerve fibers of differing spontaneous rate. I. Anteroventral cochlear nucleus. *Journal of Comparative Neurology*, **313**(2), 240–258.

Loewenstein, Y., Yarom, Y., and Sompolinsky, H. (2001). The generation of oscillations in networks of electrically coupled cells. *Proceedings of the National Academy of Sciences*, **98**(14), 8095–8100.

Louage, D. H., van der Heijden, M., and Joris, P. X. (2005). Enhanced temporal response properties of anteroventral cochlear nucleus neurons to broadband noise. *Journal of Neuroscience*, **25**(6), 1560–1570.

Manis, P. B. and Campagnola, L. (2018). A biophysical modelling platform of the cochlear nucleus and other auditory circuits: from channels to networks. *Hearing Research*, **360**, 76–91.

Manis, P. B. and Marx, S. O. (1991). Outward currents in isolated ventral cochlear nucleus neurons. *Journal of Neuroscience*, **11**(9), 2865–2880.

Manis, P. B., Kasten, M. R., and Xie, R. (2019). Classification of neurons in the adult mouse cochlear nucleus: Linear discriminant analysis. *PloS One*, **14**(10), e0223137.

Manor, Y., Rinzel, J., Segev, I., and Yarom, Y. (1997). Low-amplitude oscillations in the inferior olive: a model based on electrical coupling of neurons with heterogeneous channel densities. *Journal of Neurophysiology*, **77**(5), 2736–2752.

Mercer, A., Bannister, A. P., and Thomson, A. M. (2006). Electrical coupling between pyramidal cells in adult cortical regions. *Brain Cell Biology*, **35**, 13–27.

Migliore, M., Hines, M. L., and Shepherd, G. M. (2005). The role of distal dendritic gap junctions in synchronization of mitral cell axonal output. *Journal of Computational Neuroscience*, **18**, 151–161.

Needham, K. and Paolini, A. G. (2006). Neural timing, inhibition and the nature of stellate cell interaction in the ventral cochlear nucleus. *Hearing Research*, **216**, 31–42.

Ngodup, T., Romero, G. E., and Trussell, L. O. (2020). Identification of an inhibitory neuron subtype, the L-stellate cell of the cochlear nucleus. *eLife*, **9**, e54350.

Oertel, D. (1983). Synaptic responses and electrical properties of cells in brain slices of the mouse anteroventral cochlear nucleus. *Journal of Neuroscience*, **3**(10), 2043–2053.

Oertel, D. and Wickesberg, R. E. (1993). Glycinergic inhibition in the cochlear nuclei: evidence for tuberculoventral neurons being glycinergic. In *The Mammalian Cochlear Nuclei: Organization and Function*, pages 225–237. Springer.

Oertel, D., Wright, S., Cao, X.-J., Ferragamo, M., and Bal, R. (2011). The multiple functions of t stellate/multipolar/chopper cells in the ventral cochlear nucleus. *Hearing Research*, **276**(1-2), 61–69.

Osen, K. K. and Roth, K. (1969). Histochemical localization of cholinesterases in the cochlear nuclei of the cat, with notes on the origin of acetylcholinesterase-positive afferents and the superior olive. *Brain Research*, **16**(1), 165–185.

Perez-Velazquez, J., Valiante, T. A., and Carlen, P. L. (1994). Modulation of gap junctional mechanisms during calcium-free induced field burst activity: a possible role for electrotonic coupling in epileptogenesis. *Journal of Neuroscience*, **14**(7), 4308–4317.

Perez Velazquez, J. L. (2003). Brief note: mathematics and the gap junctions: in-phase synchronization of identical neurons. *International Journal of Neuroscience*, **113**(8), 1095–1101.

Pickles, J. (2013). *An Introduction to the Physiology of Hearing*. 4th Ed. Brill Academic Publishers, Leiden, NL.

Rhode, W., Oertel, D., and Smith, P. (1983). Physiological response properties of cells labeled intracellularly with horseradish peroxidase in cat ventral cochlear nucleus. *Journal of Comparative Neurology*, **213**(4), 448–463.

Rhode, W. S. (2008). Response patterns to sound associated with labeled globular/bushy cells in cat. *Neuroscience*, **154**(1), 87–98.

Rhode, W. S. and Smith, P. H. (1986). Encoding timing and intensity in the ventral cochlear nucleus of the cat. *Journal of Neurophysiology*, **56**(2), 261–286.

Rose, J. E., Hind, J. E., Anderson, D. J., and Brugge, J. F. (1971). Some effects of stimulus intensity on response of auditory nerve fibers in the squirrel monkey. *Journal of Neurophysiology*, **34**(4), 685–699.

Rothman, J. S. and Manis, P. B. (2003). The roles potassium currents play in regulating the electrical activity of ventral cochlear nucleus neurons. *Journal of Neurophysiology*, **89**(6), 3097–3113.

Rothman, J. S. and Young, E. D. (1996). Enhancement of neural synchronization in computational models of ventral cochlear nucleus bushy cells. *Auditory Neuroscience*, **2**, 47–62.

Rothman, J. S., Young, E. D., and Manis, P. B. (1993). Convergence of auditory nerve fibers onto bushy cells in the ventral cochlear nucleus: implications of a computational model. *Journal of Neurophysiology*, **70**(6), 2562–2583.

Rubio, M. and Nagy, J. (2015). Connexin36 expression in major centers of the auditory system in the CNS of mouse and rat: Evidence for neurons forming purely electrical synapses and morphologically mixed synapses. *Neuroscience*, **303**, 604–629.

Rudnicki, M. and Hemmert, W. (2017). High entrainment constrains synaptic depression levels of an in vivo globular bushy cell model. *Frontiers in Computational Neuroscience*, **11**, 16.

Ryugo, D. K. and Parks, T. N. (2003). Primary innervation of the avian and mammalian cochlear nucleus. *Brain Research Bulletin*, **60**(5-6), 435–456.

Schwarz, D. W. and Puil, E. (1997). Firing properties of spherical bushy cells in the anteroventral cochlear nucleus of the gerbil. *Hearing Research*, **114**(1-2), 127–138.

Shaffer, A., Follmann, R., Harris, A. L., Postnova, S., Braun, H., and Rosa, E. (2017). A critical firing rate associated with tonic-to-bursting transitions in synchronized gap-junction coupled neurons. *The European Physical Journal Special Topics*, **226**, 1939–1951.

Sharp, A. A., Abbott, L., and Marder, E. (1992). Artificial electrical synapses in oscillatory networks. *Journal of Neurophysiology*, **67**(6), 1691–1694.

Smith, P. H. and Rhode, W. S. (1987). Characterization of HRP-labeled globular bushy cells in the cat anteroventral cochlear nucleus. *Journal of Comparative Neurology*, **266**(3), 360–375.

Smith, P. H., Joris, P. X., and Yin, T. C. (1993). Projections of physiologically characterized spherical bushy cell axons from the cochlear nucleus of the cat: evidence for delay lines to the medial superior olive. *Journal of Comparative Neurology*, **331**(2), 245–260.

Spirou, G., Rager, J., and Manis, P. (2005). Convergence of auditory-nerve fiber projections onto globular bushy cells. *Neuroscience*, **136**(3), 843–863.

Spirou, G. A., Kersting, M., Carr, S., Razzaq, B., Pinto, C. Y. A., Dawson, M., Ellisman, M. H., and Manis, P. B. (2023). High-resolution volumetric imaging constrains compartmental models to explore synaptic integration and temporal processing by cochlear nucleus globular bushy cells. *eLife*, **12**, e83393.

Traub, R. D., Schmitz, D., Jefferys, J. G., and Draguhn, A. (1999). High-frequency population oscillations are predicted to occur in hippocampal pyramidal neuronal networks interconnected by axoaxonal gap junctions. *Neuroscience*, **92**(2), 407–426.

Traub, R. D., Draguhn, A., Whittington, M. A., Baldeweg, T., Bibbig, A., Buhl, E. H., and Schmitz, D. (2002). Axonal gap junctions between principal neurons: a novel source of network oscillations, and perhaps epileptogenesis. *Reviews in the Neurosciences*, **13**(1), 1–30.

Traub, R. D., Cunningham, M. O., and Whittington, M. A. (2011). Chemical synaptic and gap junctional interactions between principal neurons: partners in epileptogenesis. *Neural Networks*, **24**(6), 515–525.

Typlt, M., Englitz, B., Sonntag, M., Dehmel, S., Kopp-Scheinpflug, C., and Ruebsamen, R. (2012). Multidimensional characterization and differentiation of neurons in the anteroventral cochlear nucleus. *PloS One*, **7**(1), e29965.

Wang, M., Zhang, C., Lin, S., Wang, Y., Seicol, B. J., Ariss, R. W., and Xie, R. (2021). Biased auditory nerve central synaptopathy is associated with age-related hearing loss. *The Journal of Physiology*, **599**(6), 1833–1854.

Wang, Y., Wang, M., and Xie, R. (2019). D-stellate neurons of the ventral cochlear nucleus decrease in auditory nerve-evoked activity during age-related hearing loss. *Brain Sciences*, **9**(11), 302.

Watanabe, A. (1958). The interaction of electrical activity among neurons of lobster cardiac ganglion. *The Japanese Journal of Physiology*, **8**, 305–318.

Wei, L., Karino, S., Verschooten, E., and Joris, P. X. (2017). Enhancement of phase-locking in rodents. I. an axonal recording study in gerbil. *Journal of Neurophysiology*, **118**(4), 2009–2023.

Wickesberg, R. E. and Oertel, D. (1990). Delayed, frequency-specific inhibition in the cochlear nuclei of mice: a mechanism for monaural echo suppression. *Journal of Neuroscience*, **10**(6), 1762–1768.

Wirtzfeld, M. R., Ibrahim, R. A., and Bruce, I. C. (2017). Predictions of speech chimaera intelligibility using auditory nerve mean-rate and spike-timing neural cues. *Journal of the Association for Research in Otolaryngology*, **18**, 687–710.

Wouterlood, F., Mugnaini, E., Osen, K., and Dahl, A. L. (1984). Stellate neurons in rat dorsal cochlear nucleus studied with combined Golgi impregnation and electron microscopy: synaptic connections and mutual coupling by gap junctions. *Journal of Neurocytology*, **13**, 639–664.

Xie, R. and Manis, P. B. (2013a). Glycinergic synaptic transmission in the cochlear nucleus of mice with normal hearing and age-related hearing loss. *Journal of Neurophysiology*, **110**(8), 1848–1859.

Xie, R. and Manis, P. B. (2013b). Target-specific IPSC kinetics promote temporal processing in auditory parallel pathways. *Journal of Neuroscience*, **33**(4), 1598–1614.

Xie, R. and Manis, P. B. (2017a). Radiate and planar multipolar neurons of the mouse anteroventral cochlear nucleus: Intrinsic excitability and characterization of their auditory nerve input. *Frontiers in Neural Circuits*, **11**, 77.

Xie, R. and Manis, P. B. (2017b). Synaptic transmission at the endbulb of Held deteriorates during age-related hearing loss. *The Journal of Physiology*, **595**(3), 919–934.

Yaeger, D. B. and Trussell, L. O. (2016). Auditory Golgi cells are interconnected predominantly by electrical synapses. *Journal of Neurophysiology*, **116**(2), 540–551.

Young, E. D. and Oertel, D. (2004). Cochlear nucleus. In *The Synaptic Organization of the Brain*, chapter 4. Oxford University Press New York, 5 edition.

Young, E. D. and Sachs, M. (2008). Auditory nerve inputs to cochlear nucleus neurons studied with cross-correlation. *Neuroscience*, **154**(1), 127–138.

Young, E. D. and Sachs, M. B. (1979). Representation of steady-state vowels in the temporal aspects of the discharge patterns of populations of auditory-nerve fibers. *The Journal of the Acoustical Society of America*, **66**(5), 1381–1403.

Zhang, C., Wang, M., Zhang, T., and Xie, R. (2024). Kv4 channels improve the temporal processing of auditory neurons in the cochlear nucleus. *The Journal of Physiology*.

Zhang, S. and Oertel, D. (1993). Tuberculoventral cells of the dorsal cochlear nucleus of mice: intracellular recordings in slices. *Journal of Neurophysiology*, **69**(5), 1409–1421.

Zilany, M. S. and Bruce, I. C. (2006). Modeling auditory-nerve responses for high sound pressure levels in the normal and impaired auditory periphery. *The Journal of the Acoustical Society of America*, **120**(3), 1446–1466.